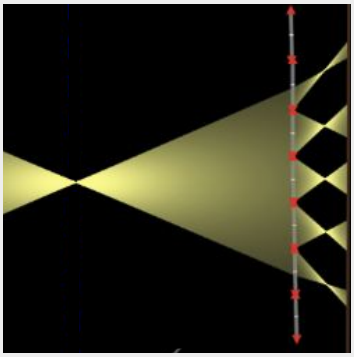

Dissertation

Fluorescence light field microscopy: wave optics modeling and 3D image reconstruction

Anca-Elena Ştefănoiu

Fakultät für Informatik
Technische Universität München

Technische Universität München
Fakultät für Informatik

Fluorescence light field microscopy: wave optics modeling and 3D image reconstruction

Anca-Elena Ştefănoiu

Vollständiger Abdruck der von der Fakultät für Informatik der Technischen Universität München zur Erlangung des akademischen Grades einer

Doktorin der Naturwissenschaften (Dr. rer. nat.)

genehmigten Dissertation.

Vorsitzender: Prof. Dr. Cristina Piazza
Prüfer der Dissertation:
1. Priv.-Doz. Dr. Tobias Lasser
2. Prof. Dr. Manuel Martínez-Corral

Die Dissertation wurde am 02.11.2021 bei der Technischen Universität München eingereicht und durch die Fakultät für Informatik am 28.02.2022 angenommen.

Abstract

Many years of active research and development have advanced fluorescence microscopy to new standards of contrast and resolution in biological imaging. While innovative super-resolution techniques enable the possibility of visualizing single molecules in cells, understanding complex biological processes usually requires multi-scale imaging. Many highly dynamic processes, such as brain activity in live animals, are not only very fast, but three dimensional in nature. In order to record such processes, high speed 3D microscopy techniques are needed.

Light field microscopy enables scanless 3D imaging of fluorescent specimens by strategically incorporating an array of micro-lenses into the optical path of a conventional wide-field microscope. Thus, similarly to a multi-stereo imaging device, the microscope captures both lateral and angular light field information in a single shot. This arrangement allows for subsequent volumetric reconstruction of the original 3D distribution of fluorescent emitters in the sample.

While its ability to capture the 3D scene at camera frame rate makes LFM particularly attractive for biological applications involving high dynamics, there are several challenges to the modality. As the system simultaneously records both lateral and axial information using a limited bank of sensor elements, the measurements are multiplexed, and thus the microscope captures axial information at the expense of lateral resolution.

In this thesis we develop 3D reconstruction schemes for computationally recovering high resolution images from light field measurements. We address two different microscope designs: the conventional light field microscope (LFM) and the Fourier light field microscope (FLFM). The conventional LFM employs a micro-lens array at the image plane of a standard wide-field microscope counterpart. In the case of the FLFM, the micro-lens array is placed at the Fourier plane. While the difference between these microscopes is minor in appearance, they are fundamentally different both in terms of complexity of the imaging model and in terms of recoverable resolution. The LFM configuration suffers from non-uniform resolution across the axial dimension, and exhibits very low resolution around the native object plane. This limitation is bound to the physical properties of the device and cannot be overcome computationally. The FLFM design was proposed more recently to address some of the disadvantages of conventional LFM.

In order to understand the sampling requirements of these devices, we analyze the image formation models and derive their wave-based point spread functions. We then propose custom 3D reconstruction algorithms that exploit the aliasing in the measurements to recover computationally super-resolved images and evaluate the methods using several biological samples.

Zusammenfassung

Über Jahre hinausgehende aktive Forschung und wissenschaftlicher Fortschritt haben die Fluoreszenzmikroskopie zu neuen Standards für Bildkontrast und Auflösung in der biologischen Bildgebung geführt. Während innovative Superauflösungstechniken die Möglichkeit bieten, einzelne Moleküle in Zellen zu visualisieren, erfordert das Verständnis komplexer biologischer Prozesse in der Regel mehrskalige Bildgebung. Viele hochdynamische Prozesse, wie die Gehirnaktivität von lebenden Tieren, sind nicht nur sehr schnell, sondern auch dreidimensional. Um solche Prozesse aufzuzeichnen, werden 3D-Mikroskopietechniken mit hoher Bildfrequenz benötigt.

Die Lichtfeld Mikroskopie (LFM) ermöglicht die scanless 3D-Bildgebung von fluoreszierenden Proben durch die strategische Einbindung eines Arrays von Mikrolinsen in der optischen Achse eines standard Weitfeldmikroskops. Somit erfasst das Mikroskop ähnlich einem Multi-Stereo-Bildgebungsgerät sowohl seitliche als auch Winkelinformation in einer einzigen Aufnahme. Diese Anordnung ermöglicht im Anschluss die volumetrische Rekonstruktion der ursprünglichen 3D-Verteilung der Fluoreszenzemitter in der Probe.

Was LFM besonders attraktiv für biologische Anwendungen mit hoher Dynamik macht, ist dessen Fähigkeit Aufnahmen von der 3D Szene in Echtzeit zu erfassen. Leider gibt es mehrere Herausforderungen an dieser Prozedur. Da die Anzahl an Sensorelementen, die für eine gleichzeitige Aufnahme von lateralen und axialen Informationen eingesetzt werden, begrenzt ist, müssen Messungen multiplexiert werden, was zu einem Kompromiss zwischen axialer und lateraler Auflösung führt.

In dieser Arbeit entwickeln wir 3D-Rekonstruktionsalgorithmen, die die rechnerische Wiederherstellung superauflösender Bilder aus Lichtfeldaufnahmen ermöglichen. Dafür untersuchen wir zwei verschiedene Implementierungen von Lichtfeld-Mikroskopen: das standard Lichtfeld-Mikroskop (LFM) und das Fourier-Lichtfeld-Mikroskop (FLFM). Ein standard LFM entsteht indem man ein Mikrolinsenarray in der Bildebene eines normalen Weitfeldmikroskop legt. Beim FLFM wird das Mikrolinsenarray in die Fourier-Ebene platziert. Obwohl die zwei Mikroskopen ähnlich sind, gibt es grundsätzliche Unterschiede die sich sowohl auf die Komplexität des Bildentstehungsmodells als auch auf die erreichbare Auflösung beziehen. Die LFM-Konfiguration leidet unter einer ungleichmäßigen Auflösung über die axiale Dimension und zeigt eine sehr niedrige Auflösung um die native Objektebene. Diese Einschränkung wird von der physikalischen Eigenschaften des Linsensystems bestimmt und kann rechnerisch nicht überwunden werden. Das FLFM-Design wurde in den letzten Jahren entworfen, um einige Nachteile des standard LFMs aufzeheben.

Um die Sampling-Anforderungen dieser Geräte zu verstehen, analysieren wir die Bilderzeugungsmodelle und leiten ihre wellenbasierten Punktbildfunktionen ab. Wir entwickeln dafür neue 3D-Rekonstruktionsalgorithmen, die das Alias-Effekt in den Messungen zu Gunsten der Erzeugung von superauflösenden Bilder nutzen und wir führen die Evaluation der Methoden auf mehreren biologischen Proben aus.

Acknowledgements

The presented thesis concludes my time at the Technical University Munich and I would like to take this chance to express my gratitude to the people who have enabled me to complete this journey. These past several years have had it all.

To begin with, I want to wholeheartedly thank my advisor, Tobias Lasser from whom I have learned a lot during this time. Thank you Tobias, for giving me this opportunity and for your guidance along the way. I could not have hoped for better mentorship. Retrospectively, I am deeply thankful to Max Baust for encouraging me to jump on this ride and for drawing my attention to Tobias' group. I am grateful for having been part of the CIIP group and I want to thank my colleagues Josue Page, Theodor Cheslerean, Erdal Pekel and Jonas Jelten for all the moments we have shared and for making CIIP such a great team. I want to especially thank Josue, my research partner, for all our discussions and discoveries. It was a great pleasure to work with you and I am looking forward to learn about your new findings.

The kind of research presented here would not have been possible without our collaborators. I would like to thank Gil Westmeyer for providing us with the biological context which motivates this work. A special thank you goes to Panagiotis Symvoulidis for his essential input to this thesis and for all the help during and after our collaboration. I also want to thank Gabrielle Scrofani and Manuel Martínez-Corral for a great collaboration. I am very grateful for having had the chance to work with you.

Furthermore, I would like to thank all talented students I had the pleasure to supervise. Special thanks go to Felix Wechsler, Erik Riedel, Viktoria Markova, Katharina Sommer and Ana Lacatusu. I want to also thank Nassir Navab and all my collegues at the CAMP chair for making my time there enjoyable. Many thanks go to Salvatore Virga, Mira Slavcheva, Federico Tombari, Walter Simsons, Rüdiger Göbl, Ari Tran and of course, Martina Hilla.

I would also like to take this chance to thank my friends and my family for being there and for much more. Special thanks go to my friends in Munich who have made this place my home. Thank you Bule, Phalgun, Theo, Andrei, Dinu, Dani, Chris, Eteri and little Aren. A very special thank you goes to my parents and my brother. There are no words to describe the extent of my gratitude to you for all your support throughout my life. Thank you for everything! Nevertheless, for the love he brings among our family, a big shout-out goes to Toffee. Finally, I want to thank my husband, Matei, whom I met at the very start of my PhD journey. Thank you for all the support and love throughout these years. I love sharing ideas with you and it is the greatest blessing having you in my life. Thank you so much!

Contents

List of Figures

List of Tables

Part I

Introduction

Chapter 1

Introduction

1.1 Pioneers of microscopy

It was the seventeenth century when lenses became scientific instruments for the study of living organisms. Around 1590, Zaccharias Janssen who was only five to ten years old at that moment, invented the compound microscope while working in his father's eyeglass workshop in the Netherlands [1]. In a compound microscope the overall magnification is obtained using two main optical elements: the objective lens and the eye-piece. At that time, Janssen's invention was capable of achieving up to 9× magnification. The term "microscope" was first used in 1625 by the botanist Giovanni Faber to describe Galileo's "occhiolino" built in 1609 [2]. The word "microscope" has its root in the Greek "mikros" (small) and "skopos" (observer). Galileo's design (also a compound microscope) provided up to 30× magnification.

Until the late 1600s there are, however, no documented observations from these instruments. The first major development was marked in 1655 when the English natural philosopher, Robert Hooke published "*Micrographia*" [3] promoting the microscope as a promising scientific instrument. "*Micrographia*" is the first illustrated microscopy book and it contains many detailed observations including plants, seeds, a flea and the eye of a fly [4, 5]. Hooke named the pores inside a cork sample as "cells", and thus coining the biological term in use today [6]. Hooke's microscope was a compound one, very similar to the modern ones. Its design featured a light source (oil lamp) to illuminate the sample, a stage and height adjuster. This setup enabled him to achieved up to 50× magnification [4].

The most prominent figure related to the development of the microscope is probably Antonie van Leeuwenhoek (1632-1723) who is known as the "Father of Microbiology". He has built over five hundred high-quality lenses and microscopes capable of magnifying up to 275×. Antonie van Leeuwenhoek's instruments were not compound microscopes. Unlike Hooke, he used single lenses which reduced the problems of optical aberrations and produced superior quality images compared to the instruments of that time. Enclosing a single spherical lens and a sample holding pin, without an in-built light source, his microscopes were lightweight. This setup allowed for imaging the samples as they were collected in the field. The imaging

process consisted of sketching and documenting observations. His ability to grind and polish extremely high-quality lenses capable of the greatest magnification of his times, together with an extraordinary dedication to research, promote Van Leeuwenhoek to the rank of pioneer in many areas of microbiology [6]. In his work, he studied the microscopic structure of seeds, fish scales, nerves, bones, muscle fibers, algae and discovered microorganisms such as bacteria and protozoa and other very small animals which he referred to as “animacule”. He communicated his findings through letters addressed to the Royal Society [7].

1.2 Fluorescence microscopy

When imaging biological samples under a bright-field microscope, the contrast is obtained from the scattering and absorption of incident light. As these samples are generally transparent, due to their refractive index being close to that of water, they do not interact much with the incident light. As a result, the captured images exhibit low contrast. In order to address this challenge in biological imaging, various modalities have been developed, including phase imaging (as opposed to amplitude), sample staining and fluorescence imaging.

First described by Fritz Zernike in the 1930s [8], phase contrast microscopy is a technique for producing enhanced contrast images of transparent samples. When light waves travel through a medium, their amplitude and phase change. While the amplitude variations (brightness) are the ones being sensed by the human eye or digital cameras, the shift in phase often carry important information. The light scattered by a specimen is usually phase-shifted by 90 degrees relative to the illuminating light. Based on this observation, phase changes can be made visible in phase contrast imaging as the transmitted and scattered light can be manipulated independently. Phase contrast microscopy is an important advancement in biology and, as a consequence, Zernike was awarded the Nobel prize in 1953 [9].

Another technique to improve the contrast in biological imaging is staining. Using high contrast substances, such as dyes, allows for highlighting micro-structures in biological specimens. Differential contrast is obtained when certain parts of the sample are stained, for example, in order to differentiate between the cytoplasm and the nucleus of the cell [10]. Staining can also enable scientists to visualize metabolic processes. Staining breakthroughs that are worthy of mention include the work of Camillo Golgi who used silver staining to visualize nervous tissue [11] and Gram’s staining method for identifying bacterial organisms [12] which is the most commonly used staining method as it differentiates a wide range of pathogens. However, the development of fluorescent staining has revolutionized the contrast enhancement in microscopic imaging of biological specimens. Fluorescence imaging is probably the most far-reaching development since the invention of the light microscope [6].

In 1852, British scientist George Gabriel Stokes published a paper describing the ability of fluorite to transform UV light into blue visible light. He coined the word “fluorescence” for referring to this phenomenon of wavelength change (refrangibility of light) [13]. As a more general definition, florescence is the emission of light by a material that absorbed light (or other electromagnetic radiation). The emitted light was a different (usually higher) wavelength than the one of the excitation radiation.

While fluorescence occurs naturally in some minerals and organisms (biofluorescence), fluo-

rophores can also be artificially synthesized. With the first fluorescent stain (fluorescein) being developed in 1871 by the chemist Adolf von Bayer [14], fluorescent staining enables a massive enhancement in detection contrast. In 2008, scientists Martin Chalfie, Roger Tsien and Osamu Shimomura were awarded the Nobel prize for the development of of the green fluorescent protein (GFP). While the GFP was first isolated from the jellyfish Aequorea Victoria in 1962 by Shimomura et al. [15], in 1994 Chalfie et al. [16] showed that it could be expressed and fluoresce outside of the jellyfish. In cell biology, the GFP is used as a marker for gene expression. It can be introduced in animals through genetic manipulation techniques and maintained in their genome (and in the genome of their offspring) allowing for the continuous study of cells it is expressed in.

After many years of research and development of various techniques, fluorescence microscopy is arguably the most versatile optical imaging modality and an essential tool for modern biologists. With the development of dichromatic beam splitters [17, 18], the epi-fluorescence microscope (reflected light fluorescence microscope) has become the standard choice. The design allows for both excitation and emission optics to be on the same side of the specimen [6]. Using a dichroic mirror, the objective focuses the illumination light on the sample and also collects the light being emitted.

Capable of optical scanning, confocal fluorescence microscopy [19], uses a pinhole to ensure that a small extent of the sample is illuminated, while another pinhole, at the detector, only collects in-focus light. The design enhances the contrast considerably by reducing the out-of-focus (background) light in the image, especially with laser-scanning illumination [20] which is one of the most important advancements in fluorescence imaging [21].

Important advances have also been achieved on the illumination side. Two-photon excitation fluorescence (2PEF) microscopy, developed from the concept of two-photon absorption, first described in 1931 by Maria Gopport-Mayer [22], allows for imaging up to 1 mm deep tissue. Two photons with longer wavelength than that of the the emitted light are required to trigger the emission of one photon whose energy is the accumulated energy of the two excitation photons. Due to its deep tissue penetration and low background signal, 2PEF has become a powerful technique, in many cases, superior to confocal microscopy [23].

Light sheet fluorescence microscopy (LSFM) is another efficient method for high contrast fluorescence imaging [24, 25]. As opposed to epi-fluorescence microscopy, LSFM illuminates only a thin slice (a hundred nanometers to several millimeters) of the sample. A laser light-sheet is used to illuminate perpendicularly to the imaging direction. It allows for 3D optical sectioning and 3D reconstruction through slice-by-slice scanning. While the quality of the recorded images is comparable to the ones obtained in confocal microscopy, LSFM is orders of magnitude faster as it allows for an entire plane to be imaged at once.

1.3 Super-resolution and 3D microscopy

According to Abbe's theory [26], the highest achievable resolution that can be obtained with an optical microscope, is imposed by the wave nature of light. The so-called "diffraction limit" governs the resolving power of optical instruments. Thus, object points separated by a distance less than about half the wavelength of the incident light, cannot be resolved. Although

technological advancements have led to spectacular image quality in microscopy, for over one hundred years, Abbe's diffraction barrier has been the ultimate limit in optical resolution. More recently, innovative, non-conventional techniques have demonstrated spatial resolution beyond what was believed unbreakable.

Stimulated emission depletion microscopy (STED) is one of the super-resolution microscopy techniques, able to overcome the diffraction limit of light microscopy. STED works by selectively deactivating fluorophores in certain regions of the specimen. The depletion is usually achieved over a doughnut-shaped de-excitation region [27], allowing for the emission to occur from only a narrow central focal spot inside the deactivation torus. When the emission region is smaller in extent than Abbe's diffraction limit, a super-resolution image is obtained. Stephan Hell, who was awarded the Nobel Prize in Chemistry in 2014 for STED, has developed it together with Jan Wichmann in 1994 [28] and experimentally demonstrated it together with Thomas Klar in 1999 [29].

Photo-activated localization microscopy (PALM) is another innovative super-resolution microscopy technique, invented by Eric Betzig and Herald Hess [30]. PALM relies on photo-activatable fluorophores [31] to distinguish spatial locations of densely packed molecules [32]. In PALM, ultra-violet laser light is used to selectively activate subsets of fluorophores in a specimen at a given time in order to localize each of them individually. When the emission of neighboring molecules is triggered at different times, the photons coming from each such molecules can be recorded separately. By randomly triggering small numbers of fluorophores until all of them have emitted, their position can be accurately mapped in a super-resolution image. In 2014 Eric Betzig was awarded the Nobel Prize in Chemistry for his contribution to super-resolution fluorescence microscopy.

Stochastic optical reconstruction microscopy (STORM), proposed by Rust *et al*. [33] in 2006 is another single molecule localization microscopy technique (SMLM). STORM relies on photo-switchable dye pairs. Photoswitchable molecules can alternate between fluorescence and dark state under different laser light activation, such that only a fraction of the fluorophores emit at a time. Similarly to PALM, by repeatedly recording these signals, a super-resolution image is generated.

Structured illumination microscopy (SIM) is another important super-resolution technique. In SIM the sample is illuminated with a known striped light pattern (using a periodic grating). By shifting the illumination pattern in a controlled way, a collection of images is acquired. These images exhibit Moiré fringes [34]. Combining the information in interference signals, a super-resolved image can be obtained via deconvolution. Using this technique a twofold improvement over the optical resolution limit can be achieved [35].

These high resolution techniques, in combination with innovative illumination schemes, are successfully capable of achieving high quality volumetric imaging [36, 37]. Confocal laser scanning microscopy (CLSM) is probably the most commonly used technique for 3D microscopic imaging [20, 38]. CLSM uses a point laser illumination and a pinhole at the detector to block out-of-focus light. A 2D image is obtained via scanning over the specimen in a raster pattern. A 3D image can be obtained by stacking together 2D images of the cross sections.

Other 3D microscopy techniques encode the depth information by asymmetrically distorting the shape of the point spread function (PSF) of the system through PSF engineering methods

[39, 40]. Controlled distortions are usually achieved through inserting a phase mask in the optical path. These distortions are depth dependent due to the phase mask acting on the phase of the incoming wavefront [41]. Double-helix PSF (DH-PSF) [42] is one such 3D phase mask based microscopy technique. The axial profile of the DH-PSF resembles an intertwined helix, rather than the hourglass shape of the conventional PSF. The effective system response at the sensor plane appears as two distinct spots and the orientation of these pairs of spots encodes the axial position of a fluorescent molecule.

A thorough review of technological advancements and forecasts in fluorescent microscopy is offered by Wollman *et al*. [6].

1.4 Light field microscopy

Dynamic biological processes, such as calcium signaling during brain activity or the mechanics of heart beats, occur in three dimensions and at high speed in live animals. One major challenge in optical imaging is to record such processes with sufficient temporal and spatial (lateral and axial) resolution [43]. While scanning microscopy approaches are highly optimized for image quality, they lack on the temporal aspect.

To address this challenge, light field microscopy (LFM) enables scanless 3D imaging of fluorescent specimens by strategically incorporating an array of micro-lenses (MLA) into the optical path of a conventional wide-field microscope. Thus, both spatial and directional light field information (4D ligh field) is captured in a single shot, allowing for subsequent volumetric reconstruction of the original 3D distribution of fluorescent emitters in the imaged sample. Due to its high speed 3D imaging capability, LFM has proven very attractive around applications involving recording highly dynamic biological processes due to its ability to capture the 3D scene at camera frame rate, without scanning. The potential of the modality has been demonstrated in various biomedical application where speed represents a critical factor, including recording neuro-dynamics in vertebrate model organisms [44–49] or live cell imaging [50].

Lenslet-based (plenoptic) imaging [51] has emerged from the principles of integral photography proposed by G. Lippmann in 1908 [52]. Both light field photography [53–57] and light field microscopy [58–61] have attracted a lot of interest and have become important research topics in computational imaging. Plenoptic cameras enable various post-acquisition processing possibilities like image refocusing [53, 62, 63], depth estimation [64–66] or 3D object reconstruction via deconvolution and computational super-resolution methods [67–69].

While the scan-less 3D imaging capability is very attractive, the technique suffers from a number of disadvantages. As the LFM captures both lateral and axial information using a limited bank of sensor elements, the information is multiplexed, and therefore the microscope captures axial information at the expense of lateral resolution. This drawback represents the well-known resolution trade-off in light field imaging [54–58, 62, 67, 70].

A considerable research effort aims at improving the image quality and increasing the resolution of LFM systems. Innovative hardware variations and extensions are actively being proposed. [50, 68, 71] discuss different strategies for introducing the MLA in the optical path of the LFM, with respect to the camera sensor. Other proposals include wave-front coding

techniques for extended depth of field in LFM [72, 98], simultaneous light field and wide field acquisition systems [73] or dual-LFM devices which combine complementary information from two plenoptic systems [45]. On the other hand, inspired by the large amount of work on computational super-resolution in the computer vision field [74, 75], algorithms for super-resolving the light field are proposed, involving multi-view reconstruction schemes [76, 77], or explicit image formation models for plenoptic devices employing either ray-based [57, 64, 78] or wave-based optics [67, 68, 72, 79].

1.5 Structure of this thesis

In this thesis we discuss popular LFM setup designs and accompanying algorithmic approaches for 3D object reconstruction from raw light field measurements.

Part II (Chapter 2) presents fundamental notions of diffraction theory for deriving the point spread function of an optical system, together with mathematics of inverse problems with a focus on statistical inversion in the context of image deconvolution. This theoretical background provides the building blocks for the algorithms developed in the main body of the thesis.

In Part III specialized reconstruction algorithms are derived for two light field microscope configurations: conventional LFM in Chapter 3 and Fourier LFM in Chapter 4. These chapters are similar in structure. We analyze the image formation and derive the setup specific light field point spread function used for 3D deconvolution. The deconvolution algorithms incorporate the intricacies of the microscope designs to recover computationally super-resolved images. The proposed methods are evaluated using measurements acquired with our experimental setups.

Part IV (Chapter 5) presents *oLaF*, a flexible Matlab framework for 3D reconstruction of light field microscopy data. *oLaF* suports the various LFM configurations discussed in the previous part of the thesis. Besides describing the available functionality, this chapter also offers a tutorial for using the framework.

Part V (Chapter 6) is dedicated to *NeuBtracker*, the project that marks my debut in computational imaging research. *NeuBtracker* is an open-source modular platform for neuro-behavioral imaging and manipulation that enables simultaneous and non-invasive monitoring of brain activity and behavioral parameters in unrestrained, freely swimming zebrafish larvae.

Finally, Chapter 7 contains a short conclusion.

Part II

Background

CHAPTER 2

Background

2.1 Diffraction theory

The diffraction property of light waves describes the light propagation behaviour when encountering an obstacle. This behaviour deviates from the geometric optics predictions and, in order to characterize an optical system's performance (resolving power), it is necessary to consider and model diffraction. Sommerfeld defined diffraction as "any deviation of light rays from rectilinear paths which cannot be interpreted as reflection or refraction" [80].

This Chapter selectively introduces the theory for deriving the diffraction models used in Chapters 3 and 4. For a rigorous and exhaustive discussion on diffraction theory, the interested reader is referred to [81, 82].

2.1.1 Wave optics

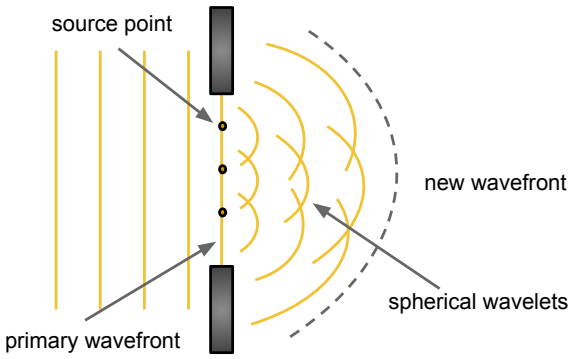

Figure 2.1: The Huygens-Fresnel principle: the superposition of spherical wavelets originating from a wavefront at an earlier time defines the wavefront at a later time.

The **Huygens-Fresnel principle** [83, 84] states that every point of a wavefront of light is the origin of a secondary wave having the same speed and frequency. All these wavelets give rise to the wavefront at a later point in time. The amplitude distribution on the new wavefront is given by the superposition of all the wavelets, as depicted in Fig. 2.1.

According to this principle, when a plane wave illuminates an opaque screen containing a small aperture, the diffraction pattern the light field undergoes depends on the distance between the aperture and the plane of observation. A spherical wavelet originating at a point P_1 within a small aperture $\sum$ contributes to the light field at a point P_2 on the observation the following:

$$U(P_1)\frac{e^{-ikr}}{r}, \tag{2.1}$$

where $U(P1)$ is the amplitude of the wavelet at P_1 and r is the distance from point P_1 to point P_2. The factor $\frac{e^{-ikr}}{r}$ is a spherical wave originating at P_1. Here k is the wave number defined as $k = \frac{2\pi n}{\lambda}$, where n is the refraction index of the medium and λ is the wavelength. Then, the mathematical formulation of the Huygens-Fresnel principle expresses the total amplitude at point P_2 as the integration over the aperture area:

$$U(P_2) = \iint_{\sum} U(P_1)\frac{e^{-ikr}}{r}ds. \tag{2.2}$$

Although the Huygens-Fresnel principle provides a good qualitative prediction for the diffraction patterns by an aperture, more accurate formulas are derived from Maxwell's wave equations. Depending on the employed boundary conditions, different solutions exist (Rayleigh-Sommerfeld I and II, Kirchoff-Fresnel diffraction integrals). These solutions are equivalent when the diffracting aperture and the distance to the observation plane are both far larger than the light wavelength, which is the case for optical systems with a low numerical aperture (NA). A complete treatise is offered in [81].

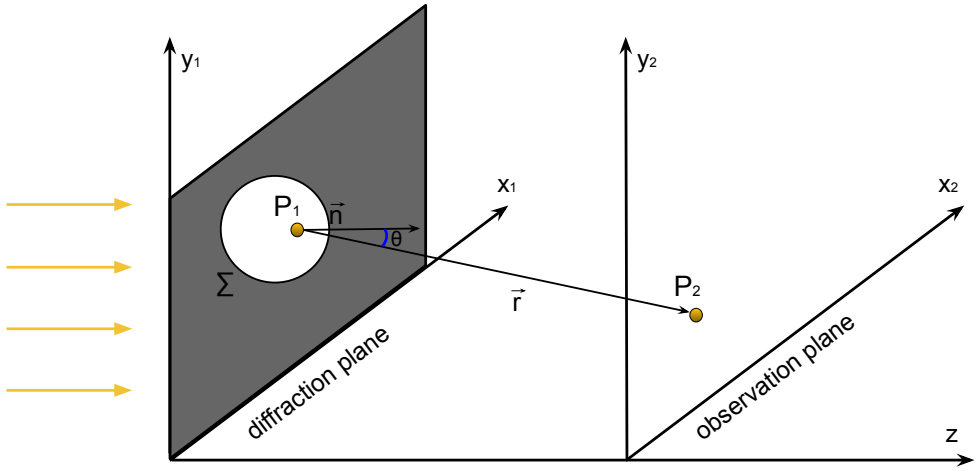

Figure 2.2: Diffraction by an aperture.

For simplicity, the **first Rayleigh-Sommerfeld integral** is commonly used as it closely resembles the Huygens-Fresnel formula in Eq. 2.2:

$$U(P_2) = -\frac{i}{\lambda}\iint_{\sum} U(P_1)\frac{e^{-ikr}}{r}cos(\theta)ds, \tag{2.3}$$

where θ is the angle between the normal vector of the diffraction aperture ($\vec{n}$) and the direction of observation ($\vec{r}$) as depicted in Fig. 2.2.

In common diffraction scenarios, we are mostly interested in observing the field close to the optical axis of a given imaging system. The so called "paraxial approximation" or **Fresnel approximation** can be assumed in this case. In Fig. 2.2, the plane (x_1, y_1) represents the diffraction plane and (x_2, y_2) the observation plane. z is the distance between these planes. Then r, the distance between a point $P_1(x_1, x_2)$ within the diffraction aperture and an observation point $P_2(x_2, y_2)$, can be expressed as:

$$r = \sqrt{z^2 + (x_2 - x_1)^2 + (y_2 - y_1)^2} = z\sqrt{1 + \frac{(x_2 - x_1)^2 + (y_2 - y_1)^2}{z^2}}. \tag{2.4}$$

When the observation point is relatively close to the optical axis, one can assume that $z^2 \gg (x_2 - x_1)^2 + (y_2 - y_1)^2$. Using the fact that $\sqrt{a+b} \approx a(1 + \frac{b}{2a})$ if $a \gg b$, Eq. 2.4 becomes:

$$r = \sqrt{z^2 + (x_2 - x_1)^2 + (y_2 - y_1)^2} = z(1 + \frac{(x_2 - x_1)^2 + (y_2 - y_1)^2}{2z^2}). \tag{2.5}$$

Conveniently, as a direct implication of the paraxial approximation, $cos(\theta)$ can be reduced to unity and r in the denominator of Eq. 2.3 can be safely replaced by z. Under Fresnel approximation, Eq. 2.3 becomes:

$$U(x_2, y_2) = \frac{ie^{-ikz}}{\lambda z}\iint_{-\infty}^{\infty} P(x_1, y_1)U(x_1, x_2)e^{-\frac{ik}{2z}[(x_2 - x_1)^2 + (y_2 - y_1)^2]}dx_1 dy_1, \tag{2.6}$$

where $P(x_1, y_1)$ is the pupil function for a circular aperture.

In order to compute accurate results under this approximation, the observation point needs to be relatively far away from the diffraction plane. The Fresnel number, $F = \frac{a^2}{\lambda z}$ establishes a guide for defining the scenarios when the approximation holds; a being the radius of the diffraction aperture. When z is larger than the aperture size, the propagation regime verifies $F \approx 1$.

2.1.2 Deriving the point spread function

The point spread function (PSF) of an optical system describes the system's response to a point source. When treating an object field as the weighted sum of impulse functions, the image of

the object in a microscope can be computed as the weighted (by the field amplitude) sum over the images of these impulse functions. When modeling the object as a set of discrete source points with varying intensities, the image is computed as the sum of the PSF for each point.

For linear systems, such as fluorescence microscopes, this process is conveniently expressed via a convolution operation. Fig. 2.3 illustrates the imaging process with an artificially computed image of cotton fibers using the simulated PSF of a wide-field microscope. The degree of blurring of an object point characterizes the performance of the imaging system. In certain conditions, if the PSF is known, it is possible to restore the original object via deconvolution as discussed in Sec. 2.2. The PSF is determined by the properties of the optical system and it can be calculated by modeling the imaging conditions.

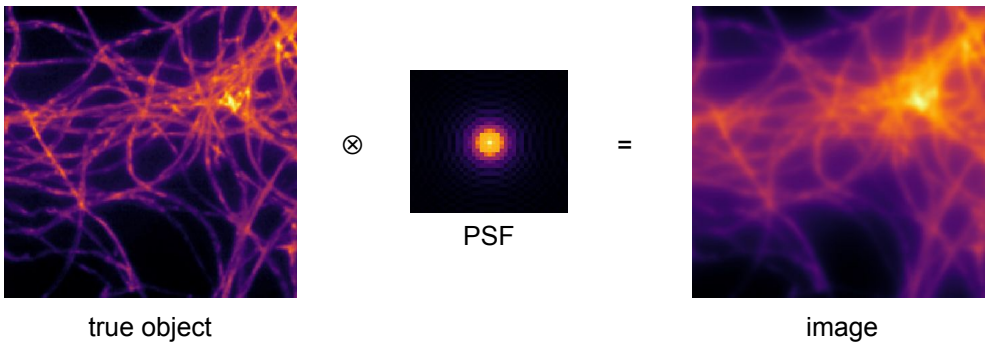

Figure 2.3: Simulated microscope image of cotton fibers via convolution with a theoretical PSF.

2.1.2.1 Lens transmittance

When passing through an optical lens, a light wave undergoes a phase and an amplitude change. The amplitude change is due to the reflected intensity on the surface of the lens. The transmittance of a lens is then a complex function of the form:

$$t(x,y) = P(x,y)e^{-i\phi(x,y)}, \tag{2.7}$$

where the pupil function, $P(x,y)$ affects the amplitude of the incident field and $e^{-i\phi(x,y)}$ represents the phase change due to the change in the direction of propagation.

Fig. 2.4 shows a lens composed of two spherical surfaces with radii of curvature R_1 and R_2. If the thickness of the lens (D) is small such that the displacement of the coordinates in the front and back of the lens due to refraction is neglectable, the change of phase between U_1 and U_2 is derived as [81]:

$$\phi(x,y) = -\frac{k(x^2+y^2)}{2f}, \tag{2.8}$$

where $k = \frac{2\pi}{\lambda}$ is the wave number of the incident light and f is the focal length of the lens defined as:

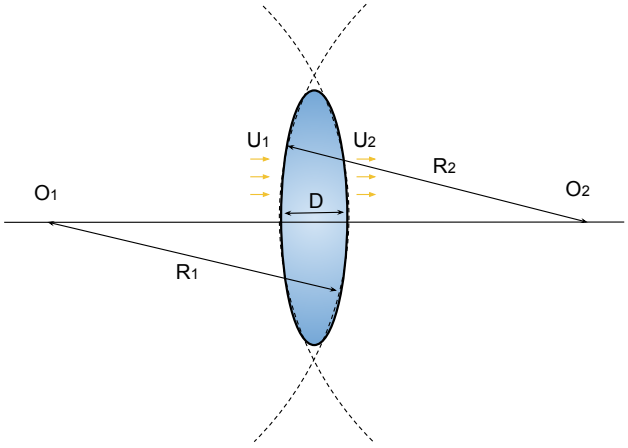

Figure 2.4: A thin double-convex lens with radii of curvature R_1 and R_2. D is the thickness of the lens on the optical axis. The light fields right before and after the lens are related through the transmittance function such that $U_2(x,y) = U_1(x,y)t(x,y)$.

$$\frac{1}{f} = (n-1)(\frac{1}{R_1} - \frac{1}{R_2}), \tag{2.9}$$

here n is the refractive index of the lens.

The complex transmittance of a thin lens is then given as:

$$t(x,y) = P(x,y)e^{\frac{ik(x^2+y^2)}{2f}}. \tag{2.10}$$

A plane wave incident on a double-convex lens converges to the "focus point" at a distance f behind the lens.

2.1.2.2 Diffraction by a lens

Having discussed the light field propagation in the paraxial regime and the transmittance of a thin lens, we can now characterize the field distribution around the focal region of a lens.

If a plane wave incident on the lens generates the field $U_-(x_1,x_1)$ just in front of the lens, as depicted in Fig. 2.5, then due to the complex lens transmittance given by Eq. 2.10, immediately behind the lens, the field $U_+(x_2,y_2)$ is derived as:

$$U_+(x_2,y_2) = U_-(x_2,y_2)P(x_2,y_2)e^{\frac{ik(x_2^2+y_2^2)}{2f}}. \tag{2.11}$$

Propagating this field further to the back focal plane using Fresnel's diffraction formula introduced in Eq. 2.6, the field U_f is given as:

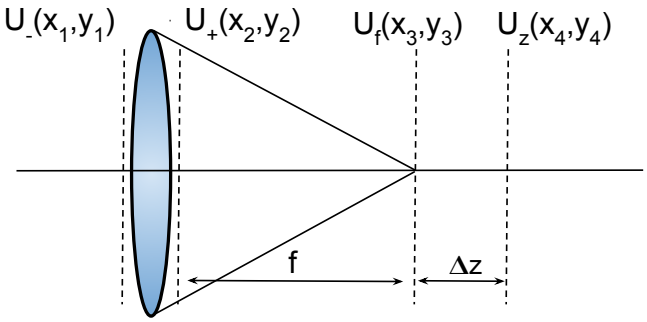

Figure 2.5: Diffraction by a lens.

$$U_f(x_3, y_3) = \frac{iU_-(x_2, y_2)}{\lambda f} e^{-ikf} e^{-\frac{ik(x_3^2+y_3^2)}{2f}} \iint_{-\infty}^{\infty} P(x_2, y_2) e^{\frac{ik(x_3x_2+y_3y_2)}{2f}} dx_2 dy_2. \tag{2.12}$$

When the observation plane is placed at a Δz displacement from the focal plane, or at a distance z behind the lens as suggested by Fig. 2.5, under Fresnel's approximation, the field becomes:

$$U_z(x_4, y_4) = \frac{iU_-(x_2, y_2)}{\lambda z} e^{-ikz} \iint_{-\infty}^{\infty} P(x_2, y_2) e^{\frac{ik(x_2^2+y_2^2)}{2f}} e^{-\frac{ik}{2z}[(x_4-x_2)^2+(y_4-x_2)^2]} dx_2 dy_2. \tag{2.13}$$

Finally, as common symmetrical imaging systems employ circular lenses, the diffraction pattern by a circular thin lens in a defocused plane (when the incident field has unit amplitude), as derived in [81], becomes:

$$U_z(r_4) = \frac{i}{\lambda z} e^{-ikz} e^{-\frac{i\pi r_4^2}{\lambda z}} \int_{-\infty}^{\infty} P(r_2, z) J_0\left(\frac{2\pi r_2 r_4}{\lambda z}\right) 2\pi r_2 dr_2. \tag{2.14}$$

Here $P(r_2, z) = P(r_2) e^{\frac{ikr_2^2}{2}\left(\frac{1}{f}-\frac{1}{z}\right)}$ represents the so-called defocused pupil function of the lens. J_0 is the Bassel function of the first kind of order zero. r_2 and r_4 are the radial coordinates: $r_2 = \sqrt{x_2^2 + y_2^2}$ and $r_4 = \sqrt{x_4^2 + y_4^2}$.

The derivations above assume the field incident on the lens has an uniform amplitude ($U_1(x_1, y_1) = 1$). When imaging an actual object placed in front of the lens, as illustrated in Fig. 2.6, the amplitude transmittance of the object needs to be taken into consideration, $U_1(x_1, y_1) = o(x_1, y_1)$. Employing the Fresnel's diffraction formula introduced in Eq. 2.6 together with the lens transmittance in Eq. 2.10, the field at the imaging plane is given as:

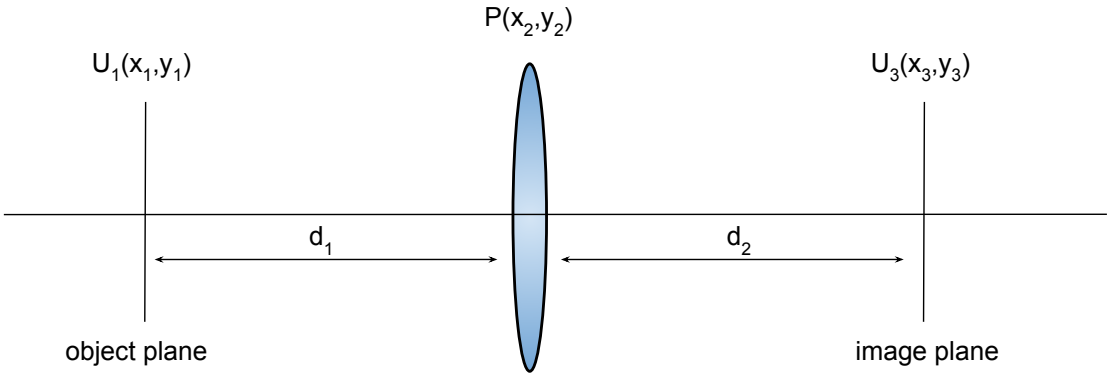

Figure 2.6: Imaging through a single lens.

$$
\begin{aligned}
U_3(x_3,y_3) = \frac{e^{-ik(d_1+d_2)}}{d_1 d_2 \lambda^2} e^{-\frac{ik}{2d_2}(x_3^2+y_3^2)} \iiiint_{-\infty}^{\infty} P(x_2,y_2) o(x_1,y_1) e^{-\frac{ik}{2d_1}(x_1^2+y_1^2)} \\
e^{\frac{ik}{2}\left(\frac{1}{f}-\frac{1}{d_1}-\frac{1}{d_2}\right)(x_2^2+y_2^2)} \\
e^{ik\left[\frac{x_2}{d_1}\left(x_1+\frac{d_1}{d_2}x_3\right)+\frac{y_2}{d_1}\left(y_1+\frac{d_1}{d_2}y_3\right)\right]} dx_1 dy_1 dx_2 dy_2.
\end{aligned}
\tag{2.15}
$$

Eq. 2.15 describes the relationship between an object and its image through a single lens. $|U_3(x_3,y_3)|^2$ represents the intensity image as it would be captured by a camera placed at the observation plane (U_3).

2.1.2.3 Point spread function

When the object and the observation plane in Fig. 2.6 satisfy the geometric lens law $\frac{1}{d_1}+\frac{1}{d_2}=\frac{1}{f}$, equation Eq. 2.15 can be simplified as [81]:

$$
\begin{aligned}
U_3(x_3,y_3) = \frac{M e^{-ikd_1\left(1+\frac{1}{M}\right)}}{d_1^2 \lambda^2} e^{-\frac{ikM}{2d_1}(x_3^2+y_3^2)} \\
\iint_{-\infty}^{\infty} o(x_1,y_1) e^{-\frac{ik}{2d_1}(x_1^2+y_1^2)} h(x_1+Mx_3, y_1+My_3) dx_1 dy_1,
\end{aligned}
\tag{2.16}
$$

where $M=\frac{d_1}{d_2}$ is the demagnification factor and $h(x,y)$ is the Fourier transform of the pupil function:

$$
h(x,y) = \iint_{-\infty}^{\infty} P(x_2,y_2) e^{\frac{ik}{d_1}(x_2 x, y_2 y)} dx_2 dy_2. \tag{2.17}
$$

The function $h(x,y)$ is called the 2D point spread function (PSF) as it represents the image of a single point object. This is best understood when $o(x_1,x_2)$ is replaced by a delta function in

Eq. 2.16. In a good optical system, the PSF has to be close to the point object and $x_1 \approx -Mx_3$, $y_1 \approx -My_3$ [81]. Subsequently, Eq. 2.16 can be rewritten as:

$$U_3(x_3, y_3) = \frac{Me^{-ikd_1\left(1+\frac{1}{M}\right)}}{d_1^2\lambda^2} e^{-\frac{ikM}{2d_1}(x_3^2+y_3^2)(1+M)} \iint_{-\infty}^{\infty} o(x_1, y_1)h(x_1 + Mx_3, y_1 + My_3)dx_1dy_1. \tag{2.18}$$

As the 2D convolution operation in equation Eq. 2.18 shows, the image of an object is the superposition of the PSF shifted around positions (Mx_3, My_3) and weighted by the object transmittance, $o(x_1, x_2)$. The intensity image is then given by the modulus squared of Eq. 2.18.

It is worth mentioning here that in a "defocused" scenario, when the object and observation planes do not satisfy the lens law: $\frac{1}{d_1} + \frac{1}{d_2} \neq \frac{1}{f}$, the defocused PSF, $h_d(x, y)$ can be expressed as:

$$h_d(x, y) = \iint_{-\infty}^{\infty} P_d(x_2, y_2)e^{\frac{ik}{d_1}(x_2x, y_2y)}dx_2dy_2. \tag{2.19}$$

$P_d(x_2, y_2) = P(x_2, y_2)e^{\frac{ik}{d_0}(x_2^2+y_2^2)}$ is the effective pupil function which accounts for the defocus effect. d_0 is introduced here such that it satisfies $\frac{1}{d_0} = \frac{1}{d_1} + \frac{1}{d_2} - \frac{1}{f}$.

In this case, the intensity image of the object is given by the squared modulus of the convolution of the object transmittance function with the defocused PSF, $h_d(x, y)$.

Interestingly, when $d_1 = d_2 = f$, $U_3(x_3, y_3)$ becomes the 2D Fourier transform of the object transmittance:

$$U_3(x_3, y_3) = \frac{e^{-2ikf}}{i\lambda f} \iint_{-\infty}^{\infty} o(x_1, y_1)e^{\frac{ik}{f}(x_1x_3+y_1y_3)}dx_1dy_1. \tag{2.20}$$

Eq. 2.20 describes the Fourier property of a thin lens. When an object is placed at the front focal plane of the lens, the field at the back focal plane represents the 2D Fourier transform of the object function. This property holds when the lens is much larger in size than the imaged object.

2.1.2.4 4-f optical systems

The field at the back focal plane does not represent the image of the field at the front focal plane, due to the Fourier property. In order to obtain an image of an object placed in front of the lens (at the focal plane), a second lens is used as illustrated in Fig. 2.7. This secondary lens is usually referred to as "tube lens" in microscopy setups.

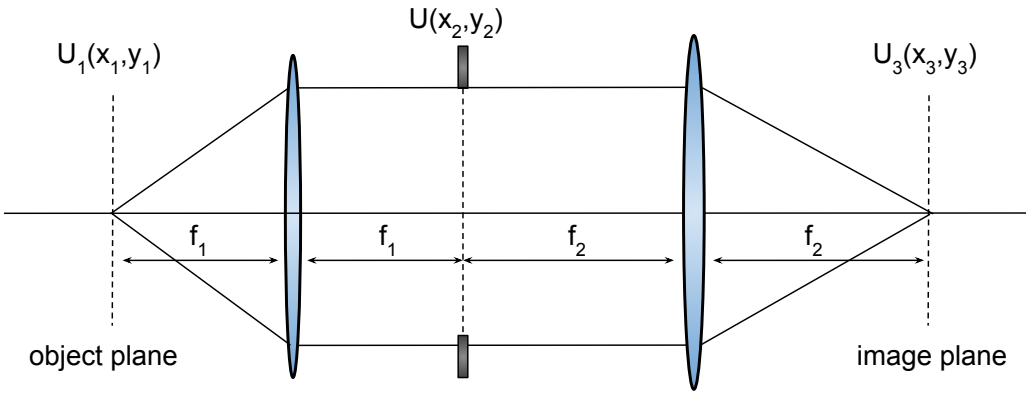

Figure 2.7: A 4-f imaging system.

According to Abbe imaging theory, when the size of the two lenses is sufficiently large in comparison with the size of the object, the field at the back focal plane of the first lens (objective lens in a microscope) is the Fourier transform ($\mathscr{F}$) of the object plane field. Analogously, the field at the back focal plane of the second lens is the Fourier transform of the field at the its front focal plane:

$$U_2(x_2, y_2) = \mathscr{F}\{U_1(x_1, y_1)\}, \tag{2.21}$$

$$U_3(x_3, y_3) = \mathscr{F}\{U_2(x_2, y_2)\} = U_1(-x_1, -y_1). \tag{2.22}$$

In practice, the focal lengths of the two lens are different and a magnification factor $M = \frac{f_2}{f_1}$ is introduced such that:

$$U_3(x_3, y_3) = U_1(-Mx_1, -My_1). \tag{2.23}$$

Finally the minus sign in equation Eq. 2.23 suggests the 4-f optical system creates an inverted and magnified image of the object.

The derivations introduced in this section represent the basis for developing the diffraction models for light field microscopy as they will be presented in Chapters 3 and 4.

2.2 Image deconvolution

> This power is what I mean when I talk of reasoning backward.
>
> *Sherlock Holmes,*
> *A Study in Scarlet,*
> *Sir Arthur Conan Doyle (1887)*

When treating an object field as the weighted sum of impulse functions, the image of the object by a microscope can be computed as the weighted sum (by the field amplitude) over the images of these impulse functions.

The recorded image can then be described as:

$$f(x,y) = \iiint |h(x,y,x_p,y_p,z_p)|^2 g(x_p,y_p,z_p) dx_p dy_p dz_p, \tag{2.24}$$

where x, y are the sensor plane coordinates, x_p, y_p, z_p are the 3D object coordinates and the function g describes the light intensity at each point in the imaged object. h is now a 3D PSF function explicitly encoding the axial position of a source point.

Image deconvolution attempts to recover the original object when the captured image and the PSF are available. The term deconvolution is mostly used in the context of image deblurring, where the observed data (captured image) is given by a convolution of the true data (object) with a known kernel (PSF). Here the image and object space coincide. In the absence of noise, the problem is solved in a straight-forward manner via division by the kernel in the Fourier domain. In this sense, image deconvolution is an inverse problem with a translation-invariant forward operator.

The 3D deconvolution problem in light field microscopy, on the other side, is rather a 3D reconstruction problem where the observed data (measurements) and the object to reconstruct come from different spaces. Then, the problem formulation is closer to image reconstruction as in computed tomography than it is to classic 2D image deconvolution in microscopy.

In this section we will address the 3D deconvolution problem in light field microscopy while touching on the basics of the more generic topic of inverse problems.

2.2.1 Inverse problems

Inverse problems are concerned with finding causes for observed effects. In imaging related applications, inverse problems are generally formalized as the restoration or reconstruction of model parameters given measured data and they solve an equation of the form:

$$\mathbf{y} = \mathbf{A}(\mathbf{x}) + \mathbf{e}, \tag{2.25}$$

where $y \in \mathbb{R}^m$ represents the measurements, $x \in \mathbb{R}^n$ the parameters to reconstruct and $A\colon \mathbb{R}^n \to \mathbb{R}^m$ the forward projection operator which explains the directed relation from x to y. $e \in \mathbb{R}^m$ models the observation noise.

The high-level formulation in Eq. 2.25 is encountered in various imaging applications from image denoising, deblurring to image reconstruction in computed tomography, where the forward operator A takes different interpretations.

2.2.1.1 Ill-posedness

In the absence of noise, the exact solution to the problem in Eq. 2.25 is given by the $A^{-1}y$ when A is invertible. In practice, however, we often deal with over-determined linear systems and, moreover, measurements typically contain noise. Solving the problem becomes difficult as the solution is sensitive to perturbations in data. Ill-posedness is defined in contrast with the notion of well-posedness introduced by Hadamard [85] which states that a well-posed problem must have a unique solution x that depends continuously on the data y.

A common approach in dealing with over-determined systems is to look for an approximate solution by minimizing the sum of squared residuals. This is called the "least squares method" which solves the following optimization problem:

$$\arg\min_{x \in \mathbb{R}^n} ||A(x) - y||_2^2. \tag{2.26}$$

2.2.2 Regularization

Regularization adds extra (prior) knowledge during the process of solving an ill-posed problem. It imposes constraints on the solution of the inverse problem (e.g. smoothness, positive definiteness) in order to make the optimal solution unique. For an exhaustive discussion on regularization methods, the reader is referred to [86].

2.2.2.1 Variational methods

The most prominent regularization methods are based on variational methods. These methods develop from optimizing a functional composed of a data term and possibly multiple regularization terms whose influences are controlled via corresponding regularization parameters. Here the idea is to minimize the data misfit penalized by some explicit regularizer [87, 88]:

$$\arg\min_{x \in \mathbb{R}^n} \mathcal{D}\{A(x), y\} + \lambda \mathcal{R}(x). \tag{2.27}$$

This is a generic formulation for optimizing a perturbed inverse problem with a natural plug-and-play structure. The forward operator A takes various implementations based on the prob-

lem at hand. The data discrepancy $\mathscr{D}$ and the regularizer $\mathscr{R}$ are chosen to fit the specific aspects of the inverse problem. $\mathscr{D}$ is a data fitting term and it can be a metric on the data space (often L_1 or L_2 norm) or a transformation over the data log-likelihood for a statistical interpretation of the inverse problem as we will see in the next section. Analogous, the regularizer can take the form of a metric penalty term or the log of a prior distribution for the unknown. Well-known examples of variational methods are classical Tikhonov regularization and TV regularization.

Tikhonov regularization Introduced by Andrey Tikhonov [89], it is arguably the most common variational regularization method:

$$\arg\min_{x\in\mathbb{R}^n} \frac{1}{2}||A(x)-y||_2^2 + \frac{\lambda}{2}||\Gamma x||_2^2. \tag{2.28}$$

In the classical implementation of the Tikhonov regularization Γ is usually chosen as $\Gamma = \mathbb{I}$ and the regularization effect is scaled with λ. The regularizer then penalizes large x in terms of the L_2-norm.

Total variation regularization Another famous explicit regularizer controls the variation given by the gradient of the solution. Rudin *et al.* [90] introduced the total variation (TV) regularization for imaging problems to preserve sharp structures, while removing noise in the images. In the original paper an isotropic and not differentiable total variation norm was proposed for the regularizer:

$$\arg\min_{x\in\mathbb{R}^n} \frac{1}{2}||A(x)-y||_2^2 + \lambda \sum_{ij} \sqrt{D_x \mathbf{x}_{ij}^2 + D_y \mathbf{x}_{ij}^2}. \tag{2.29}$$

D_x and D_y are the horizontal and vertical finite difference operators. Without loss of generality, the TV regularizer assumes that $\mathbf{x}$ is two dimensional for the sake of an explicit expansion of the term.

A commonly employed variation is the "anisotropic TV" as it might be easier to minimize [91]:

$$\arg\min_{x\in\mathbb{R}^n} \frac{1}{2}||A(x)-y||_2^2 + \lambda \sum_{ij} |D_x \mathbf{x}_{ij}| + |D_y \mathbf{x}_{ij}|. \tag{2.30}$$

2.2.3 Statistical Inversion

Statistical inversion is a complete statistical inferential methodology for approaching inverse problems. It addresses these problems from a different angle and interprets the object of inference (the model parameter) as a random variable that follows a prior distribution. This gives

rise to a set of tools from Bayesian inference theory [92–94] for incorporating data statistics into the recovery of the model parameter when solving ill-posed inverse problems. In such frameworks, regularization is incorporated in the form of prior knowledge through an appropriate choice of the prior distribution.

2.2.3.1 Basics of Bayesian inference

So far we have looked at inverse problems from an analytic point of view and aimed at finding a best fit solution $\hat{\mathbf{x}}$. In a statistical inverse problem we solve for a set of solutions by looking at the distribution of the unknown solution rather than a single best fit; this has the effect of improving the conditioning of the problem [95, 96].

When formulating a Bayesian inverse problem the key idea is to treat both the unknown solution and observed data as realizations of random variables. Then the inverse problem can be interpreted as a statistical inference problem.

Let $\mathbf{X} = (X_1, ..., X_n)$ be the random vector for the unknown solution $\mathbf{x}$ and $\mathbf{Y} = (Y_1, ..., Y_m)$ for the measurements $\mathbf{y}$. Likewise, $\mathbf{E}$ models the uncertainty in the observations as additive noise with the associated probability density function $p_{noise} : \mathbb{R}^m \to \mathbb{R}_+$. We can then replace the formulation in Eq. 2.25 by the stochastic analogue below:

$$\mathbf{Y} = \mathbf{A(X)} + \mathbf{E}. \tag{2.31}$$

Assume further that $\mathbf{X} \sim p_{prior}$ and $\mathbf{E} \sim p_{noise}$, then the conditional distribution of $(\mathbf{Y}|\mathbf{X} = \mathbf{x}) \sim p^x_{data}$ is derived from translating p_{noise} by $A(x)$:

$$p^x_{data}(\mathbf{y}|\mathbf{x}) = p_{noise}(\mathbf{y} - A(\mathbf{x})) \tag{2.32}$$

A common model for the above likelihood when dealing with low photon count imaging (as it is the case in fluorescence microscopy) is the Poisson distribution for Y with the mean $\lambda = A(\mathbf{x})$. This approach is used in Chapters 3 and 4 when solving the light field 3D reconstruction problem.

The prior probability density of $\mathbf{X}$, p_{prior} describes the information regarding the distribution of $\mathbf{x}$ prior to recording the measurements. The task of the statistical inference is now to recover the posterior (conditional distribution p^y_{post} of $(\mathbf{X}|\mathbf{Y} = \mathbf{y})$) given a single sample $\mathbf{y}$ from the observed data model.

The posterior density is given in the **Bayes formula** for parameter inference:

$$p^y_{post}(\mathbf{x}|\mathbf{y}) = \frac{p^x_{data}(\mathbf{y}|\mathbf{x}) p_{prior}(\mathbf{x})}{p_Y(\mathbf{y})}, \tag{2.33}$$

where:

- $p^x_{data}(\mathbf{y}|\mathbf{x})$ is the "likelihood" and it quantifies the likeliness of the data when the model parameter is fixed. It is a function of $\mathbf{y}$, while the posterior is a function of $\mathbf{x}$.

- $p_{prior}(\mathbf{x})$ represents the "prior". It comes from prior knowledge (known physical constrains). A good choice of the prior distribution incorporates regularization in the inference process and a great amount of research in Bayesian inference revolves around designing priors. The prior is especially important for problems where there are very few observations from which the posterior can be updated.

- $p_Y(\mathbf{y})$ is the so-called "evidence" representing the marginal density of the observed data:

$$p_Y(y) = \int_{\mathbb{R}^n} p^x_{data}(\mathbf{y}|\mathbf{x}) p_{prior}(\mathbf{x}) dx. \tag{2.34}$$

  $p_Y(\mathbf{y})$ is often ignored as it stays constant with respect to the values of X and only the factors in the numerator of Eq. 2.33 affect the values of the posterior.

The posterior gives the complete solution of the inference problem as it provides the entire distribution for the model parameter. In practice, however, it is often computationally challenging, if not intractable, to calculate the posterior density. Then point estimator methods which compute a single "best" value are commonly used.

2.2.3.2 Point estimators

While Bayesian inference offers a set of tools for fully calculating the posterior probability distribution, in large scale problems the computation can be very intensive or even intractable. By contrast, non-Bayesian statistics calculates point estimates (like maximum likelihood) for the model parameters.

Maximum a posteriori (MAP) estimator This point estimator represents the most likely model parameter $\mathbf{x}$ given the observed data $\mathbf{y}$. It maximizes the posterior probability:

$$\begin{aligned} \hat{\mathbf{x}}_{MAP} = \arg\max_{\mathbf{x}} p^y_{post}(\mathbf{x}|\mathbf{y}) &= \arg\max_{\mathbf{x}} \frac{p^x_{data}(\mathbf{y}|\mathbf{x}) p_{prior}(\mathbf{x})}{p_Y(\mathbf{y})} \\ &= \arg\max_{\mathbf{x}} p^x_{data}(\mathbf{y}|\mathbf{x}) p_{prior}(\mathbf{x}). \end{aligned} \tag{2.35}$$

The advantage of the MAP estimator is that it does not involve integration over X as the posterior is proportional to the numerator in Eq. 2.33 and the denominator can be safely ignored for the maximization purpose. As previously mentioned, the prior may act as a regularizer, so MAP can be useful for solving an ill-posed inverse problem. On the other side, the choice of prior is not always trivial and it can also lead to non-smooth optimization problems that are computationally challenging [96].

Maximum likelihood (ML) estimator This estimator maximizes the data likelihood:

$$\hat{\mathbf{x}}_{ML} = \arg\max_{\mathbf{x}} p^{x}_{data}(\mathbf{y}|\mathbf{x}). \tag{2.36}$$

Since the ML estimator only considers the data likelihood, it neglects the prior and it does not have a regularization effect. ML is equivalent to MAP when the prior is uniformly distributed. Chapters 3 and 4 discuss methods to add regularization after obtaining the ML estimate.

2.2.3.3 Expectation Maximization

The Expectation Maximization (EM) algorithm [97] is a classic iterative method for finding the ML or MAP estimates of unknown parameters in statistical problems involving also latent variables. In this case the maximization problem cannot be solved directly.

Let $\mathbf{Y}$ and $\mathbf{Z}$ be independent and identically distributed random vectors and a vector of unknown parameters $\theta \in \mathbb{R}^n$ along with the density function $p(Y, Z; \theta)$. The random vector $(\mathbf{Y}, \mathbf{Z})$ represents the complete data containing the observed data $\mathbf{Y}$ and unobserved latent (or missing) data $\mathbf{Z}$. The maximum likelihood estimate of θ maximizes the marginal likelihood of the observed data:

$$L(\theta; \mathbf{Y}) = p(\mathbf{Y}|\theta) = \int p(\mathbf{Y}, \mathbf{Z}|\theta) d\mathbf{Z}. \tag{2.37}$$

As we do not know $\mathbf{Z}$ the above sum calculation can be problematic (intractable) and the EM algorithm aims to find the ML estimator by iteratively applying the following two steps:

- Expectation (E) step: computes the expected value of the log-likelihood function with respect to the conditional distribution of $(\mathbf{Z}|\mathbf{Y})$:

$$E_{\mathbf{Z}|\mathbf{Y}}\big(\log L(\theta_{current}; \mathbf{Y}, \mathbf{Z})\big)$$

- Maximization (M) step: computes the ML estimator on the conditional expectation:

$$\theta_{ML} = \text{argmax}_{\theta}\ E_{\mathbf{Z}|\mathbf{Y}}\big(\log L(\theta_{current}; \mathbf{Y}, \mathbf{Z})\big)$$

The EM method is used in Chapters 3 and 4 as part of the MLEM (Maximum Likelihood Expectation Maximization) algorithm for 3D deconvolution.

Part III

Light field microscopy

Chapter 3

Conventional light field microscopy

The work in this chapter was published in:

- A. Stefanoiu, J. Page, P. Symvoulidis, G. G. Westmeyer, and T. Lasser. "Artifact-free deconvolution in light field microscopy." *Optics Express*, 27, pp. 31644-31666, 2019. DOI: 10.1364/OE.27.031644.

3.1 The light field microscope

A light field microscope (LFM) is built by placing a micro-lens array (MLA) into the optical path of a conventional wide-field microscope [44, 58]. Fig. 3.1 shows a ray diagram as an intuitive overview of the light propagation through a LFM. A source point at a depth z in front of the microscope objective has a conjugate image by the tube lens at z''. The objective lens creates a virtual image of the object at z', which is not drawn here for the sake of clarity. We choose to represent z as $f_{obj} + \Delta z$, since an object at depth f_{obj} is usually in focus in the wide field microscope. In order to be consistent with the literature [44, 67], we will call this depth, $z = f_{obj}$, the *native object plane* (NOP) or the *zero plane* of the LFM. Then Δz represents an offset from the native object plane, and we will refer to this quantity when talking about depth in the subsequent sections. Finally, the micro-lenses create micro-images at z''', and the light reaches the camera sensor, producing a raw light field image.

Without loss of generality, Fig. 3.1 depicts a configuration where the conjugate image is formed in front of the MLA. However, our derivations are valid for arbitrary configurations, i.e. they do not discriminate between focused plenoptic [54] and original plenoptic [53, 58] light field imaging designs.

In the early stages, the methods for rendering images from the LFM were limited to lenslet resolution [53], which is the number of available micro-lenses. In [67], Broxton *et al*. introduced a wave-based model to describe the propagation of light through a plenoptic 1.0 LFM setup [58], together with a 3D deconvolution method. They demonstrate superior reconstructions in

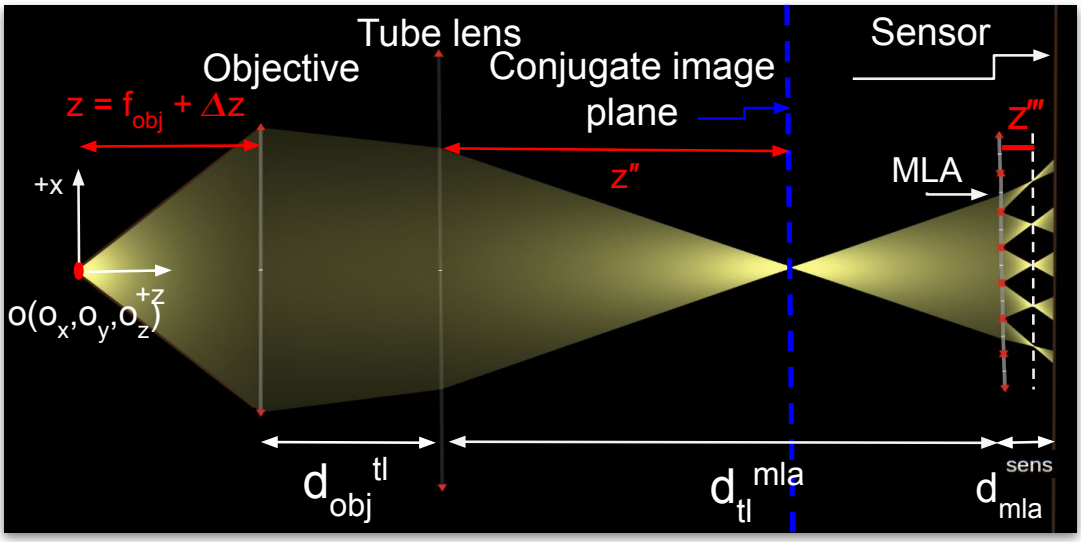

Figure 3.1: Ray diagram of the LFM: light propagation through the light field microscope. f_{obj} denotes for objective focal length, Δz represents the offset from the native object plane (NOP). A source point $\mathbf{o}(o_x, o_y, o_z = z)$ in front of the microscope objective has a conjugate image by the tube lens at z''. Finally, the micro-lenses create micro-images at z''', and the light reaches the camera sensor, producing a raw light field image.

terms of lateral resolution (compared to lenslet resolution) for most of the axial range. The improvement rate, however, is non-uniform across depth, and the recoverable resolution remains low near the native object plane; additionally this region exhibits strong artifacts. This effect is due to the depth-dependent sampling patterns and induced aliasing in light field imaging [57]. As the sample is naturally placed at the native object plane during the acquisition, i.e. in focus, the aliasing artifacts constitute a rather prominent problem in light field microscopy as expressed in [44, 45, 99], undermining the potential of the modality.

The sampling patterns and angular aliasing have previously been studied for light field imaging systems, like camera arrays [100–103]. However, there are fundamental differences between the aliasing in camera arrays and plenoptic devices [57], which must be acknowledged in order to address the cause of the artifacts in LFM deconvolution. Plenoptic devices avoid angular aliasing while introducing considerable spatial aliasing, since neighboring emitters in the scene are projected to pixels far apart on the sensor. Ng *et al*. [53] analyzed aliasing in refocused light fields, and Georgiev *et al*. [104] discussed the impact of the micro-lens array to sensor distance on the sampling rate in plenoptic cameras. In [57, 105], the authors studied the depth-dependent sampling requirements in light field cameras.

3.2 Aliasing in light field microscopy

3.2.1 The depth-dependent sampling patterns of the LFM

We now proceed at investigating the sampling requirements of the LFM and deriving the depth-dependent quantities relevant for our algorithm, similar to the analysis of sampling patterns in plenoptic cameras [57].

Fig. 3.2 is meant to build an intuition on the depth-dependence of the sampling patterns of the plenoptic microscope. The source points at z_0 in front of the microscope (circled in red) have completely overlapped images at the sensor plane. On the other side, the source points in the blue group have partially non-overlapping images on the sensor, while being sampled at the same rate as the points in the red group, but they originate from a different depth z_1. The points in the green group, also at z_1, are being sampled at a higher rate such that their images on the sensor are fully non-overlapping.

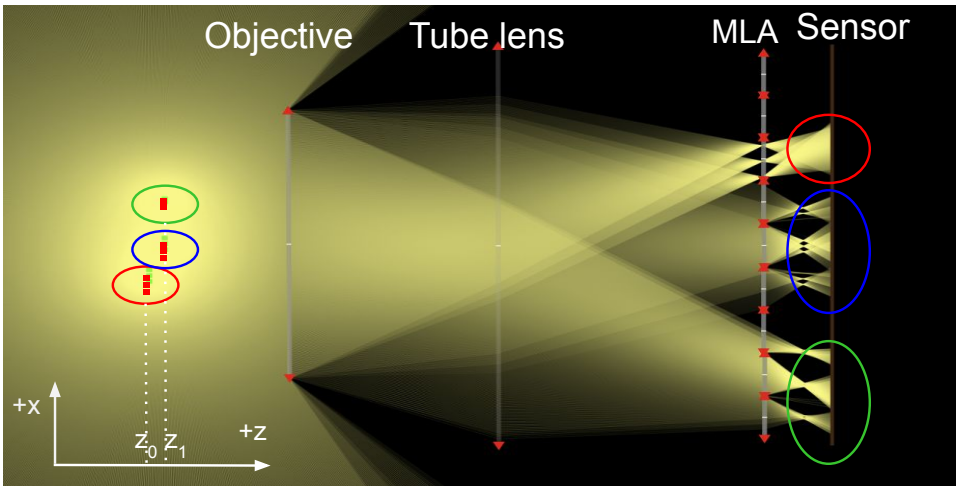

Figure 3.2: Depth-dependent aliasing in LFM: The source points in the red group at depth z_0 in front of the microscope have completely overlapped images at the sensor plane. The points in the blue group, while being sampled at the same rate as the points in the red group, show partially non-overlapping images on the sensor as they are placed at depth z_1. The points in the green group, on the other side, are also placed at z_1; however they are sampled at a higher rate and their images are fully non-overlapping.

In order to characterize the depth-dependent nature of the sampling in light field microscopy, let us assume for now that the micro-lenses have very small apertures and behave like pinholes. Then we can approximate the MLA by an array of pinholes with spacing p_{ml}. The in-camera light field at the MLA (pinholes in this context) should be band-limited with a bandwidth of $f_0 = \frac{1}{2d}$ in order to satisfy the Nyquist criteria [106]. Higher frequencies, outside this bandwidth, would be under-sampled by the pinhole array and appear aliased.

Since the sensor elements have a finite extent, we must look into what area the pixels effectively integrate over. Fig. 3.3(a) illustrates how the image at the MLA scales to the actual image that forms under a micro-lens. For a clear visualization, we omit here the first part of

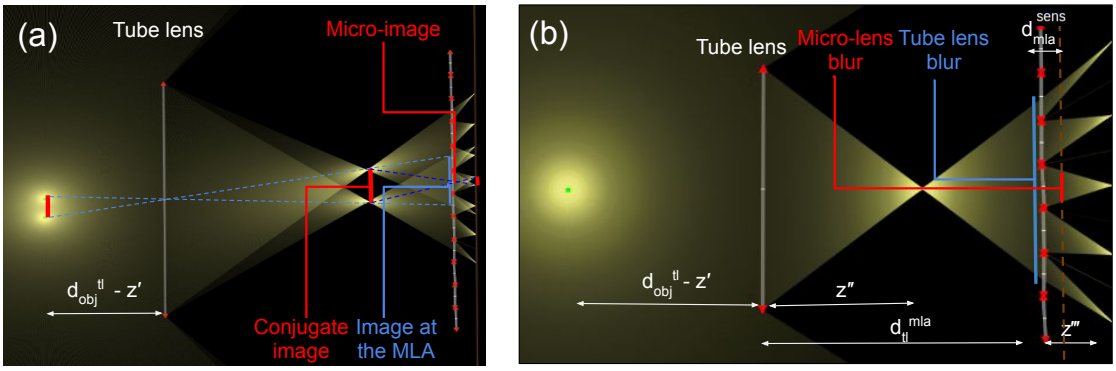

Figure 3.3: **(a) Micro-lens magnification**: The image of an object under a micro-lens scales according to the object depth. **b) Micro-lens blur**: The geometric blur radius behind a micro-lens is again depth-dependent.

the image formation and assume we have an image of an object at z in front of the objective formed at z' by the objective lens. The tube lens further creates a scaled image at the conjugate image plane (dark blue), z''. The image at the MLA (light blue) follows from tracking the chief rays. Finally, we pick a micro-lens and derive the micro-image behind it. By means of similar triangles, the size of the image under a micro-lens is the size of the image at the MLA, scaled by a factor:

$$\gamma_z = \frac{d_{mla}^{sens}}{d_{tl}^{mla}} \left| \frac{z''}{d_{tl}^{mla} - z''} \right|. \tag{3.1}$$

The scaling amount γ_z is depth-dependent, which means the actual area of the light field the sensor pixels integrate over varies with the object depth.

An interesting observation follows for telecentric microscopes (4f-systems as the ones in [44, 67]). For these systems, although the magnification stays constant with object depth, the blur radius at the MLA (depicted in blue in Fig. 3.3(b)) varies in extent with depth,

$$B_z = r_{tl} \left| \frac{d_{tl}^{mla} - z''}{z''} \right|. \tag{3.2}$$

Here, r_{tl} is the effective tube lens radius. Consequently, the depth-dependent scaling factor γ_z still applies, as we can write

$$\gamma_z = \frac{d_{mla}^{sens}}{d_{tl}^{mla}} \frac{r_{tl}}{B_z}. \tag{3.3}$$

Please note the relation to the magnification factor in [57], or the amount of refocusing in [62].

If we now drop the pinhole array approximation and consider a micro-lens with finite aperture p_{ml}, we have to take into account the additional blur they introduce. The depth-dependent blur under each micro-lens, depicted in red in Fig. 3.3(b), has a radius

$$b_z = r_{ml} \left| \frac{1}{z'''} - \frac{1}{d_{mla}^{sens}} \right|, \tag{3.4}$$

where $r_{ml} = \frac{p_{ml}}{2}$ is the radius of the micro-lens.

We have now derived all the ingredients we need to characterize the non-aliasing requirements of the LFM.

3.2.2 Anti-aliasing filters

The band-limited assumption we made in the previous section for the pinhole approximation of the MLA means the acquired light field is the conjugate light field at z'', convolved by a low-pass ideal (sinc) filter with cutoff frequency $\frac{1}{2d}$. We define the sinc kernel radius as the first zero crossing of the filter, p_{ml}. Then, as every micro-image is the projection of the conjugate light field onto the sensor, we can project the filter in the same way. Employing eq. (3.1), the scaled filter kernel has a radius of $\gamma_z d$.

When we take into account the finite micro-lens apertures p_{ml}, the pixels effectively integrate over a larger area and the aliasing is reduced with the micro-lens blur b_z. Then the filter size at the sensor, accounting for the micro-lens blur, is:

$$w_{sens_z} = \left| \gamma_z p_{ml} - b_z \right|. \tag{3.5}$$

In the case where the conjugate image forms at the MLA ($z'' \to d_{tl}^{mla}$), we have $z''' \to 0$ and $b_z \to \infty$. However, the micro-lens blur actually converges to the size of the micro-image and thus we restrict the maximum filter radius to r_{ml}:

$$w_{sens_z} = \min\left(\left| \gamma_z p_{ml} - b_z \right|,\ r_{ml} \right). \tag{3.6}$$

We now backproject the filter into the object space. For this we introduce the super-resolution factor, $s \in \mathbb{Z}$, as defined in [67]. If we sample the volume at a rate of s times the lenslet resolution p_{ml}, then the voxels are spaced by $\frac{p_{ml}}{Ms}$, where M is the objective magnification factor. Then the radius of our ideal filter kernel in pixels in object space is:

$$w_{obj_z} = \frac{w_{sens_z} s}{p_{ml}}. \tag{3.7}$$

Fig. 3.4 illustrates the scaled pinhole filter radius together with the micro-lens blur radius and the final compensated anti-aliasing filter radius in pixels over an axial range $[-100, 100]\mu m$ for an example plenoptic 1.0 LFM configuration as in Fig. 3.5(a). An important observation here is that, as we move away from the zero plane, the LFM samples at a higher rate, imposing milder anti-aliasing requirements.

Finally, we define $h_{f_{w,z}}$ as the anti-aliasing normalized resampling filter. $h_{f_{w,z}}$ is a depth-dependent ideal low-pass filter and its kernel size at each depth is given by w_{obj_z}.

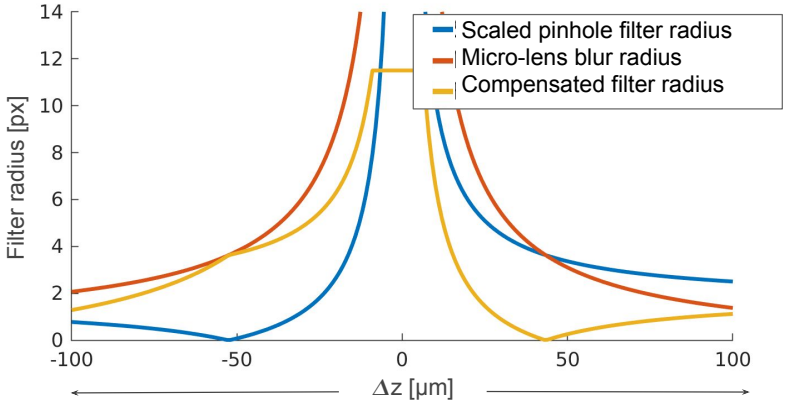

Figure 3.4: Anti-aliasing filter radius over depth: In the original LFM design [58, 67] (see Fig. 3.5(a)), the NOP is sampled at the coarsest rate by the LFM which implies our resampling anti-aliasing filter has the largest radius at this object depth. As we move away from the *zero plane*, the LFM sampling rate increases and the anti-aliasing requirements become milder.

Since the ideal filter is of unit value for all the frequencies inside the band-limit, and zero outside, it has infinite extent. In practice, we need to use an approximate non-ideal filter kernel, aiming at optimizing the unity gain in the pass-band and zero gain in the stop-band. While there are extensive filter design choices [106], for all the experiments shown in this work, we obtained satisfying results using a Lanczos2 windowed version of the sinc kernel.

3.3 The generalized light field point spread function

In this section we propose a generalized forward light propagation model describing the optical system's impulse response for arbitrary LFM configurations (i.e. the light field point spread function, LFPSF). Fig. 3.5 depicts such plenoptic configurations, where the micro-lens array is placed at the native image plane (left), behind (center) or in front of it (right). Experimentally acquired LFSPFs are shown on top for each setup.

In order to derive the diffraction pattern of a source point $\mathbf{o}(o_x, o_y, o_z)$, when the light propagates through the LFM from the source to the camera sensor, we discuss the wavefront at intermediate key planes in the following subsections.

3.3.1 The wavefront at the MLA plane

In order to evaluate the wavefront incident on the MLA produced by a source point in front of the microscope, we employ Abbe imaging theory for 4-f optical systems [81]. We proceed to find the "focused" configuration for our scenario. In Fig. 3.6(b) FOP represents the focused object plane, which is the depth in the object space that is imaged exactly at the MLA by the tube lens. This plane is then located at offset Δ_{NOP} from the native object plane. If we

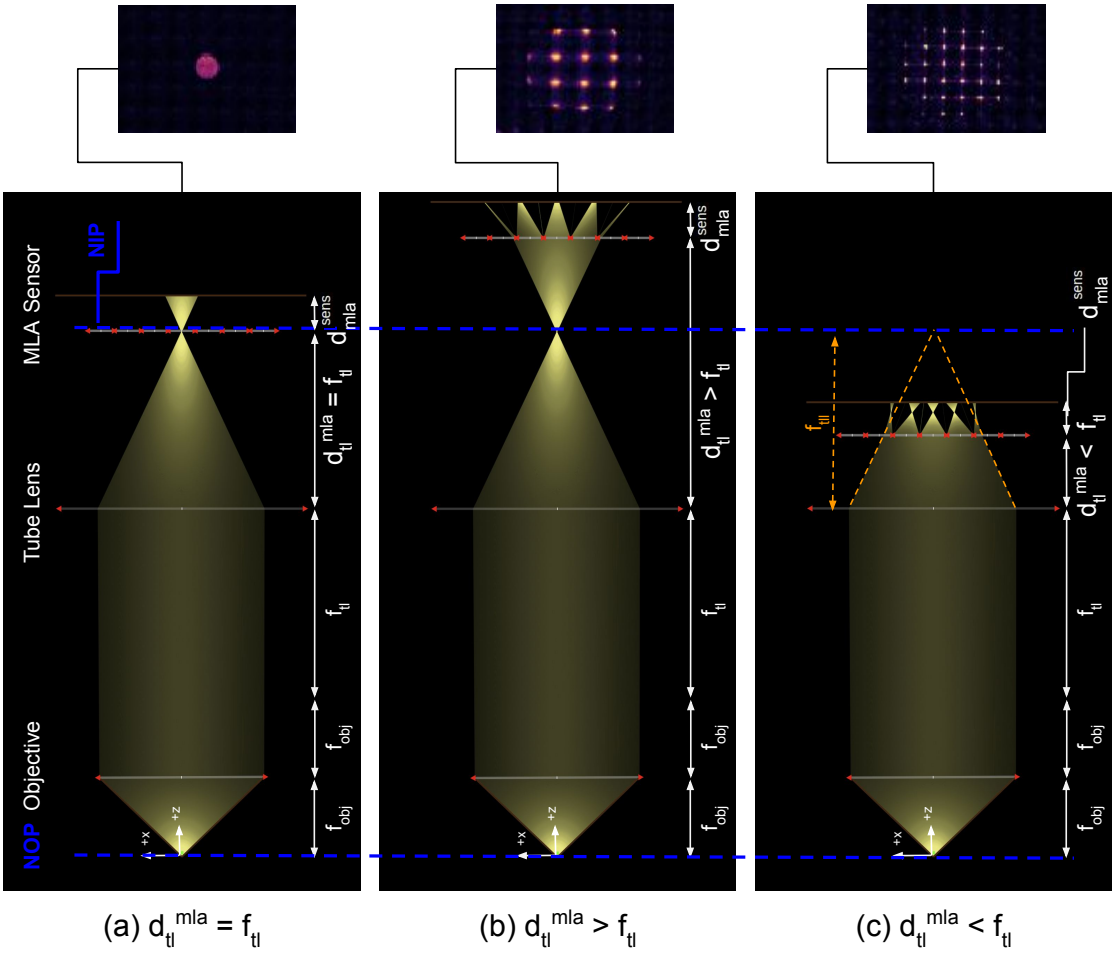

Figure 3.5: LFM configurations and their light propagation paths. (a) The original design as described in [58, 67]. The objective and tube lens are arranged as a 4-f (tele-centric) system. The native object plane (NOP) is then defined at the f_{obj} in front of the microscope objective and the native image plane (NIP) follows at f_{tl} behind the tube lens. The MLA is then placed at the NIP. The camera is behind the MLA at an offset $d_{mla}^{sens} = f_{ml}$. **(b) and (c) Defocused LFM** (similar to the 2.0 / focused plenoptic camera [54] design). The MLA is now placed behind the NIP (b) or in front of it (c), such that the NOP is not focused on the MLA. In the latter scenario, the virtual image that would form at the NIP is depicted in dashed orange. **Top**: experimentally acquired LFPSF of a point source at the NOP, $\mathbf{o}(o_x, o_y, o_z) = (0, 0, f_{obj})$ for each setup.

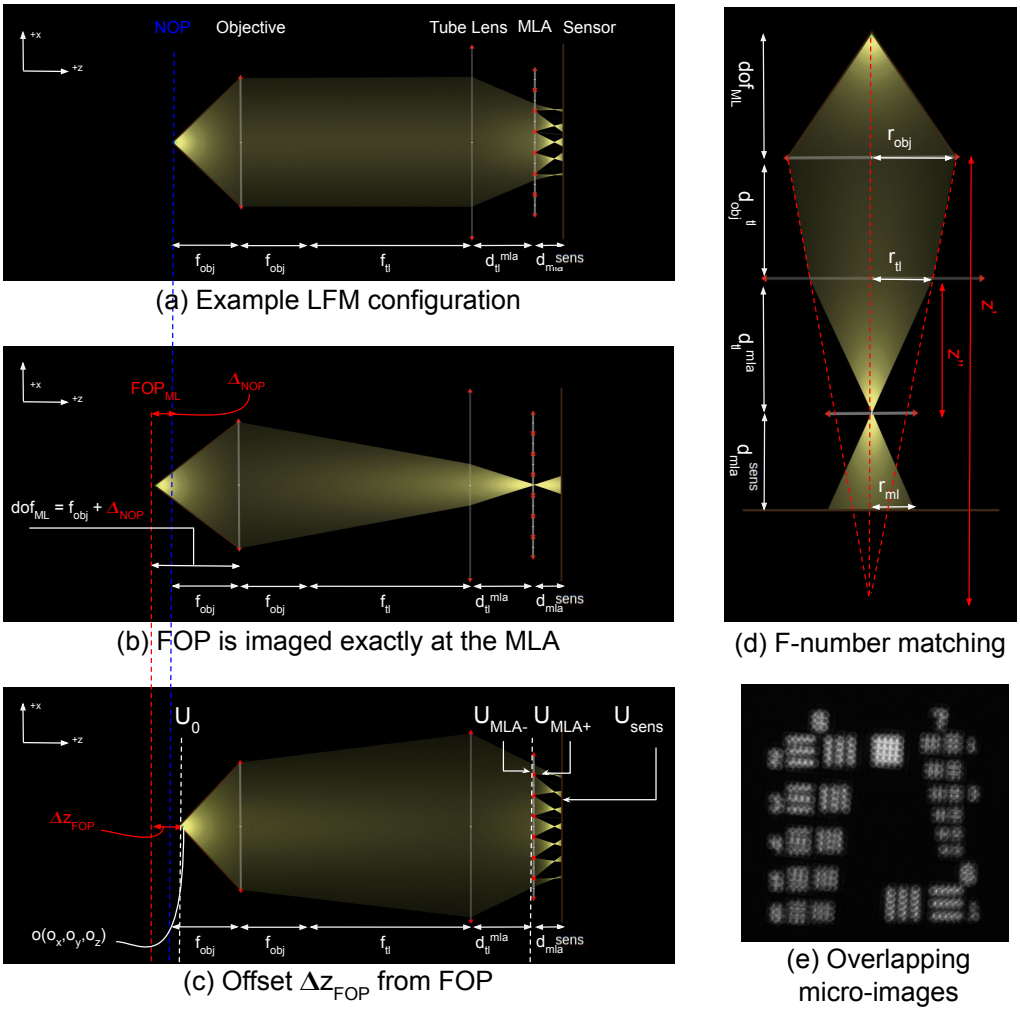

Figure 3.6: **(a) Example defocused LFM** configuration with $d_{tl}^{mla} < f_{tl}$. **(b) The "focused" object depth** for our LFM in (a). FOP represents the focused object plane which is imaged exactly at the MLA by the tube lens. FOP is then located at offset Δ_{NOP} from NOP. Then an object focused on the MLA by our microscope is placed at $dof_{mla} = f_{obj} + \Delta_{NOP}$ in front of the objective. **(c)** Δz_{FOP} represents the depth offset from the FOP for a source point, $\mathbf{o}(o_x, o_y, o_z = \Delta z_{FOP} + dof_{mla})$. **(d) Optimal sensor plane coverage condition:** The micro-lens blur radius for a source point $\mathbf{o}(o_x, o_y, o_z = dof_{mla})$ needs to match the micro-lens radius r_{ml}, in order to ensure optimal sensor plane coverage, without overlapping micro-images. **(e) Overlapping micro-images** due to violation of criteria in eq. (3.17).

introduce $\Delta_{MLA} = d_{tl}^{mla} - f_{tl}$ to be the signed distance between the MLA plane and the tube lens, we can write:

$$\Delta NOP = \frac{1}{M^2}\Delta_{MLA}, \tag{3.8}$$

where $\frac{1}{M^2}$ is the axial magnification factor [81].

We now introduce the axial coordinate $dof_{mla} = f_{obj} + \Delta_{NOP}$ as the object space depth that is focused on the MLA by our 4-f microscope. Then a source point $\mathbf{o}(o_x, o_y, o_z = dof_{mla})$ produces a convergent wavefront exactly at the MLA plane; see Fig. 3.6(b).

Having defined these quantities, we can express any source point $\mathbf{o}(o_x, o_y, o_z)$ relative to the FOP of our LFM setup as $\mathbf{o}(o_x, o_y, o_z = dof_{mla} + \Delta z_{FOP})$, see Fig. 3.6(c). Then we observe a defocused wavefront at the MLA plane:

$$\begin{aligned} U_{mla-}(\mathbf{o}, x_{mla}, y_{mla}) = &\frac{deM}{{o_z}^2\lambda^2}\exp\left(-\frac{iu}{4\sin^2(\alpha/2)}\right)\cdot \\ &\int_0^{\alpha} P(\theta)\exp\left(-\frac{iu\sin^2(\theta/2)}{2\sin^2(\alpha/2)}\right)J_0\left(\frac{\sin(\theta)}{\sin(\alpha)}v\right)\sin(\theta)\,d\theta, \end{aligned} \tag{3.9}$$

which is the Debye integral for circular lens apertures. $deM = \frac{dof_{mla}}{d_{tl}^{mla}}$ is the demagnification factor, $\alpha \approx \arcsin(NA/n)$ is the maximum entrance angle of the objective aperture, λ is the wavelength of the monochromatic light we assume, $P(\theta)$ is the apodization function of the microscope, J_0 the zeroth order Bessel function of the first kind, and v, u are the normalized radial and axial optical coordinates respectively, given by:

$$\begin{aligned} v &= \frac{2\pi}{\lambda}\sqrt{(x_{mla} - o_x)^2 + (y_{mla} - o_y)^2}\cdot sin(\alpha), \\ u &= \frac{8\pi}{\lambda}\Delta z_{FOP}\cdot sin^2(\alpha/2), \end{aligned} \tag{3.10}$$

Δz_{FOP} represents the depth offset from the FOP for a source point, $\mathbf{o}(o_x, o_y, o_z = \Delta z_{FOP} + dof_{mla})$. In order to stay consistent with the convention and for the clarity of the subsequent discussion, we will still refer to Δz ($o_z = \Delta z + f_{obj}$) as the axial range of an object, via the following convenient substitution:

$$\Delta z_{FOP} = \Delta z + \Delta_{NOP} \tag{3.11}$$

An immediate observation follows when $\Delta_{NOP} = 0$, then $dof_{mla} = f_{obj}$ and $d_{tl}^{mla} = f_{tl}$. This is the original LFM configuration, and eq. (3.9) is equivalent to the defocused PSF at the native image plane proposed in Broxton *et al.* [67].

Similar to us, in [50] the authors compute the wavefront at the MLA in a defocused LFM setup. They first model the PSF at the NIP as in [44, 67] and then propagate the wavefront for

a Δ_{MLA} distance via Fresnel diffraction integral. In theory this is equivalent to our approach. In practice, however, FFT-based Fresnel propagation is implemented via its transfer function, which is a chirp function, and special sampling regimes have to be considered. This implies not only a computational overkill, but such requirements depend on the propagation distance and under-/over- sampling of the angular spectra introduce artifacts in the observation plane [107].

3.3.2 The MLA transmittance

Having computed the light field at the plane immediately before the MLA, we account now for the effect of the MLA. The field U_{mla+} immediately after the MLA is given by:

$$U_{mla+}(\mathbf{o}, x_{mla}, y_{mla}) = U_{mla-}(\mathbf{o}, x_{mla}, y_{mla}) \cdot T(x_{mla}, y_{mla}), \tag{3.12}$$

where the MLA transmittance function T is modeled by replicating the single lenslet transmittance in a tiled fashion as in [67]:

$$T = rep_{d,d}\big(t(x_l, y_l)\big), \tag{3.13}$$

with $rep_{d,d}$ the 2D replication operator and p_{ml} the spacing between micro-lenses. $t(x_l, y_l)$ is the complex transmittance function of a lenslet with local lenslet coordinates, (x_l, y_l):

$$t(x_l, y_l) = P(x_l, y_l) e^{\frac{ik(x_l^2 + y_l^2)}{2f_{ml}}}. \tag{3.14}$$

The exponential term is responsible for the phase change in the incident light, while $P(x, y)$ represents the pupil function, where $P(x, y) = circ_d(x, y)$ for circular aperture lenslets or $P(x, y) = rect_d(x, y)$ for squared shaped lenslets. $k = \frac{2\pi}{\lambda}$ is the wavenumber.

3.3.3 MLA to sensor light field propagation

We now address the propagation of the field from the MLA plane to the camera plane. Since we aim to model arbitrary distances between the MLA and the sensor, without restricting the d_{mla}^{sens} distance to satisfy the Fresnel number (paraxial assumption) [67], we use the more accurate Rayleigh-Sommerfeld diffraction solution [108] to predict the light field at the sensor plane:

$$U_{sens}(\mathbf{o}, x_s, y_s) = \mathscr{F}^{-1}\Big\{\mathscr{F}\big\{U_{mla+}(\mathbf{o}, x_s, y_s)\big\} \cdot H_{rs}(f_X, f_Y)\Big\}, \tag{3.15}$$

where (x_s, y_s) are the image plane coordinates, $\mathscr{F}$ denotes the Fourier transform, and (f_X, f_Y) are the spatial frequencies at the sensor plane. H_{rs} is the Rayleigh-Sommerfeld transfer function:

$$H_{rs}(f_X, f_Y) = e^{\left(ik \cdot d_{mla}^{sens} \sqrt{1-(\lambda f_X)^2-(\lambda f_Y)^2}\right)} \tag{3.16}$$

3.3.4 F-number matching condition for defocused LFM setups

In order to ensure the micro-images optimally fill the sensor plane without overlapping when acquiring light field images, the effective image-side NA of the tube lens needs to match the effective NA of the micro-lenses.

As depicted in Fig. 3.6(d), it is important to notice that a point source $\mathbf{o}(o_x, o_y, o_z = dof_{mla})$, generates the largest response (blur) behind a micro-lens. Conversely, as we move away from dof_{mla}, the micro-lens blur radius, b_z decreases. Thus, we only need to constrain the maximum blur radius, $b_{dof_{mla}}$ to match the micro-lens radius r_{ml} in order to ensure optimal non-overlapping sensor plane coverage. From Fig. 3.6(d) it quickly follows:

$$\frac{r_{tl}}{d_{tl}^{mla}} = \frac{r_{ml}}{d_{mla}^{sens}}, \tag{3.17}$$

where r_{tl} represents the effective tube radius; the radius of the field distribution incident on the tube lens by a source point at dof_{mla} in front of the microscope. In practice, we compute the r_{tl} following the marginal rays:

$$r_{tl} = r_{obj}\left|1 - \frac{d_{obj}^{tl}}{z'}\right|, \tag{3.18}$$

where z' is obtained using the thin lens equation and $d_{obj}^{tl} = f_{obj} + f_{tl}$ for 4f microscopes.

An immediate observation follows that when $d_{tl}^{mla} = f_{tl}$ and $d_{mla}^{sens} = f_{ml}$, we have $r_{tl} = r_{obj}$, and eq. (3.17) is equivalent to $\frac{M}{2NA_{obj}} = \frac{f_{ml}}{p_{ml}}$, where M is the objective magnification and NA_{obj} the objective numerical aperture. This is the f-number matching condition for the original LFM [58, 67].

While violations of eq. (3.17) result in either suboptimal sensor plane coverage or overlapping micro-images (see Fig. 3.6(e)), the LFPSF we derived in the current section allows for arbitrary $d_{tl}^{mla}, d_{mla}^{sens}$ combinations and is consequently not limited to f-number matching configurations.

3.4 Aliasing aware 3D deconvolution

Having discussed the non-aliasing sampling requirements of the LFM and derived the generalized LFPSF, we now turn our attention to incorporating this prior knowledge into the reconstruction process of computing a 3D volume from a light field image.

In [67], Broxton *et al*. introduced a wave-based model to describe the propagation of light through a plenoptic 1.0 LFM setup [58], together with a 3D deconvolution method. They demonstrate superior reconstructions in terms of lateral resolution (compared to lenslet resolution) for most of the axial range. The improvement rate, however, is non-uniform across depth, and the recoverable resolution remains low near the native object plane; additionally this region exhibits strong artifacts. This effect is due to the depth-dependent sampling patterns and induced aliasing in light field imaging [57]. As the sample is naturally placed at the native object plane during the acquisition, i.e. in focus, the aliasing artifacts constitute a rather prominent problem in light field microscopy as expressed in [44, 45, 99], undermining the potential of the modality.

3.4.1 The discretized imaging model

Given the raw noisy light field sensor measurements $\mathbf{m} = (m_j)_{j\in J}$ acquired by pixels $j \in J$ ($|J| = m$) we seek to recover the fluorescence intensity at each discrete point in the volume which produced these measurements.

We represent the discretized volume $\mathbf{v}$ by a coefficient vector $(v_i)_{i\in I}$ with $|I| = n$. Note that the sampling rate in $\mathbf{v}$ is dictated by the super-resolution factor s defined in the previous section. We now denote the detection probabilities

$$a_{ji} = P\big(\text{photon counted at sensor element } j \mid \text{emission occurred in voxel } i\big). \tag{3.19}$$

Due to the low photon counts in fluorescence microscopy, we define the number of photons emitted at voxel i and detected by sensor element j as random variables z_{ji} with $z_{ji} \sim \text{Poisson}(v_i a_{ji})$, which we combine into the the iid random vector $\mathbf{z} = (z_{ji})_{j\in J, i\in I}$.

Our measurements $\mathbf{m} = (m_j)_{j\in J}$ arise from z_{ji} as $m_j = \sum_{i\in I} v_i a_{ji}$, yielding the stochastic imaging model

$$\mathbf{m} \sim \text{Poisson}(A\mathbf{v}), \tag{3.20}$$

where $\mathbf{m}$ denotes the light field measurement, $\mathbf{v}$ denotes the discretized volume we seek to reconstruct, and the operator $A = (a_{ji})_{j\in J, i\in I}$ describes the light field forward model, which is effectively determined by the discretized version of the LFPSF in eq. (3.15). For each point in a fluorescent object the image intensity is given by the modulus squared of its amplitude [81]:

$$a_{ji} = \left|U_{sens}(\mathbf{o}(i), \mathbf{x}_s(j))\right|^2, \tag{3.21}$$

where $\mathbf{o}(i)$ is the object space coordinate of voxel i and $\mathbf{x}_s(j)$ is the coordinate of the pixel j.

3.4.2 Estimate-Maximize-Smooth algorithm

We now consider the estimation of $\mathbf{v}$ by maximizing the Poisson log-likelihood

$$L(\mathbf{z} \mid \mathbf{v}) = \sum_{j \in J} \sum_{i \in I} v_i a_{ji} + z_{ji} \ln v_i a_{ji} - \ln z_{ji}!. \tag{3.22}$$

If we look at $\mathbf{z}$ as the complete version of the incomplete data $\mathbf{m}$, the expectation maximization approach provides an iterative two-step scheme for increasing the likelihood of the current estimate $\mathbf{v}$. In the first step, $\mathbf{z}$ is estimated by computing the conditional expectation $E(z_{ij}|\mathbf{m}, \mathbf{v})$, and in the second step, the maximum likelihood estimate of $\mathbf{v}$ is found, starting from an initial guess $\mathbf{v}^0$:

$$\hat{z_{ji}} = m_j \frac{v_i^q a_{ji}}{\sum_{l \in I} v_l^q a_{jl}} \tag{3.23}$$

$$v_i^{q+1} = \frac{v_i^q}{\sum_{j \in J} a_{jl}} \sum_{j \in J} \frac{m_j a_{ji}}{\sum_{l \in I} v_l^q a_{jl}} \tag{3.24}$$

This is the well known MLEM algorithm, and eq. (3.24) also corresponds to the popular Richardson-Lucy [109] iterative update, which in matrix-vector notation reads:

$$\mathbf{v}^{q+1} = \frac{\mathbf{v}^q}{A^T \mathbf{1}} \left[A^T \frac{\mathbf{m}}{A\mathbf{v}^q} \right]. \tag{3.25}$$

We now propose an additional straightforward step in which we filter the result of eq. (3.23) and eq. (3.24) using the depth-dependent anti-aliasing filters $h_{f_{w,z}}$ that we derived in the previous section. Then the aliasing aware update scheme reads:

$$\textbf{EMS:} \qquad \mathbf{v}^{q+1} = h_{f_{w,z}} * \frac{\mathbf{v}^q}{A^T \mathbf{1}} \left[A^T \frac{\mathbf{m}}{A\mathbf{v}^q} \right], \tag{3.26}$$

where $*$ represents the convolution operator.

The reconstructed $\mathbf{v}$ has a uniform lateral resolution across depths as imposed by the depth invariant discretization we choose; see the super-resolution factor s in the previous section. However, the non-aliasing sampling requirements of the LFM vary across depth, and the actual details that can be recovered depend on these patterns, among other factors.

Moreover, as our model does not incorporate explicit depth priors, information from one depth appears aliased when wrongly projected to another depth. This behavior is present from the first iteration of the Richardson-Lucy scheme, resulting in strong artifacts at the highly undersampled depths where the process fails to converge. Thus, the resampling correction (by depth-dependent filtering) we propose is absolutely necessary.

The filtering in eq. (3.26) can be interpreted as projecting $\mathbf{v}^{q+1}$ to the set of true solutions, which consists of frequencies below the bandwidth dictated by the LFM sampling requirements at each reconstructed depth.

3.4.3 Convergence of the proposed scheme

In order to show convergence of our proposed algorithm, we use the results of [110], in which a similar EMS algorithm with a smoothing kernel S is investigated. The authors in [110] demonstrate a modified (weighted) EMS algorithm with desirable convergence properties using a weighted smoothing kernel $T = W^{-1}SW$, where $W = \text{diag}(w_i)$ and $w_i^{q+1} = s_i^{1/2} e_i^{1/2} \theta_i^q$. According to Lemma in Section 5.3 in [110], S and T will have approximately the same effect if S and W satisfy the three requirements:

1. $S_{ji} \geq 0, \forall i, j$,
2. $\sum S_{ji} = 1$,
3. $|\frac{w_i}{w_j} - 1| \leq \delta$ when $S_{ji} \neq 0$ for some $\delta > 0$.

In our context, s_i is the size of the voxel i, $e_i = \sum_{j \in J} a_{ij}$ and $\theta_i^q = (\frac{v_i}{s_i})^{1/2}$. For our smoothing kernel, $h_{f_{w,z}}$, the first two requirements are trivially fulfilled. Regarding the third requirement, as we use a uniform sampling of our volume, we have $s_i = s_j \forall i, j$. Also $\forall i, j$ where $h_{f_{w,z}}$ is non-zero, we have $\theta_i^q \simeq \theta_j^q$, as the effective sampling rate is higher than the kernel radius. The same argument holds for e_i and e_j, since the columns a_i and a_j act on regions of $\mathbf{v}$ at most as large as the effective sampling rate of the LFM. Thus we can conclude $w_i \simeq w_j$ when $S_{ji} \neq 0$ and δ small.

3.5 Experimental results

All experiments in this work were performed with a custom-built LFM setup, configured as a 4-f system, combining a 0.5 NA with 20× magnification objective lens, and a tube lens with focal length $f_{tl} = 165mm$. We used a f-number matching square-shaped aperture MLA with $150\mu m$ micro-lens pitch and $3000\mu m$ focal lengths. The pixel pitch of the sCMOS camera is $6.5\mu m$, yielding a total of 23×23 pixels behind a micro-lens.

All the results we discuss in this section were reconstructed at sensor resolution, i.e. at a super-resolution factor $s = 23$, which translates to a uniform lateral resolution of $0.33\mu m$. Note, this refers to the sampling rate we chose for rendering the volumes and has nothing to do with the actual details that can be recovered, which is the effective resolution of the LFM. We refer the interested reader to existing discussions on the subject [56, 58, 111].

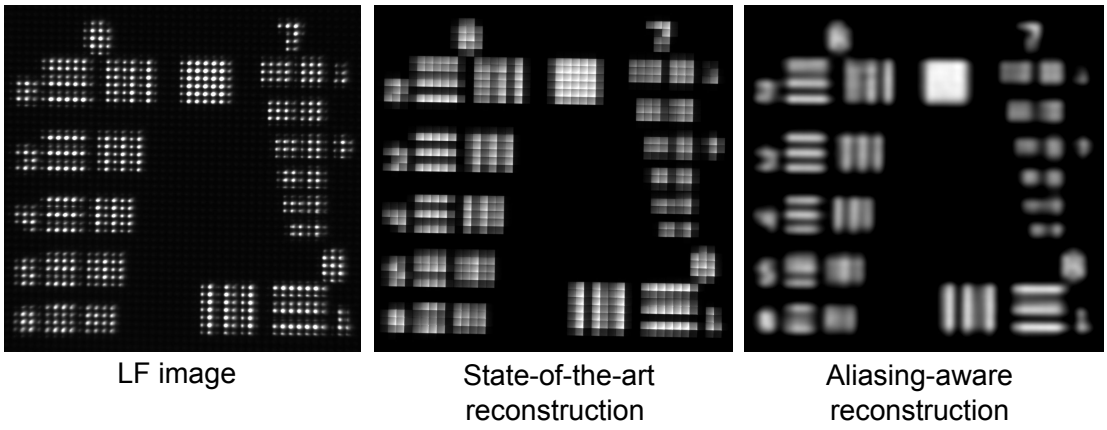

Figure 3.7: (c) Reconstruction of the USAF 1951 target: *Left:* a light field image of the USAF 1951 resolution target, acquired with our experimental LFM. *Center:* reconstructed target using the method in [67]. Specific aliasing artifacts are present. *Right:* artifact-free reconstruction using our aliasing-aware deconvolution method.

3.5.1 Artifact-free deconvolution

In order to show the full potential of our method and to be able to use the method [67] as a baseline for comparison, the experiments in this section were done with the LFM in the original plenoptic 1.0 configuration, i.e. $d_{tl}^{mla} = f_{tl}$ and $d_{mla}^{sens} = f_{ml}$. Then the zero plane ($\Delta z = 0\mu m$) has a conjugate image exactly at the MLA and is the most under-sampled, exhibiting the most artifacts.

As the first experiment, a USAF 1951 resolution target was imaged at $\Delta z = 0\mu m$ using the LFM, see Fig. 3.7 (left) for the raw light field image. Fig. 3.7 shows the reconstruction using the baseline method from [67] (center), and it is obviously riddled with the typical zero plane artifacts. Conversely, Fig. 3.7 (right) shows the reconstruction of the same light field image with our proposed aliasing-aware algorithm, exhibiting a natural appearance with no artifacts.

As discussed in Section 3.2.2, when moving away from $\Delta z = 0\mu m$, we need milder anti-aliasing filters to remove the artifacts while keeping the details in the reconstruction. This effect is illustrated in Fig. 3.9, which shows the reconstruction of an eyeball of a zebrafish larvae (5 days post fertilization, expressing green fluorescent proteins) over a depth range of $[-50, 50]\mu m$; due to space constraints we only show several lateral slices through the volume.

Figs. 3.9(a) and 3.9(c) show the reconstruction with the baseline method in [67] and the artifacts are strongly present at depths close to the zero plane, while they fade out as we move further away from this plane, see for example the slice at $\Delta z = 25\mu m$. In Figs. 3.9(b) and 3.9(d) we show the reconstruction of the same light field data using our proposed method. The depth-dependent filter radius is shown in Fig. 3.4; note here how the kernel radius drops as the artifacts fade away. Our deconvolution produces superior artifact-free results compared to the reference method without over-smoothing, as the depth-dependent filter is dictated by

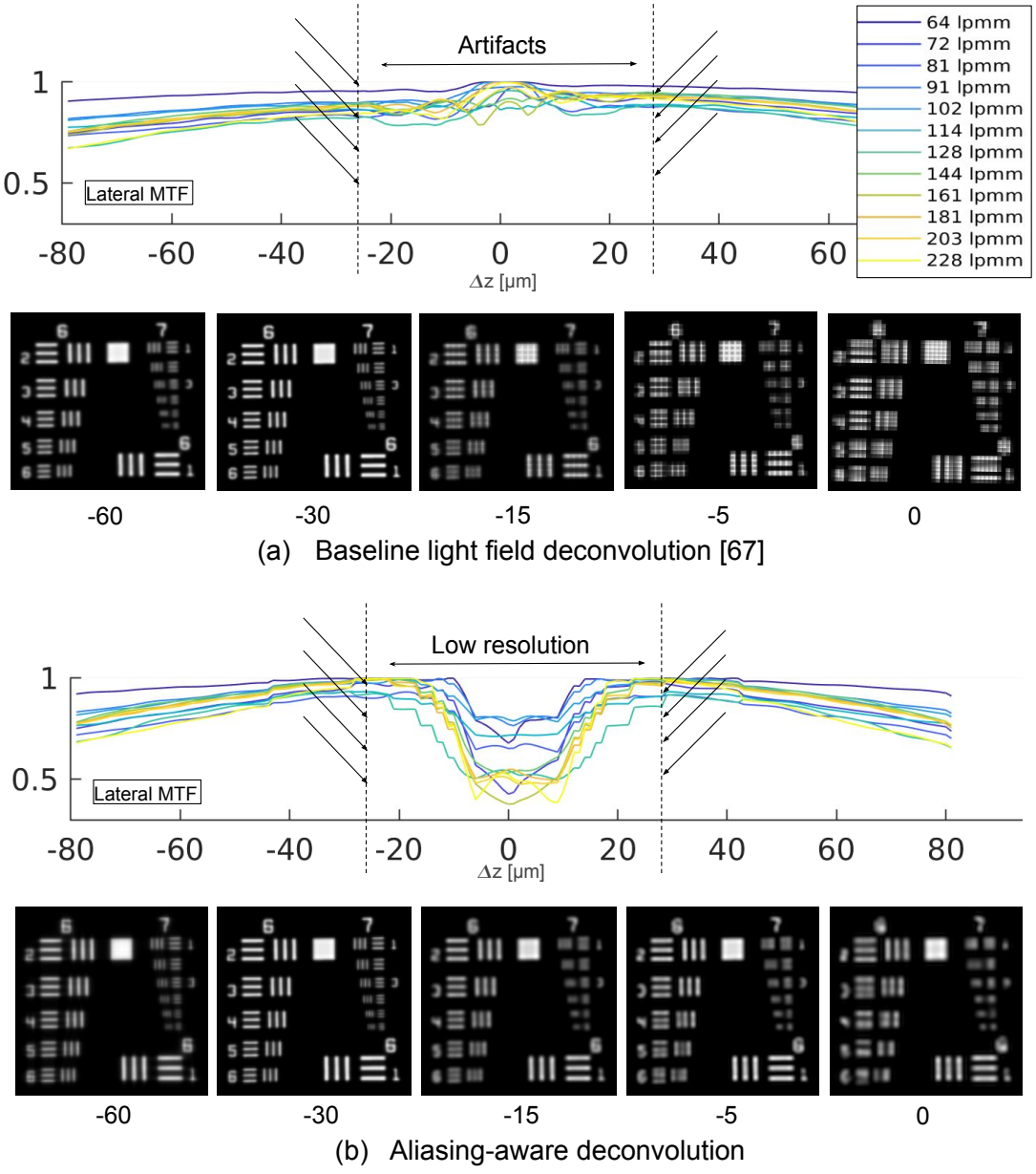

Figure 3.8: Lateral resolution limits of the deconvolution.

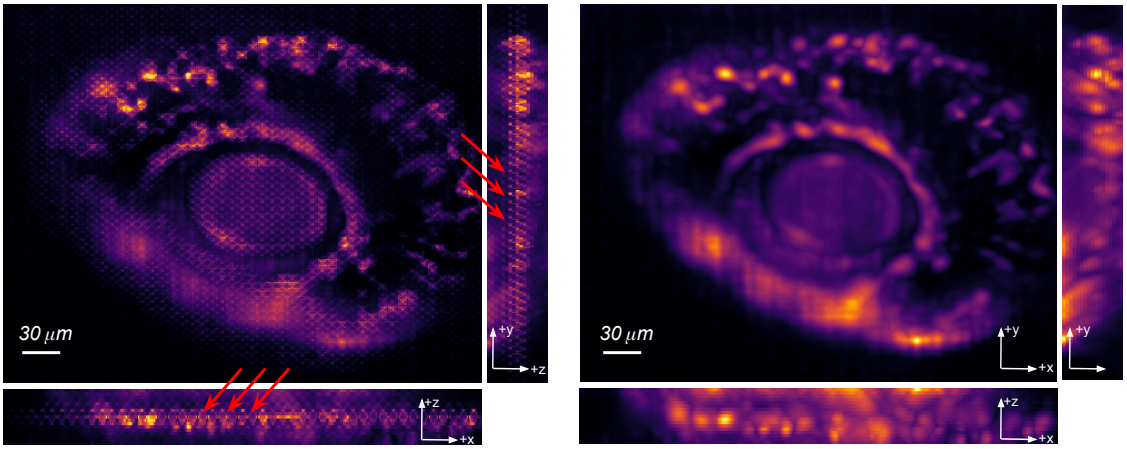

(a) Baseline LF deconvolution [67] (b) Aliasing-aware deconvolution

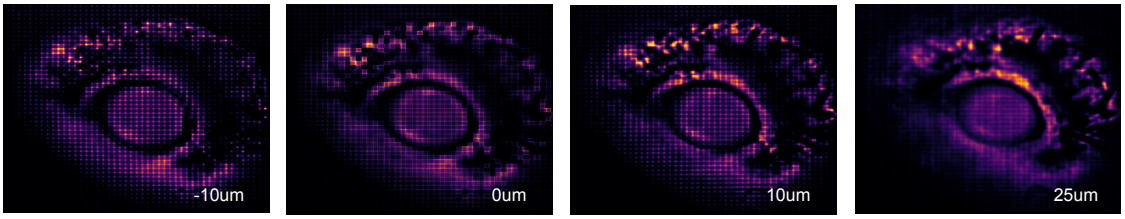

(c) Baseline LF deconvolution [67]

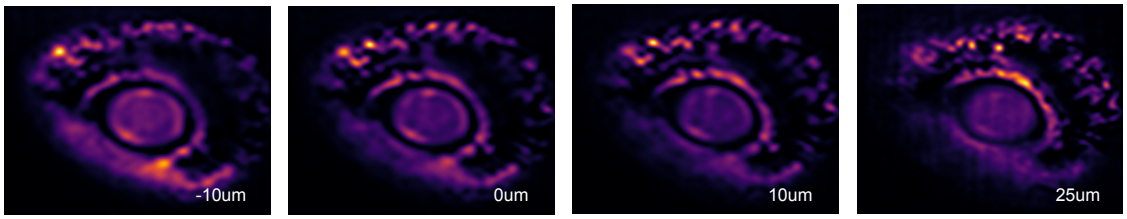

(d) Aliasing-aware deconvolution

Figure 3.9: 3D reconstruction of a zebrafish eye over an axial range $\Delta z = [-50, 50]\mu m$. *(a), (b)*: maximum intensity projections. *(c), (d)*: lateral slices through the volume. The reconstruction with the baseline method in [67] shows strong specific aliasing artifacts (red arrows) at depth planes close to the *zero plane*, while they fade out as we move further away from this plane. In comparison, our aliasing-aware deconvolution scheme completely removes all the artifacts.

the sampling requirements of the LFM. Both reconstructions (Fig. 3.9) were obtained after 8 iterations of the corresponding update schemes.

Fig. 3.10 shows a reconstructed cardiomyocyte organoid labelled with the calcium dye Fluo4-AM. Such organoids are an emerging platform for clinical trials, enabling high-throughput studies (both logistically and ethically since they are not organisms), along with possible direct clinical applicability, since they are derived from human stems cells. Contrary to traditional cell-cultures they are extended across all three dimensions and they have interesting temporal dynamics like cell-signaling and, specifically for heart-organoids, movements.

For the reference method [67], reconstruction artifacts are again strongly present (Figs. 3.10(a) and 3.10(c)) around $\Delta z = 0\mu m$, while gradually fading out further away; see the slice at $\Delta z = 50\mu m$. In the corrupted regions, a subsequent data analysis is not only troublesome, but rather unreliable. In comparison, our proposed method, specifically treats these artifacts via our depth-dependent resampling strategy (Figs. 3.10(b) and 3.10(d)). Again 8 iterations were performed for both methods.

3.5.2 Defocused LFM design

In this section we evaluate the defocused LFM setup. For this purpose, we place the micro-lens array at a distance $d_{tl}^{mla} \neq f_{tl}$ from the tube lens, while keeping the tele-centricity as before (see Figs. 3.5(b) and 3.5(c)). The d_{mla}^{sens} distance will then follow from eq. (3.17) to ensure the micro-images optimally cover the sensor plane.

Fig. 3.11 shows the reconstruction of a zebrafish eye (a different sample from the one in Fig. 3.9), over an axial range $\Delta z = [-40, 40]\mu m$, from LF images acquired when $d_{tl}^{mla} > f_{tl}$ and $d_{tl}^{mla} < f_{tl}$. In order to perform deconvolution on these images, we used the LFPSF we derived in Section 3.3 to describe the forward imaging model. In Fig. 3.11(b) we show the reconstruction using the classic Richardson-Lucy scheme, as in eq. (3.25). While in the original LFM configuration the reconstructed samples show prominent aliasing artifacts around $\Delta z = 0\mu m$ due to the coarse sampling in this region, here, in the defocused LFM design we observe the artifacts pushed to the edges of our axial range. This effect is due to the displacement of the MLA from the native image plane, Δ_{MLA}, which effectively translates into a proportional axial shift of the depth dependent lateral sampling rates in the object space by Δ_{NOP}, see eq. (3.8). This means an axial range Δz in front of a defocused LFM setup is sampled in the same way the Δz_{FOP} range would be sampled by the original LFM setup with the same settings.

Table 3.1 contains the system parameters for the used experimental data sets, together with the relevant reconstruction settings. The *Fish eye(>)* and *Fish eye(<)* entries correspond to the $d_{tl}^{mla} > f_{tl}$ and $d_{tl}^{mla} > f_{tl}$ configurations in Fig. 3.11, respectively. Reconstructing the $[-40, 40]\mu m$ axial range in both situations is equivalent, in terms of recoverable resolution, to reconstructing the $[-80, 0]\mu m$ and $[5, 85]\mu m$ in the original LFM setup (see Δz_{FOP} column); effectively shifting the *zero plane* by Δ_{NOP}. This explains the strongest artifacts in Fig. 3.11(b) being at the right most end of the axial range ($\Delta z_{FOP} = [-80, 0]\mu m$) when $d_{tl}^{mla} > f_{tl}$, and at the left most end of the axial range ($\Delta z_{FOP} = [5, 85]\mu m$) for the $d_{tl}^{mla} < f_{tl}$ case. In Fig. 3.11(c) we show the artifact-free deconvolution obtained using our Estimate-Maximize-Smooth scheme, and in Fig. 3.11(d) we illustrate z-slices of the reconstructed volumes every

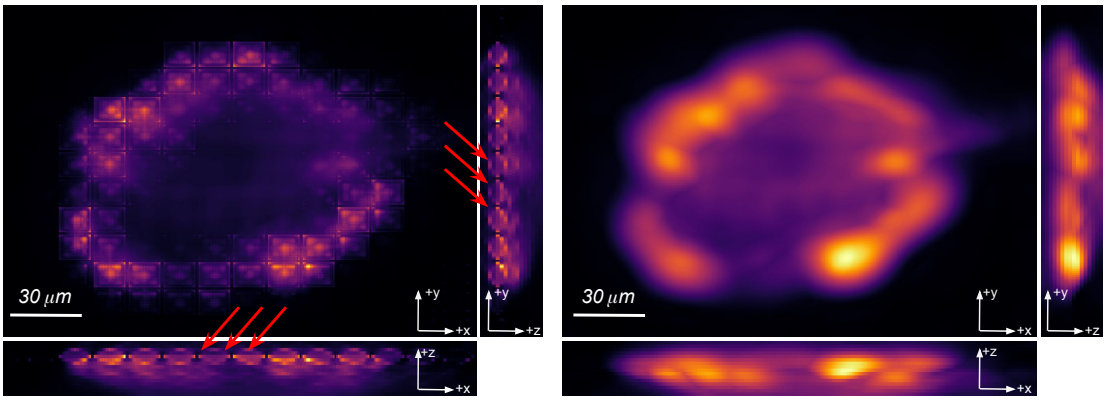

(a) Baseline LF deconvolution [67] (b) Aliasing-aware deconvolution

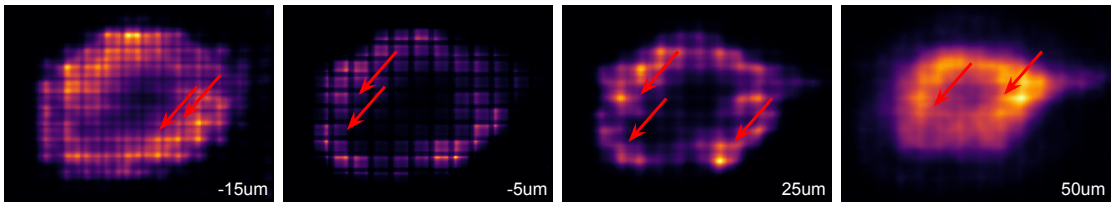

(c) Baseline LF deconvolution [67]

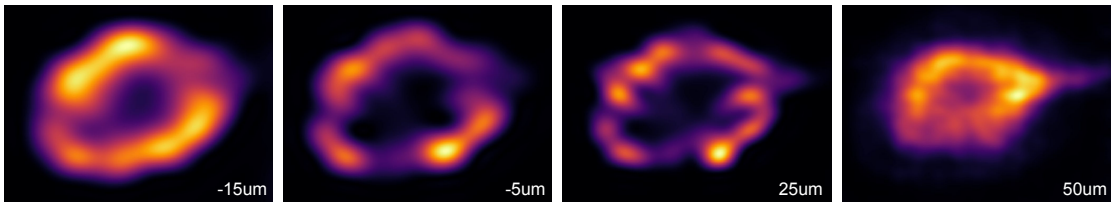

(d) Aliasing-aware deconvolution

Figure 3.10: **3D reconstruction of a cardiomyocyte organoid over an axial range** $\Delta z = [0, 50]\mu m$**.** *(a), (b)*: maximum intensity projections. *(c), (d)*: lateral slices through the volume. The reconstruction with the baseline method in [67] shows strong specific aliasing artifacts (red arrows) at depth planes close to the *zero plane*, while as we move away from this plane, the artifacts are less visible. Our aliasing-aware deconvolution method shows superior artifact-free results.

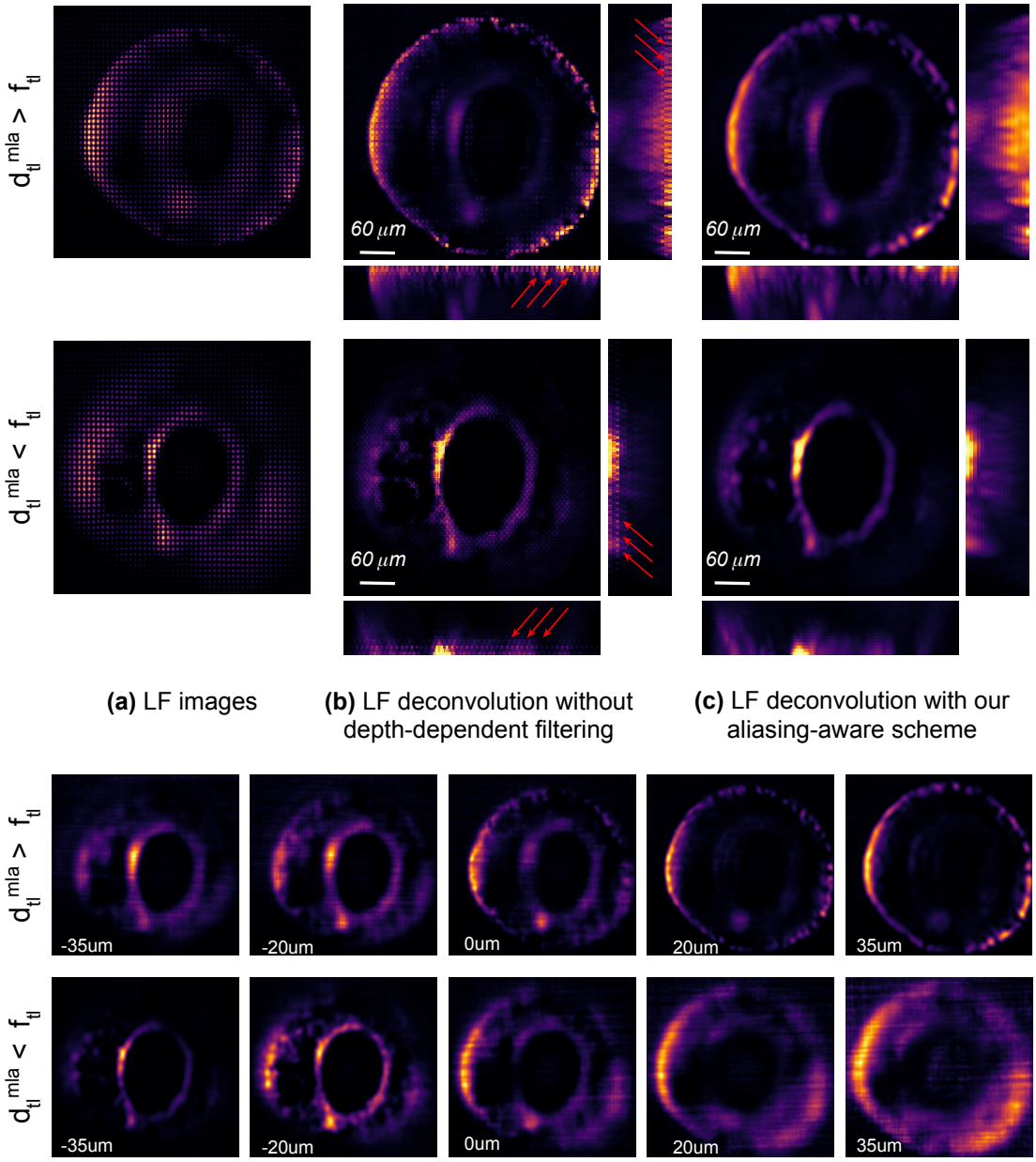

Figure 3.11: Defocused LFM: 3D reconstruction of a zebrafish eye over an axial range $\Delta z = [-40, 40]\mu m$. **(a) LF images** acquired when $d_{tl}^{mla} > f_{tl}$ and $d_{tl}^{mla} < f_{tl}$. **(b) The reconstruction using the Richardson-Lucy scheme** shows artifacts around the FOP plane of each setup. The defocused LFM is effectively an axially shifted (by Δ_{NOP}; see Table 3.1) version of the original LFM; the *zero plane* behavior is now appearing at the FOP plane. **(c) The artifact-free reconstruction** using our aliasing-aware deconvolution method. **(d) Lateral slices through the reconstructed volume.** The two defocused LFM configurations demonstrate higher resolved features at complementary axial ranges; marked with smileys.

$5\mu m$. We perceive better spatially resolved features in the range $[0, 40]\mu m$ for the $d_{tl}^{mla} > f_{tl}$ setup, while in the $d_{tl}^{mla} < f_{tl}$ case this range appears blurred and the $[-40, 0]\mu m$ range is resolved better.

Data set	f_{tl}	d_{tl}^{mla} (mm)	d_{mla}^{sens} (mm)	Δz (μm)	Δ_{NOP} (μm)	$\Delta z_{FOP} = \Delta z + \Delta_{NOP}$ (μm)
USAF	165	165	3.0	0	0	0
Fish eye	165	165	3.0	$[-50, 50]$	0	$[-50, 50]$
Organoid	165	165	3.0	$[0, 50]$	0	$[0, 50]$
Fish eye (>)	165	181	2.985	$[-40, 40]$	-40	$[-80, 0]$
Fish eye (<)	165	147	3.016	$[-40, 40]$	45	$[5, 85]$
Spheres (>)	165	175	2.990	$[-45, 45]$	-25	$[-70, 20]$
Spheres (=)	165	165	3.0	$[-45, 45]$	0	$[-45, 45]$
Spheres (<)	165	151	3.012	$[-45, 45]$	35	$[-10, 80]$

Table 3.1: Data set acquisition parameters of our experimental LFM setup together with the corresponding reconstructed axial ranges. **Top three rows:** Datasets acquired with the focused LFM setup. **Bottom five rows:** Datasets acquired with various defocused LFM configurations.

In Fig. 3.12, we imaged $1\mu m$ fluorescent beads in agarose with the LFM in the three configurations depicted in Fig. 3.5. Fig. 3.12(a) (top) shows the acquired LF image for the original plenoptic design ($d_{tl}^{mla} = f_{tl}$), together with the 3D reconstruction using our proposed method in Fig. 3.12(b) (top). Fig. 3.12(a) (middle) and (bottom) illustrate the acquired LF image for the defocused design with $d_{tl}^{mla} > f_{tl}$ and $d_{tl}^{mla} < f_{tl}$, respectively, alongside the 3D reconstructions in Fig. 3.12(b) (middle) and (bottom). The red rectangle highlights two micro-spheres at the *zero plane* of the LFM ($\Delta z = 0$). While, in the original LFM setup (top) they are only reconstructed at the lenslet resolution, in Fig. 3.12 (middle) and (bottom) they appear better resolved. On the other side, the dashed arrow, for example, points to a sphere placed at the FOP plane in the defocused $d_{tl}^{mla} > f_{tl}$ (middle) case. While in this case it can only be recovered at lenslet resolution, in Fig. 3.12 (top) and (bottom) we observe it at higher resolution. Analogous discussion applies to the other beads. Just as we have seen for the fish eye in Fig. 3.11, while one LFM configuration performs well at spatially resolving certain depths in the axial range, it does so at the cost of other depths, which is also the case when imaging away from the *zero plane* with the original LFM. In order to extend the resolvable range in the 3-D reconstructions, such LFM configurations can be complementary, which supports and motivates the work towards multi-focus [55, 112] or dual-camera [45, 113] plenoptic setups.

3.6 Discussion

In this Chapter we address one of the challenges in 3D reconstruction of light field microscopy data, the aliasing artifacts. We perform an analysis of the aliasing-free sampling requirements of the LFM to derive depth-dependent anti-aliasing filters. We also derive a generalized wave-based LFPSF to propose a novel aliasing-aware deconvolution scheme that applies to arbitrary LFM designs. We compare the capabilities of the original and defocused LFM designs in terms of recoverable lateral resolution at various axial ranges and demonstrate the superior quality reconstruction performance of our method using experimental data from phantoms and in-vivo biological samples.

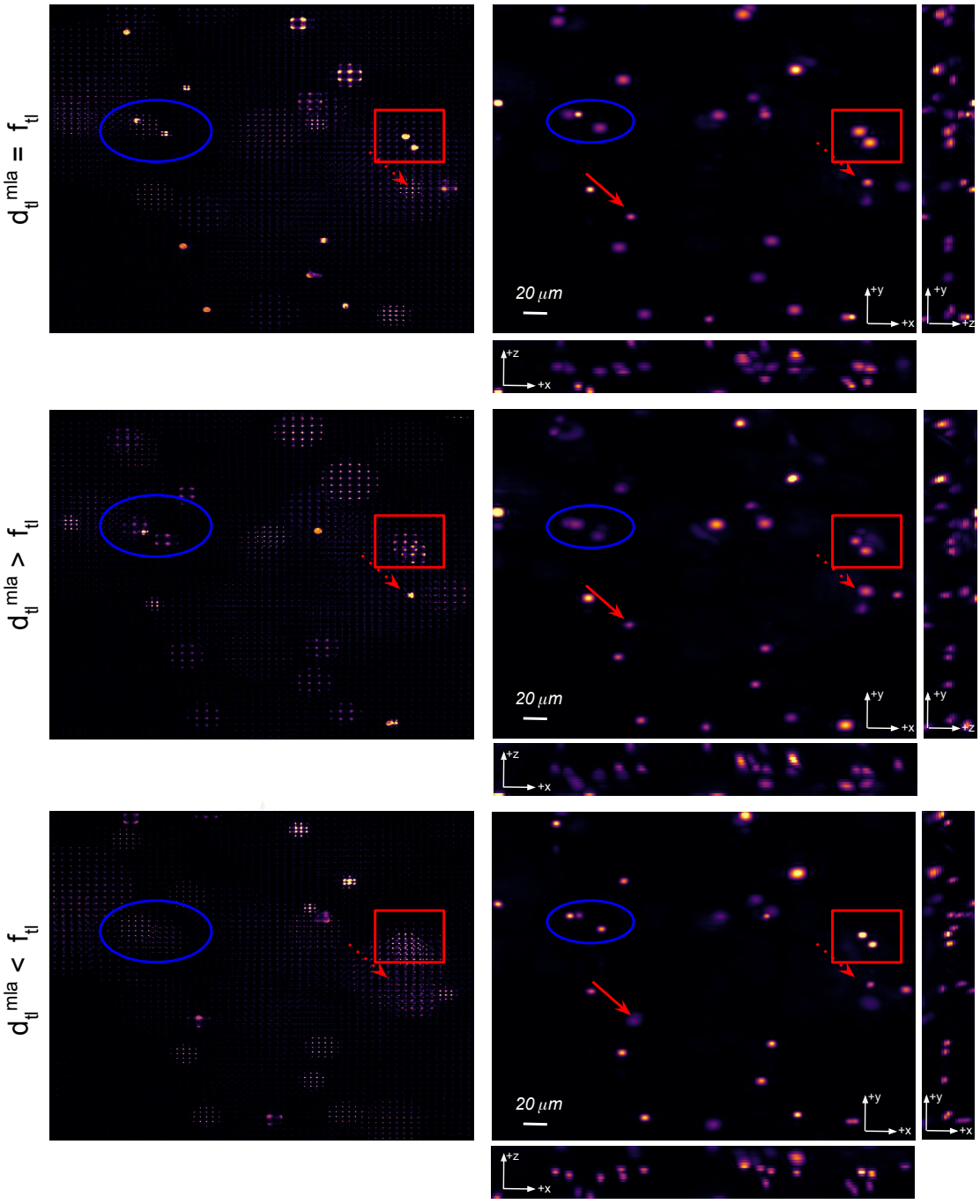

Figure 3.12: **Defocused LFM:** 3D reconstruction of fluorescent beads in agarose over an axial range of $\Delta z = [-45, 45]\mu m$. **(a) Acquired LF images. (b) The reconstructed volumes** using our method for the original plenoptic design with $d_{tl}^{mla} = f_{tl}$ (top) and the defocused LFM with $d_{tl}^{mla} > f_{tl}$ (middle) and $d_{tl}^{mla} < f_{tl}$ (bottom). The red and blue highlights suggest how different features at different depths are better resolved in one configuration than in the others. No plenoptic design is generally better or worse.

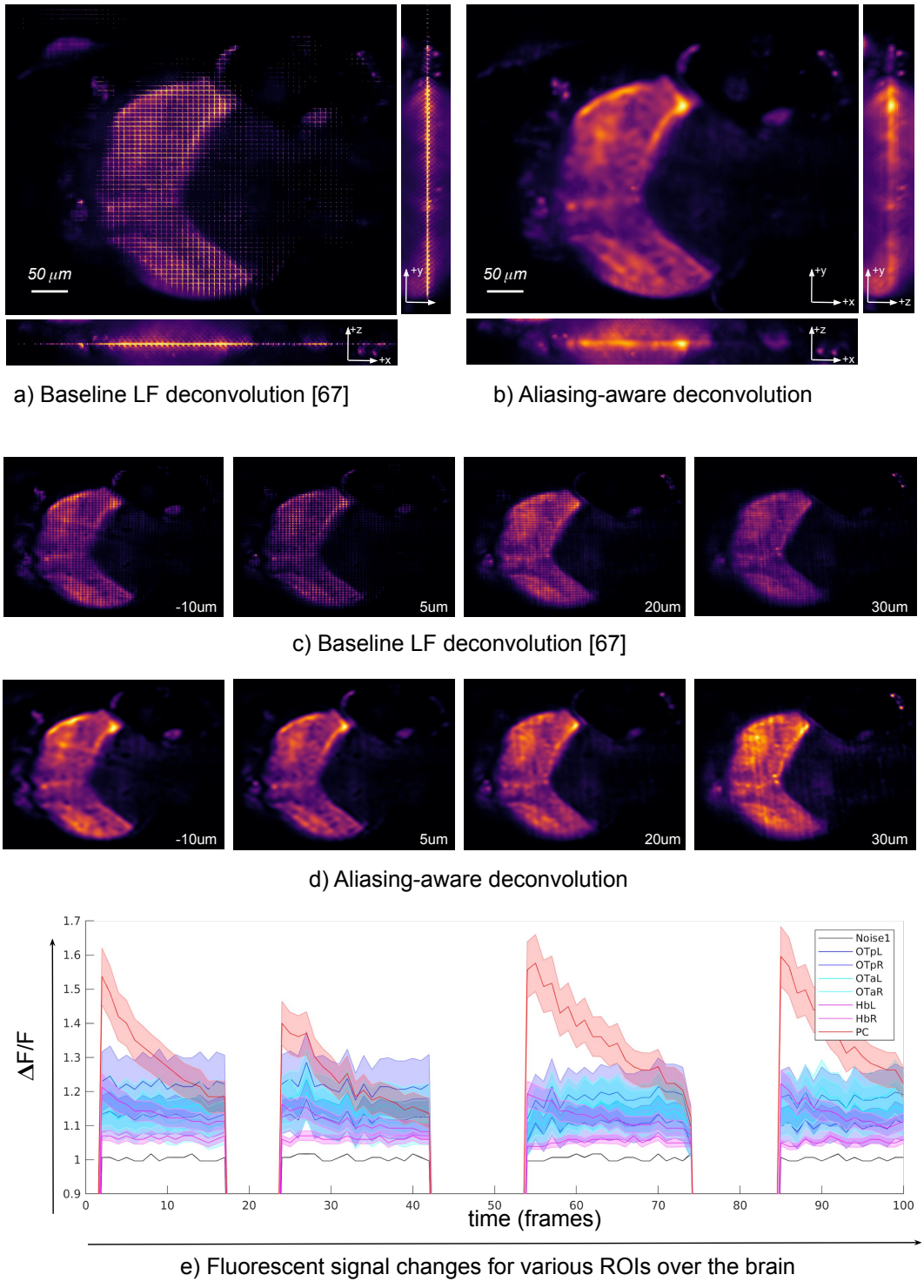

Figure 3.13: 3D reconstruction of a zebrafish larvae brain over the axial range $\Delta z = [-80, 70]\mu m$. *Top*: maximum intensity projections. *Bottom*: lateral slices through the volume. The reconstruction with the baseline method in [67] shows strong specific aliasing artifacts (a) and c)) at depth planes close to the *zero plane*, while as we move away from this plane, the artifacts are less visible. Our aliasing-aware deconvolution method shows superior artifact-free results (b) and d)). **e):** Fluorescent signal changes for various biologically significant ROIs over the fish brain.

Our work and [57] share the anti-aliasing priors idea in an interesting way. In [57], the authors use light field projections of the filtering kernels directly on the micro-images to ensure correct, non-aliased disparity maps. They then incorporate the estimated disparity in the light propagation model and proceed to recover the 2D radiance (all-in-focus image) from a light field camera image employing a variational Bayesian framework. This can be interpreted as an implicit accounting for the aliasing through the disparity prior. In our work, on the contrary, we derive the anti-aliasing filter kernels in the object space and explicitly apply them to the light field as a correction step of our iterative aliasing-aware deconvolution, which employs a smoothing expectation maximization scheme.

The analysis and the deconvolution scheme we propose apply to arbitrary plenoptic configurations. Hence, we also derive a generalized wave-based forward light propagation model able to characterize both original (plenoptic 1.0) [58, 67] and "focused" (plenoptic 2.0) LFM setups.

In previous works, the "focused plenoptic" (or plenoptic 2.0) camera [54, 56] design was proposed to enhance the spatial resolution of the captured light field, compared to the original plenoptic camera [62], by manipulating the placement of the sensor with respect to the MLA such that the micro-lenses are focused on the objective lens. When coming to the light field microscope, due to the presence of the tube lens, manipulating the distance between the MLA and the camera sensor immediately affects the distance between the tube lens and the MLA such that the conjugate image of the native object plane may be in front or behind the MLA, creating a defocused field incident on the MLA, as opposed to the original LFM case, where the native image pane coincides with the MLA plane. Thus, although conflicting with the established "focused plenoptic" term, we find the term "defocused LFM" to better reflect generic LFM designs, as the recoverable resolution at a certain depth in the object space strongly depends on the extent of the defocus generated at the MLA plane.

Although we improve the visual appearance of the 3D reconstructed objects by addressing the sampling artifacts, the effective lateral resolution is still limited by the depth-dependent sampling rate.

We showed that defocused LFM designs better resolve the near native object plane range, while sacrificing resolution at other depth ranges by axially shifting the sampling patterns; similar to imaging away from the *zero plane* with the original LFM design. This situation can be improved by splitting the optical path and imaging with complementary focused LF systems [45, 113], or combining a light field with a wide-field acquisition [73]. Alternatively, employing an array of lenslets with mixed focal lengths introduces more irregularity in the sampling patterns and allows increased depth of field [55, 112]. In [105], denser and more uniform sampling through lens aberrations was discussed, while [72] demonstrates higher lateral resolutions over extended depth of field by introducing phase masks in the optical path of the LFM.

Chapter 4

Fourier light field microscopy

The work in this chapter was published in:

- A. Stefanoiu, G. Scrofani, G. Saavedra, M. Martínez-Corral, and T. Lasser. "What about computational super-resolution in fluorescence Fourier light field microscopy?" *Optics Express*, 28, p. 16554, 2020. DOI: 10.1364/OE.391189.

- A. Stefanoiu, G. Scrofani, G. Saavedra, M. Martínez-Corral, and T. Lasser. "Deconvolution in Fourier integral microscopy." *Proc. SPIE 11396, Computational Imaging V*, p. 18, 2020. DOI: 10.1117/12.2558516.

4.1 The Fourier integral microscope

Fourier integral microscopy (FiMic) was recently introduced [59] to address the current challenges in conventional LFM.

A Fourier integral microscope (FiMic) is built by inserting a micro-lens array (MLA) at the back aperture stop (AS) of a conventional microscope objective (MO) and recording far-field (Fourier) perspective views (elemental images) of the object under each micro-lens [71]. While compact in design, this arrangement provides extended depth of field and improved uniform lateral resolution compared to conventional LFM [71].

Fig. 4.1 illustrates a ray diagram of the light propagation through a FiMic. Since the AS is usually not accessible for commercial microscope objectives, the configuration depicted here employs a telecentric optical relay system (RL1 and RL2, with focal lengths f_1 and f_2, respectively) to conjugate the AS plane and the MLA plane. Note that, when $f_1 \neq f_2$, there is a relay magnification factor $M_{relay} = \frac{f_2}{f_1}$ that contributes to the total system magnification. For an arbitrary source point in front of the objective, $\mathbf{o}(o_x, o_y, z)$, we will represent the axial coordinate as $z = f_{obj} + \Delta z$, since an object at the front focal plane (the native object plane, NOP) is in focus in a conventional wide-field microscope. f_{obj} is the focal length of the objective lens.

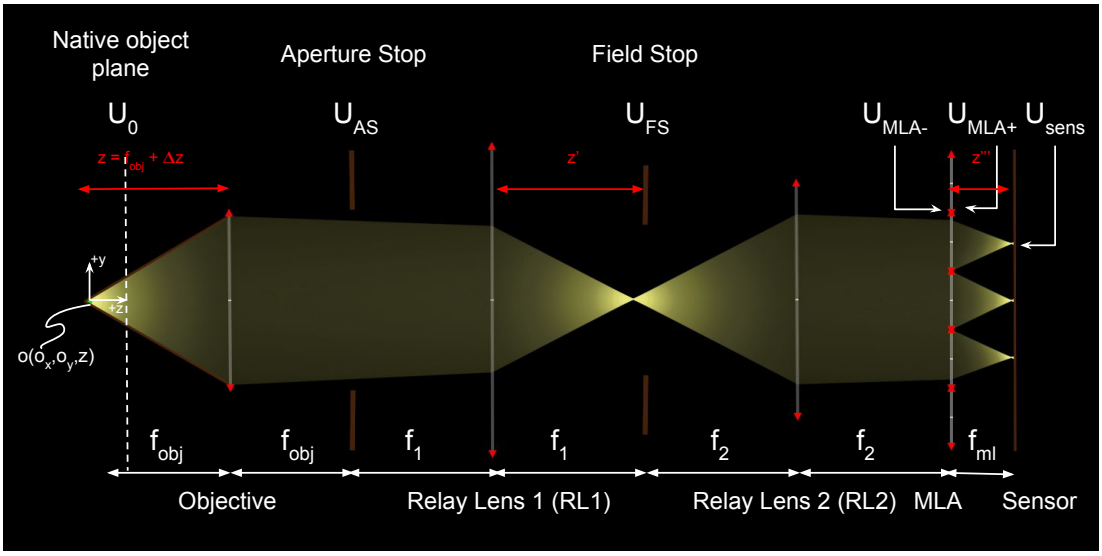

Figure 4.1: Ray diagram: light field propagation through the Fourier integral microscope. The FiMic depicted here makes use of an optical relay system (RL1 and RL2 with focal lengths f_1 and f_2, respectively) which conjugate the back aperture of the microscope objective (MO) with the MLA plane. The reason for the relay is that the back aperture is usually not accessible in conventional commercial MOs. A source point $\mathbf{o}(o_x, o_y, z = f_{obj} + \Delta z)$ in front of the MO has a conjugate image by the first relay lens (RL1) at z'. RL2 picks up this image and magnified images are recorded behind each micro-lens as the light reaches the camera sensor. f_{obj} denotes the MO focal length and Δz represents the axial offset from the native object plane.

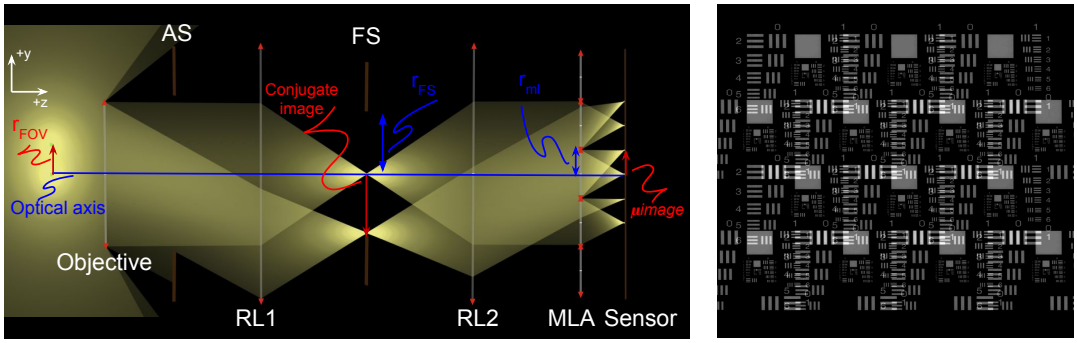

a) Field Stop requirement for optimal sensor coverage

b) Overlapping elemental images (EIs)

Figure 4.2: Image formation in FLFM. (a) The field stop (FS) controls the size of the elemental images (EIs) as well as the size of the microscope's field of view. See Eq. (4.1) and Eq. (4.2). (b) Overlapping images of the USAF resolution target when the FS is too large.

Then Δz is an offset from the NOP, and we will refer to it when talking about depth in the subsequent sections.

A source point at a depth z in front of the MO has a conjugate image at z' by the first relay lens, RL1. This intermediate image is then picked up by the second relay lens, RL2, and finally, magnified images of the field stop (FS) are recorded behind each micro-lens as the light reaches the camera sensor. The FS, as depicted in Fig. 4.2(a), controls the lateral extent of the micro-images as $\mu_{image} = r_{FS}\frac{f_{ml}}{f_2}$. Here r_{FS} is the radius of the FS, f_{ml} is the focal length of the micro-lens and μ_{image} is the radius of the EI formed on the sensor. In order for the EIs to optimally cover the sensor plane (without leaving space between them or overlapping), the micro-image radius must match the micro-lens radius, $\mu_{image} = r_{ml}$. Then the radius of the FS satisfies:

$$r_{FS} = r_{ml} \cdot f_2 / f_{ml}. \tag{4.1}$$

It quickly follows, as depicted in Fig. 4.2(a), that the FS determines the field of view (FOV) of the FiMic, as its radius satisfies:

$$r_{FOV} = r_{FS} \cdot f_{obj} / f_1. \tag{4.2}$$

Figure 4.2(b) shows a simulated light field image of the USAF 1951 resolution target with overlapping EIs when the FS does not satisfy Eq. (4.1).

4.2 Aliasing and computational super-resolution

By design, behind the micro-lenses, the FiMic records EIs with dense spatial sampling and each with different angular content. The number of micro-lenses that can be fitted within the AS

is $N = M_{relay}\frac{r_{obj}}{r_{ml}}$, with r_{obj} being the radius of the AS. Then such a setup captures N angular views of the imaged scene. With an equivalent (in terms of MO) wide-field microscope, these EIs could be captured if pinholes would be placed at certain positions over the AS. Hence, the recorded light field consists of pinhole views at N locations over the numerical aperture of the objective, NA_{obj}. The number of micro-lenses controls the spatio-angular resolution trade-off. By increasing N we may capture more views, however, at a lower spatial resolution as the effective numerical aperture is reduced proportionally, $\frac{NA_{obj}}{N}$ [71].

When aiming at 3D reconstruction of the imaged object, the resolution of the volumetric reconstruction is directly determined by the band limit of the recorded signal in each perspective view. Thus, high-frequency details in the volume can only be recovered if they can be resolved in the views. Under the Rayleigh resolution criterion for diffraction limited systems [108], two source points are resolved in each of the EIs, when they are separated by at least a distance:

$$\delta_{diff} = N\frac{\lambda}{2NA_{obj}}, \tag{4.3}$$

where λ is the wavelength of the light we employ.

On the other hand, the sampling rate in an EI is crucial in determining how high frequencies of the light field signal are recorded on the sensor. Within each EI, the sampling period in the object space is given by the camera pixel pitch, ρ_{px} divided by the total system magnification factor, $M_{FiMic} = \frac{f_{ml}f_1}{f_2 f_{obj}}$. Then, using Nyquist's criterion, we define the sensor resolution as:

$$\delta_{sensor} = 2\frac{\rho_{px}}{M_{FiMic}}. \tag{4.4}$$

When δ_{sensor} samples the signal below the band limit, high frequency details of the light field appear aliased as low frequency features in the individual EIs. One could potentially try to alleviate the under-sampling issues by proper selection of the relay magnification. However, this is not a good strategy since such an increase of the magnification involves the reduction of the FOV and the need of high-NA micro-lenses which have poor optical quality [71].

A feature that inherently characterizes the orthographic images captured in FLFM, when working with fluorescent samples, is the under-sampling of the PSF. This happens due to the sensitivity and noise requirements of the camera sensors, which are often met by the use of large pixels. Note that this problem does not occur in conventional fluorescence microscopy due to the large magnification factor between the object and the sensor planes.

We introduce the super-sampling factor $s \in \mathbb{Z}$ to characterize the object space sampling rate of our reconstructed volumes. If we sample the volume at a rate s times the sensor resolution, the lateral voxel spacing is:

$$\delta_{super} = \frac{\delta_{sensor}}{s}. \tag{4.5}$$

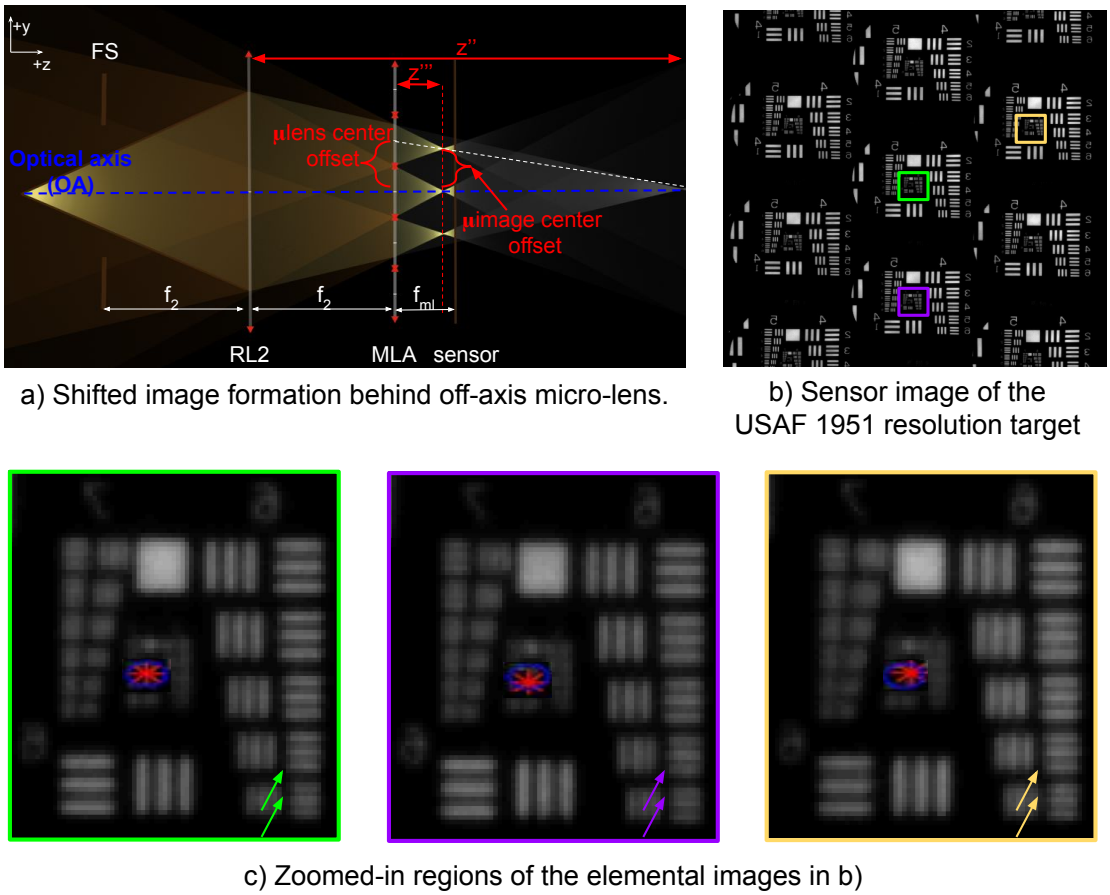

a) Shifted image formation behind off-axis micro-lens.

b) Sensor image of the USAF 1951 resolution target

c) Zoomed-in regions of the elemental images in b)

Figure 4.3: Aliasing and EI sampling rates. a) The EIs formed behind off-axis micro-lenses are shifted with respect to the centers of the micro-lenses. b) FiMic image of the USAF 1951 resolution target placed at $\Delta z = -100\mu m$. c) Zoomed-in regions of the EIs in b) showing distinct aliasing patterns in areas with high frequency features as highlighted by the arrows. The micro-lens centers (red dots) and the EI centers (dark blue dots) are mismatched for the off-axis EIs.

There are various works in computer vision demonstrating computational super-resolution through combining multiple aliased low-resolution images acquired at sub-pixel camera movements [74, 114–118]. In light field photography and conventional light field microscopy, computational super-resolution was addressed by exploiting sub-lenslet sampling [57, 67, 68, 77–79].

In Fourier light field microscopy, the EIs form behind the micro-lenses at specific translational offsets with respect to their corresponding micro-lens centers. In Fig. 4.3(a) a ray diagram of the image formation of a point source away from the NOP is depicted. The first part of the light propagation is omitted for the sake of clarity of the figure. The center of the image (μ_{image}) formed behind an off-axis micro-lens, with respect to the optical axis (OA) of the system, is translationally offset from the corresponding micro-lens (μ_{lens}) center. We will refer to the EI behind the micro-lens centered on the OA as the *reference EI*, since this image is aligned with the micro-lens. Then the translational offsets specific to the off-axis EIs are stated with respect to this image. Fig. 4.3(b) shows an image acquired with our experimental FiMic of the USAF-1951 resolution target placed at $\Delta z = -100\mu m$ in front of the MO. And Fig. 4.3(c)

shows zoomed-in regions of three arbitrarily picked EIs of the image in Fig. 4.3(b). The centers of the micro-lenses are marked in red on the image, while the centers of the EIs are marked in blue to highlight the misalignment between them. These images contain distinct complementary aliasing patterns (especially noticeable for elements 6.4 and 6.5 of the USAF target) which motivate computational super-resolution. Figure 4.4(a) illustrates how the shift patterns change with object depth and Fig. 4.4(b) visualizes these shifts in pixels (between each micro-lens and its corresponding EI) for an axial range [-120, 120]μm to give an intuitive understanding on how the image formation in FLFM varies with object depth. The μ_{lens} *index* being zero refers to the reference (central) micro-lens, which is the closest to the OA.

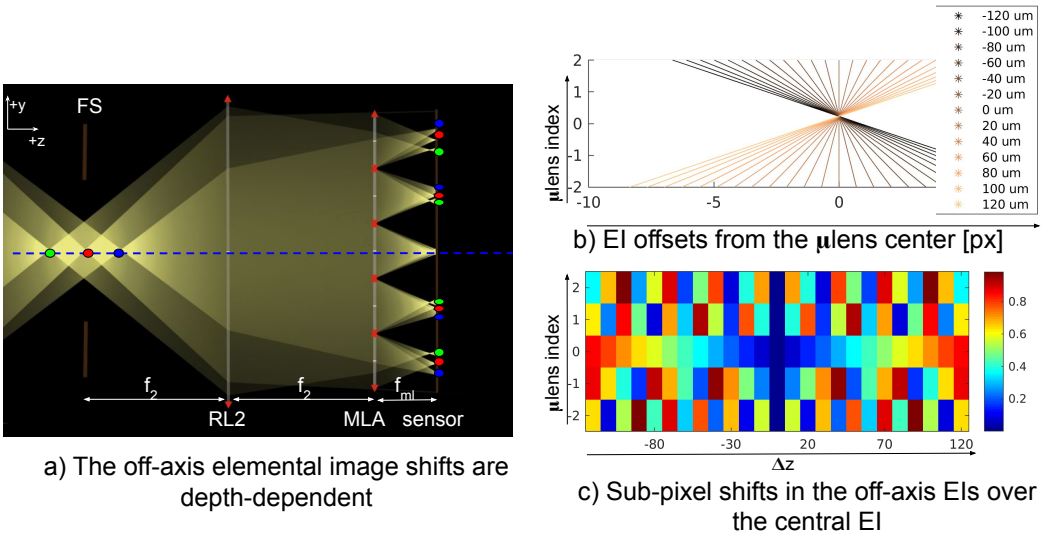

Figure 4.4: Depth-dependent lateral shift for the EIs. a) The EIs exhibit different shift pattern with object depth. b) EIs offsets in pixels from the micro-lens centers with respect to a reference EI (closest to the optical axis) for objects placed at Δz = [-120, 120] μm. The μ_{lens} *index* = 0 refers to the central micro-lens (closest to the OA). c) Sub-pixel shifts of the EIs with respect to the reference EI over depth. It is these sub-pixel shifts between the captured views that record complementary aliased information and motivate computational super-resolution.

More interesting for our discussion are the sub-pixel shifts which are the fractional part of the pixel shifts in Fig. 4.4(b). Fig. 4.4(c) displays the absolute value of the sub-pixel shifts as a function of axial position of the source point and μ_{lens} *index* and they appear highly irregular, although consistent in density across depth. The lack of symmetry with respect to the 'μ_{lens} index' axis is due to the fact that the reference EI is not perfectly aligned with the optical axis, but rather the most central one, as it is not trivial to perfectly align the MLA with the optical axis in practice. However, this misalignment does not impact our reasoning, as long as the location of the sub-imaging systems (micro-lenses) can be determined. When computing the system's response for a specific arrangement, we first detect the relative positions (with respect to the reference EI) of the centers of the micro-lenses. Also, at the *zero* plane ($\Delta z = 0 \mu m$) the off-axis EIs show no shift in Fig. 4.4(c). However, the concept of NOP in experimental FLFM is rather mathematical than physical as any small displacement from that plane gives rise to a collection of EIs with subpixel shifts. When we present the results we show that super-resolution is achievable also around the NOP.

In order to recover high-frequency features, enough images with distinct aliasing patterns

should be combined, such that the sub-pixels shifts constitute a sufficiently dense sampling pattern [106, 119–121]. Such requirements contribute to the ultimate fundamental resolution limits of the deconvolved image, the band limit through diffraction limit, the camera pixel size, sensitivity, fill factor and prior scene information [122]. Multiple such aliased images of a scene can be computationally combined to enhance the resolution of the recontructed volume, provided known sub-pixel translational offsets between them Provided sufficient aliased EIs, we aim at fusing this complementary information while also removing out of focus light in order to recover a high resolution 3D reconstruction through deconvolution. When the sensor pixels are close to or smaller than the diffraction limit (generally the case in microscopy), the aliasing is probably neglectable and computational super-resolution is of relatively low impact. We will discuss these aspects when we present our results in section 4.4.

4.3 3D reconstruction

4.3.1 The light field point spread function model

In order to obtain a 3D reconstruction of the imaged sample, we aim at characterizing the point spread function (PSF) of the system and use it to perform deconvolution. In this section we introduce a wave-based forward light propagation model to describe the optical system's PSF. For that we derive the diffraction pattern of a source point when the light propagates through the FiMic from the source to the camera sensor and we discuss the wavefront at intermediate key planes in the following subsections.

A source point $\mathbf{o}(0, 0, o_z = f_{obj} + \Delta z_o)$ in front of the microscope generates, according to Rayleigh-Sommerfeld theory [81], a wavefront distribution at the front focal plane of the objective:

$$U_0(x, y; \mathbf{o}) = \frac{A}{r} e^{ikr(sign(\Delta z_o))}, \tag{4.6}$$

where A is the amplitude of the source electrical field, $r = \sqrt{x^2 + y^2 + \Delta z_o^2}$ is the distance between the source point and the observation point (x, y) at the front focal plane, $k = \frac{2\pi}{\lambda}$ is the wave number and λ is the wavelength of the assumed monochromatic light.

According to Debye scalar integral representation, the wavefront distribution at the back focal plane of the objective is given by[123]:

$$U_{AS}(r_{as}; \mathbf{o}) = \int_0^{\alpha} U_0(\theta; \mathbf{o}) J_0(k r_{as} \sin(\theta)) \sin(\theta)\, d\theta, \tag{4.7}$$

where $r_{as} = (x_{as}, y_{as})$ stands for the lateral coordinate at the AS, α is the aperture angle so that $NA_{obj} = \sin(\alpha)$, and $\theta = \sin^{-1}(r_{as}/f_{obj})$. J_0 represents the zeroth order Bessel function of the first kind. From this equation we recognize a Fourier-Bessel transformation between the amplitude at the front and the back focal planes.

The wave propagation between the AS and the MLA can be accurately described under the Fresnel approximation, Thus, the wavefront incident on the MLA array is the magnified version of the wavefront at the MO aperture stop:

$$U_{MLA-}(x_{mla}, y_{mla}; \mathbf{o}) = U_{AS}\left(\frac{x_{mla}}{M_{relay}}, \frac{y_{mla}}{M_{relay}}; \mathbf{o}\right), \tag{4.8}$$

where $M_{relay} = \frac{f_2}{f_1}$. As pointed out in Sec. 4.1, for practical design reasons, the FiMic makes use of a relay system, depicted by the RL1 and RL2 lens in Fig. 4.2(a), in order to mimic the MLA being placed at the AS plane (Fourier plane) of the objective. There is no need to explicitly model the relay system, however we have to account for the induced magnification factor, M_{relay}. When $f_1 = f_2$, the relay is 1:1 and the wavefront distributions U_{MLA-} and U_{AS} are the same.

In [124], the authors have very recently presented a similar wave-based model for describing the incident field on the MLA. They directly compute the wavefront at the intermediate image plane (in our naming scenario this is at the back focal plane of RL1) using the Debye integral derivation for 4f systems [81] and then Fourier transform this field to obtain the distribution at the MLA. This brings an unnecessary computational overhead and a degree of inflexibility as the model confines the FiMic design to configurations containing the relay lenses, which as we have discussed above, do not need explicit modeling. The relay system in our experimental setup is an auxiliary construction due to the AS not being physically accessible in commercial MOs, and not an essential specification of the FiMic.

In the next step, the wavefront is further transmitted by the MLA. The field U_{MLA+} immediately after the MLA is given by:

$$U_{MLA+}(x_{mla}, y_{mla}; \mathbf{o}) = U_{MLA-}(x_{mla}, y_{mla}; \mathbf{o}) \cdot T(x_{mla}, y_{mla}). \tag{4.9}$$

Here T is the MLA transmittance function modeled by replicating the single lenslet transmittance in a tiled fashion, $T = rep_{p_{ml}, p_{ml}}\big(t(x_l, y_l)\big)$; with $rep_{p_{ml}, p_{ml}}$ being the 2D replication operator and p_{ml} the spacing between micro-lenses. $t(x_l, y_l) = P(x_l, y_l)e^{\frac{ik(x_l^2+y_l^2)}{2f_{ml}}}$ is the complex transmittance function of a lenslet and (x_l, y_l) are the local lenslet coordinates, while $P(x_l, y_l)$ is the lenslet pupil function [67, 68].

Finally, similarly to [68], we employ the Rayleigh-Sommerfeld diffraction solution [108] to further propagate (for a f_{ml} distance) the light field to the sensor plane:

$$U_{sens}(x_s, y_s; \mathbf{o}) = \mathscr{F}^{-1}\Big\{\mathscr{F}\big\{U_{MLA+}(x_s, y_s; \mathbf{o})\big\} \cdot H_{rs}(f_X, f_Y)\Big\}, \tag{4.10}$$

where (x_s, y_s) are the coordinates at the sensor plane, $\mathscr{F}$ represents the Fourier transform operator, and (f_X, f_Y) are the spatial frequencies at the image plane. H_{rs} is the Rayleigh-Sommerfeld transfer function, given by:

$$H_{rs}(f_X, f_Y) = e^{\left(ik \cdot f_{ml}\sqrt{1-(\lambda f_X)^2-(\lambda f_Y)^2}\right)}. \tag{4.11}$$

The fact that we deal with an under-sampled process, in which the PSF is smaller than the pixel size, the small shape changes in the PSF due to the imperfections in the optical system have little relevance and therefore validate our decision of using the analytic LFPSF. Additionally, it must be taken into account that, since we are using well-corrected optical equipment (the MO and the achromatic lenses), our experiments are subjected to the same aberrations problems as conventional microscopes, and therefore we do not consider aberrations as a topic of special concern.

4.3.2 3D deconvolution

Given the raw noisy light field sensor measurements $\mathbf{m} = (m_j)_{j\in J}$ acquired by pixels $j \in J$ ($|J| = m$) we seek to recover the fluorescence intensity at each discrete point in the volume which produced these measurements. We represent the discretized volume $\mathbf{v}$ by a coefficient vector $(v_i)_{i\in I}$ with $|I| = n$. Note that the sampling rate in $\mathbf{v}$ is dictated by the super-sampling factor s defined in the previous section. Due to the low photon counts in fluorescence microscopy, the sensor pixels follow Poisson statistics, yielding the stochastic imaging model: $\mathbf{m} \sim \text{Poisson}(A\mathbf{v})$, where $\mathbf{m}$ denotes the light field measurement, $\mathbf{v}$ denotes the discretized volume we seek to reconstruct, and the operator $A = (a_{ji})_{j\in J, i\in I}$ describes the light field forward model, which is effectively determined by the FiMic point spread function in Eq. (4.10). For each point in a fluorescent object, the image intensity is given by the modulus squared of its amplitude [81]: $a_{ji} = \left|U_{sens}(\mathbf{x}_s(j), \mathbf{o}(i))\right|^2$, where $\mathbf{o}(i)$ is the object space coordinate of voxel i, and $\mathbf{x}_s(j)$ is the coordinate of sensor pixel j. We now employ the well known Richardson-Lucy algorithm [109, 125] to estimate $\mathbf{v}$. The iterative update in matrix-vector notation reads:

$$\mathbf{v}^{q+1} = \frac{\mathbf{v}^q}{A^T\mathbf{1}}\left[A^T\frac{\mathbf{m}}{A\mathbf{v}^q}\right], \tag{4.12}$$

where q is the iteration count. For a more detailed derivation of the reconstruction algorithm we refer the reader to the previous Chapter [68].

When we assume an aberration-free context, thanks to the strategic placement of the MLA at the at the back aperture stop of the MO, the light field PSF of the FiMic is translationally invariant for a fixed axial coordinate. Each micro-lens represents a sub-imaging system with spatially invariant PSFs and since all the micro-lenses are identical, the whole FiMic imaging system can be characterized by a shift invariant LFPSF, as a superposition of these individual PSFs [49]. Conveniently, this allows for the application of the columns of the matrix A for each depth Δz via a 2D convolution operation when implementing the iterative scheme in Eq. (4.12).

For practical reasons, when we discretize the object using the lateral spacing δ_{super} introduced in Eq. (4.5), we upsample the raw light field image by the super-sampling factor s. To make sure this step does not alter the measurements, we employ a nearest neighbor upsampling method.

4.3.2.1 Penalized likelihood

If we further assume that we have prior information about our solution, it is appropriate to estimate $\mathbf{u}$ by maximizing the penalized log-likelihood [126], $L(\mathbf{v}) - \lambda J(\mathbf{v})$ instead:

$$\arg\max_{\mathbf{u}} \sum_{j\in J}\sum_{i\in I} v_i a_{ji} + z_{ji} \ln x_i a_{ji} - \lambda J(\mathbf{v}), \tag{4.13}$$

where the prior $J(\mathbf{v})$ could, for example, represent a roughness functional and λ a smoothing parameter, as we will see in the next section.

To find a maximizer of the penalized likelihood, we adopt the explicit one step late (OSL) algorithm [126], and the iterative update scheme in Eq. 4.12 now becomes:

$$\mathbf{v}^{k+1} = \frac{\mathbf{v}^k}{A^T\mathbf{1} + \lambda * (\mathbf{D}J(\mathbf{v})_k)}\left[A^T\frac{\mathbf{m}}{A\mathbf{v}^k}\right], \tag{4.14}$$

where $\mathbf{D}$ denotes the derivative operator.

4.3.2.2 Total variation regularization

In this section we assume a smoothness requirement on the discrete solution $\mathbf{u}$. Rudin *et al.* [90] introduced the total variation (TV) regularization for imaging problems to preserve sharp structures, while removing noise in the images. The roughness penalty functional, defined by the TV of the solution $\mathbf{v}$ is:

$$J(\mathbf{v}) = |\mathbf{v}|_{\mathrm{TV}}. \tag{4.15}$$

Here we employ the anisotropic discretization of the TV norm[127]:

$$|\mathbf{v}|_{\mathrm{TV}} = \sum_i \left(|(\nabla_x \mathbf{v})_i| + |(\nabla_y \mathbf{v})_i|\right), \tag{4.16}$$

where $\nabla_x\mathbf{v}$ and $\nabla_y\mathbf{v}$ are the horizontal and vertical derivatives, which are discretized here as one-sided forward differences [128].

When minimizing the negative penalized log-likelihood, $-L(\mathbf{v}) + \lambda J(\mathbf{v})$, the minimizer of the $J(\mathbf{v})$ functional satisfies the corresponding Euler-Lagrange equation, $\mathtt{div}\frac{\nabla\mathbf{v}}{|\nabla\mathbf{v}|} = 0$ and the update scheme of the OSL algorithm with TV regularization (OSL-TV) finally reads [129]:

$$\mathbf{v}^{k+1} = \frac{\mathbf{v}^k}{A^T\mathbf{1} + \lambda \cdot \mathtt{div}(\frac{\nabla\mathbf{v}}{|\nabla\mathbf{v}|})_k}\left[A^T\frac{\mathbf{m}}{A\mathbf{v}^k}\right]. \tag{4.17}$$

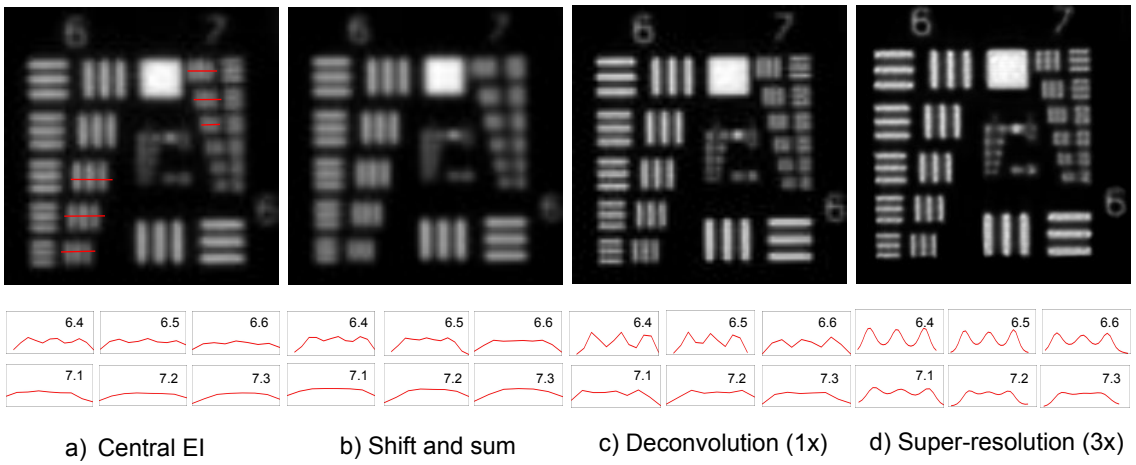

Figure 4.5: Reconstruction of the USAF 1951 resolution target. **Top:** (a) Raw elemental image of the resolution target acquired with our experimental FiMic (shown is a close up on groups 6 and 7 of the central elemental image). (b) The post-acquisition refocused image using the popular algorithm of shifting views and summing up [130]. (c) The deconvolved image at sensor resolution. (d) The reconstructed image at a 3x super-sampling of the object space, exploiting complementary multi-view aliasing in the elemental images. **Bottom:** Line profiles through the elements 6.4 to 7.3 of the images above. While the elemental image (a) and the refocused image (b) resolve up to element 6.4 (11 μm), the deconvolution resolves up to element 6.6 (8.8 μm) in (c) and element 7.1 (7.8 μm) in the computationally super-resolved image (d).

4.4 Experiments and results

In order to demonstrate the potential of our method, the deconvolution results in this section were obtained at various super-sampling factors and compared with the the refocusing algorithm of pixel shifting and summing [130] and with the central EI of the raw image. All the results were obtained after 50 iterations of the scheme in Eq. (4.12), which coincides with a drop in the improvement rate (based on the absolute square difference from the previous iteration) below 10^{-2} and the solutions were initialized with uniform white texture.

It is important to note that the factor s relates to the sampling rate we chose for reconstructing the volumes and has nothing to do with the actual details that can be recovered, which is the effective resolution of the FiMic as addressed in section 4.2. We refer the interested reader to existing discussions on the subject [59, 71, 124].

The experiments in this chapter were performed with a custom-built FiMic containing a MLA with $f_{ml} = 6.5mm$, $\mu_{\text{lens}} = 1.0mm$ (AMUS APH-Q-P1000-R2.95) and an infinity corrected MO ($f_{obj} = 9.0mm$ and $NA_{obj} = 0.4$). For recording the images we used a CMOS camera (EO-5012c 1/2") with pixel pitch $\rho_{px} = 2.2\mu m$.

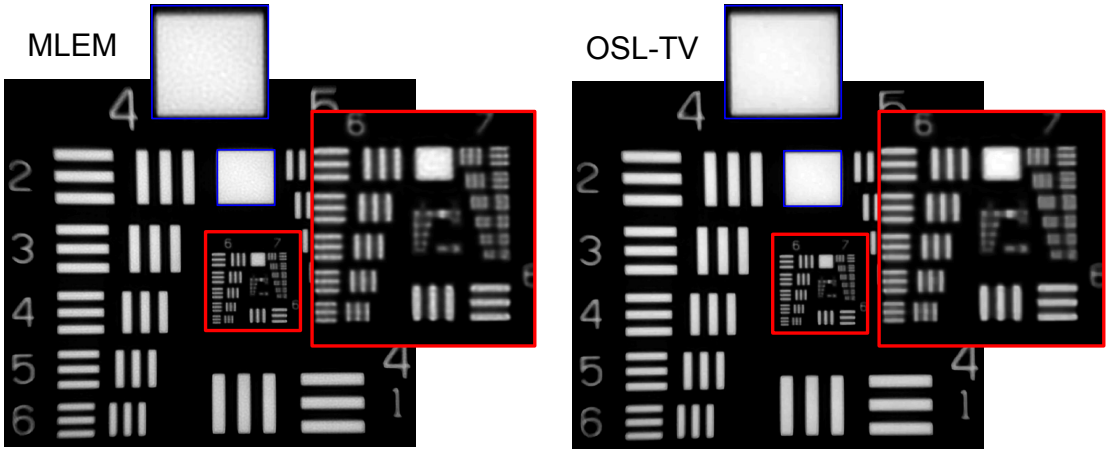

Figure 4.6: Close-up on the reconstruction of the USAF resolution target: MLEM (left) and OSL-TV (right). The regularized reconstruction ($\lambda = 0.001$) produces a smooth image, while preserving the sharp discontinuities as expected.

4.4.1 Analysis of the reconstruction resolution

For the USAF-1951 resolution target imaged at the front focal plane, Fig. 4.5 shows superior results for the deconvolution compared to the well known *shift and sum* refocusing algorithm [130] used in the baseline work by Scrofani *et al.* [71]. When employing total variation regularization during the reconstruction, using the penalized likelihood fomulation in Eq. (4.17), the solution becomes smoother while the sharp details are preserved; see Fig. 4.6. We have further imaged the USAF-1951 resolution target at various axial positions in the [-120,120]μm range using our experimental setup. As mentioned in section 4.1, since the AS was not mechanically accessible, we used an optical relay system ($f_1 = 125mm$, $f_2 = 200mm$) to conjugate the AS plane and the MLA plane. This configuration fits $N = 11.5$ micro-lenses in the AS. Under the resolution criterions in Eq. (4.3) and Eq. (4.4), the expected lateral resolution limit (when $\lambda = 480nm$) of this setup is at best $\delta_{diff} = 6.9\mu m$, while the sensor sampling resolution is $\delta_{sensor} = 9.7\mu m$. On the USAF resolution target, these values are approximately represented by the elements 7.2 and 6.5, respectively. Fig. 4.7(a) shows the central EI of the raw FiMic image (green), the shift and sum refocusing algorithm (yellow), our deconvolution at object space sampling $s = 1$ (red) and $s = 3$ (blue) of the groups 6 and 7 of the USAF 1951 resolution target placed at $\Delta z = \{0, -20, -50, -100\}\mu m$. To characterize the recoverable resolution of our FiMic configuration, in Fig. 4.5 we display line profiles for elements 6.4 to 7.3 of the USAF target arbitrarily placed at $\Delta z = -80\mu m$. To determine if one element is resolved, we check for the existence of an intensity dip of 25% [60]. The central EI, and similarly the refocused image, resolves up to element 6.4, which corresponds to a lateral resolution of $11\mu m$. By removing the out-of-focus blur, the deconvolution ($s = 1$) resolves up to element 6.6 ($8.8\mu m$). And by fusing the aliased information in the EIs, in the super-resolved reconstruction ($s = 3$), we can recover element 7.1, corresponding to $7.8\mu m$. It is worth remarking here that the difference between δ_{diff} and δ_{sensor} changes with the number of sub-aperture images, N. It quickly follows from the definitions in Eq. (4.3) and Eq. (4.4), that when $\lambda < 4NA_{ml}\rho_{px}$, the more angular samples we record, the more under-sampled they are by the system. For our configuration, this inequality is well satisfied and thus the potential for computational super-

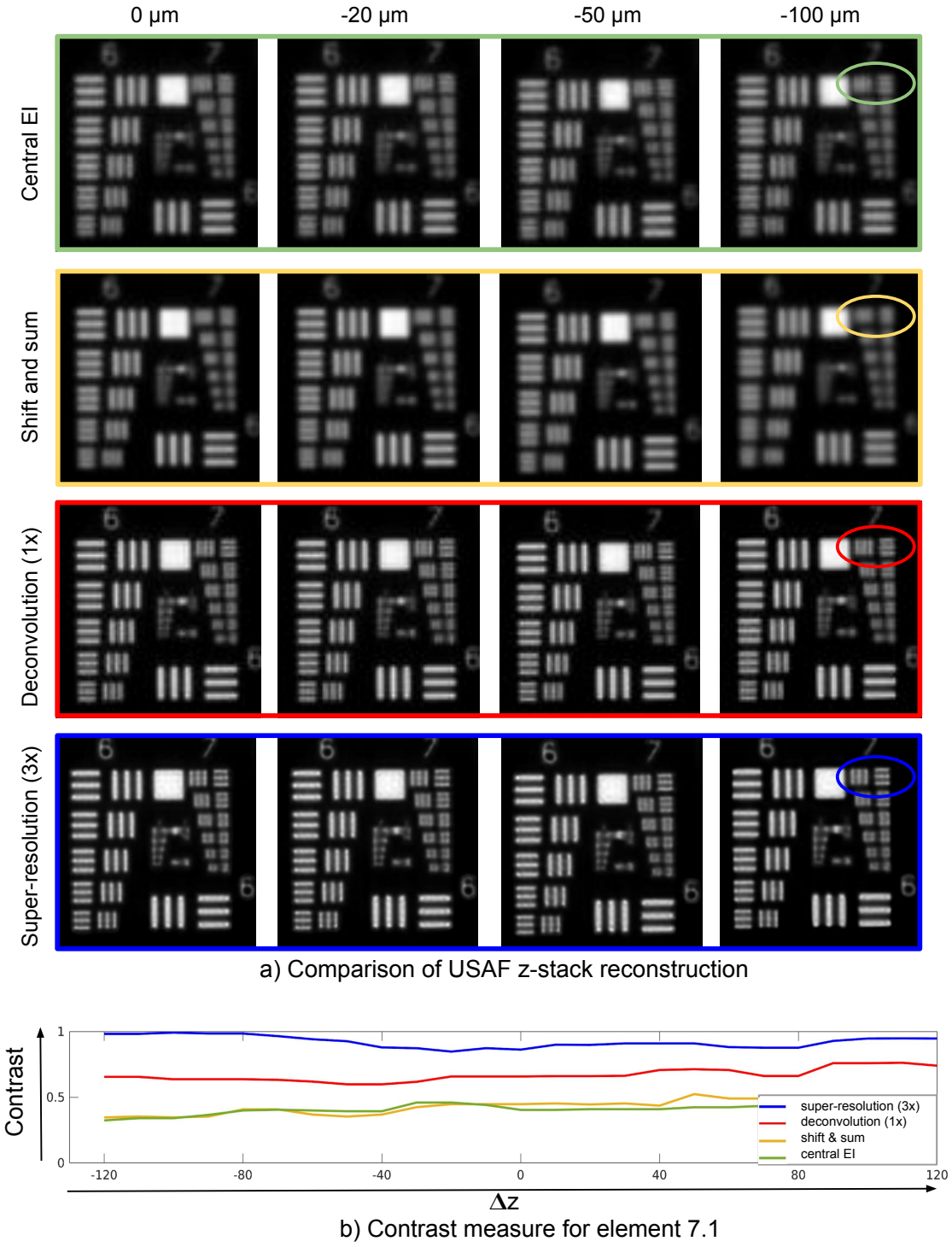

Figure 4.7: Reconstruction of the USAF 1951 target imaged at Δz = [-120, 120] μm. a) Example central EI of the FiMic image (green), the refocused image (yellow), the deconvolved image at sensor resolution (red), the deconvolved image at 3x sensor resolution (blue) for arbitrarily picked axial positions $\Delta z = \{0, -20, -50, -100\}$. When compared to the raw and refocused images, the deconvolved images appear to better resolve details through deblurring. Element 7.1 appears resolved in the super-resolved image (blue oval). b) Contrast of the USAF element 7.1 over Δz = [-120, 120] μm is generally constant for all the methods in a). As expected, the super-resolved deconvolution shows the best contrast.

resolution. On the other hand, although we record $N = 11.5$ views, this does not dictate the actual improvement factor we can obtain via super-sampling, which is rather determined by the density and the level of distinction in the aliasing patterns the EIs exhibit and ultimately band limited. For the presented USAF target images, reconstructing at $s > 3$ did not improve the resolution any further.

Finally, in order to analyze the behaviour of the reconstruction regarding object axial positioning, we compute the contrast measure $c = (I_{max} - I_{min})/(I_{max} + I_{min})$ [67, 131], for the element 7.1 for each method in Fig. 4.7(a), over the [-120,120]μm axial range. I_{max} and I_{min} are the minimal and maximal intensities along a line perpendicular to the stripes of the element 7.1 The final contrast (average of the vertical and horizontal stripes contrasts) as a function of depth is aggregated for all the discussed methods in Fig. 4.7(b). In agreement with the analysis in Fig. 4.5, the central EI and the refocused image show low contrast when compared to the deconvolved and super-resolved images. And very importantly, the plots suggest that the variation in contrast over the axial position is rather low, which means the lateral resolution in FLFM is uniform across depth, unlike in conventional LFM, where the resolution is highly non uniform.

4.4.2 Reconstruction of a real 3D sample

We further evaluate the proposed methods on real volumetric data of cotton fibers.

Fig. 4.8(a) (left) shows a raw FiMic image of cotton fibers captured with our experimental setup configured in a similar way as in the previous section. This time, the relay lenses, RL1 and RL2 have focal lengths $f_1 = 50mm$ and $f_2 = 40mm$, which introduce a relay magnification, $M_{relay} = 0.8x$. Under red light with $\lambda = 680nm$, the expected lateral resolution limit for this configuration is $\delta_{diff} = 4.9\mu m$ and the sensor sampling resolution is about the same. In order to evaluate our proposed computational super-resolution algorithm, we binned the pixels ($2x2$) in the LF image to artificially double the sensor pixel size. This results in $\delta_{sensor} = 9.8\mu m$. The LF image is shown in Fig. 4.8(a) together with zoomed-in regions of an EI for details. We reconstructed the sample over an axial range of Δz = [-150,150]μm for every 10 μm at super-sampling rates $s = 1$ and $s = 4$ as displayed in Fig. 4.8(b) and Fig. 4.8(c). While in both cases we see details that are not visible in the raw image, the improvement in the super-resolved deconvolution is evident. The close-up in Fig. 4.8(c), as well as the xz and xy projections cleary show structure that are not resolved in the normal deconvolution in Fig. 4.8(b).

4.5 Discussion

Fourier light field microscopy addresses the limitations in conventional LFM, where computational super-resolution has a major impact. It is then natural to ask ourselves if there is something we can do computationally to improve the resolution in this different FLFM arrangement. When inspecting fluorescence specimens, the camera pixels need to be relatively large to cope with low light conditions. Then for certain FiMic setup configurations, the light field signal is under-sampled.

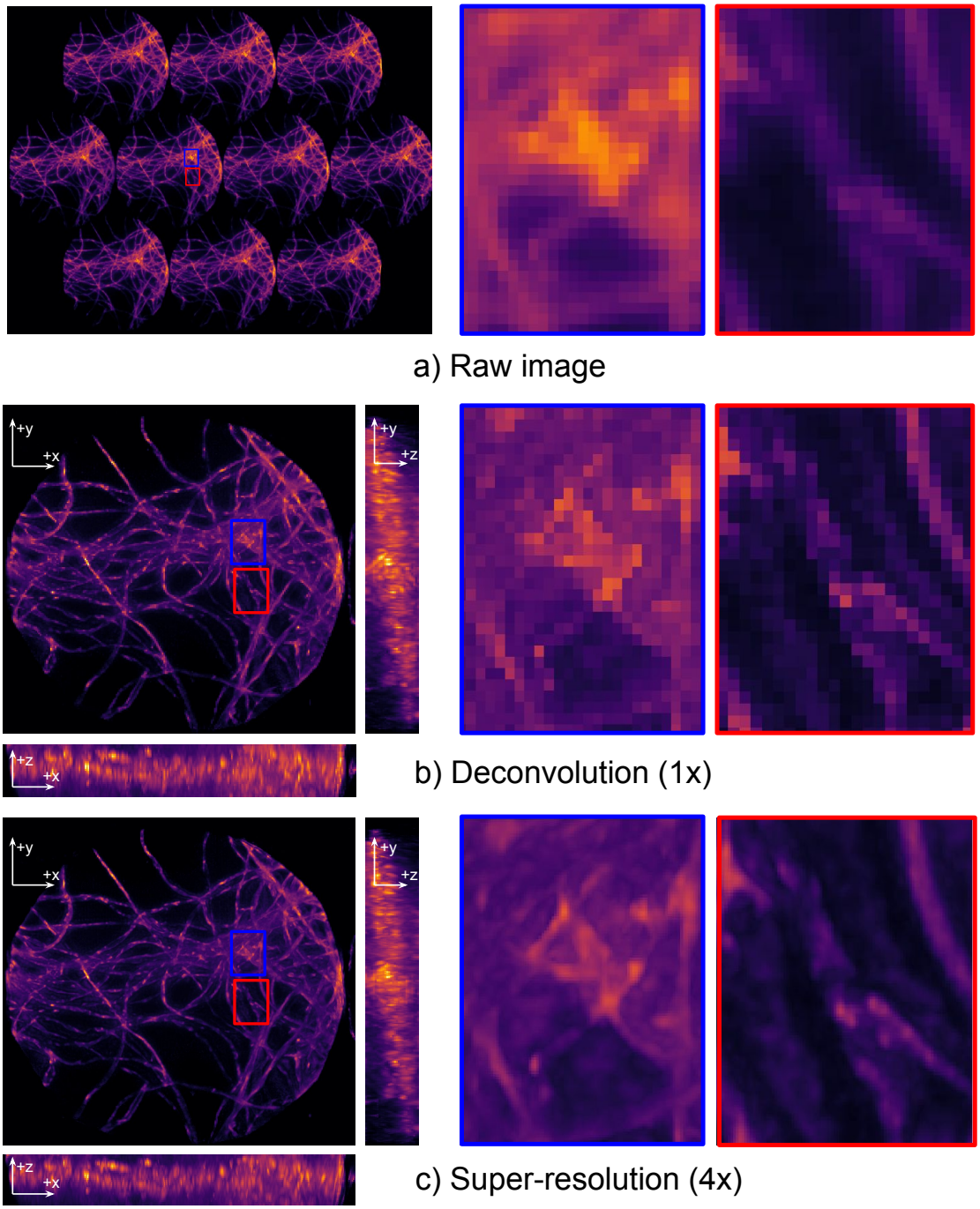

Figure 4.8: 3D reconstruction of cotton fibers. a) Raw image acquired with our experimental FiMic setup and zoomed-in regions of an EI for details. b) Maximum intensity projections (MIPs) and zoomed-in regions of the 3D reconstructed sample (Δz = [-150,150]μm) using our proposed method at sensor resolution ($s = 1$). c) MIPs of the super-resolved 3D reconstruction at 4x sensor resolution ($s = 4$). The deconvolved images resolve structures structures that do not show in the EI. The close-ups in b) and c) clearly shows that the super-resolved reconstruction recovers fine details in the sample, that are not resolved in the normal deconvolution.

In this chapter we analyze the sampling requirements in FLFM to understand how the sampling rate of the camera pixels impacts the recoverable spatial resolution through volumetric deconvolution. We then derive a flexible wave-based light field point spread function and use it to perform 3D reconstruction. The methods we develop in this work are related to computational super-resolution techniques used in computer vision and computational photography, where sub-pixel shifts (or sub-lenslet shifts in conventional light field photography) between multiple aliased views of the same scene are combined to recover an image at sub-pixel resolution. A feature that inherently characterizes the orthographic images captured in FLFM, when working with fluorescent samples, is the under-sampling of the PSF. This happens due to the sensitivity and noise requirements of the camera sensors, which are often met by the use of large pixels. Note that this problem does not occur in conventional fluorescence microscopy due to the large magnification factor between the object and the sensor planes. We demonstrate, using experimental images of the USAF 1951 resolution target, that when the system samples the light field below its band limit, computational super-resolution is possible to some extent. Hence, successful deconvolution fuses the complementary information in aliased perspective views to recover high frequency details in the imaged scene. We further evaluate the proposed methods for volumetric samples (cotton fibers) and show superior 3D reconstruction quality over state-of-the-art methods.

Part IV

3D reconstruction software

CHAPTER 5

oLaf - A flexible Matlab framework for 3D reconstruction of LFM data

oLaF [1] is a flexible Matlab framework for 3D reconstruction of light field microscopy data. It is designed to cope with various LFM configurations in terms of MLA type (regular vs. hexagonal grid, single-focus vs. mixed multi-focus lenslets) and MLA placement in the optical path (original 1.0 vs. defocused 2.0 LFM vs. Fourier LFM designs).

Acknowledgments

oLaF evolved gradually improving and expanding on the functionality in [44]. Where possible, the naming conventions were kept for the sake of relatability and convenience of the shared users. The pre-processing of the raw light field images relies on the image rectification functionality [132] in the Light Field Toolbox for Matlab by Donald G. Dansereau.

[1] `https://gitlab.lrz.de/IP/olaf`

5.1 A tutorial

5.1.1 LFM vs. FLFM

oLaF deals with 3D reconstruction of data from both conventional light field microscopy (LFM) and Fourier light field microscopy (FLFM). While both modalities make use of a micro-lens arrays to record the spatio-angular light field information, they are in many ways conceptually different. In this sense, *oLaF* distinguishes between LFM and FLFM functionality and in the following we will demonstrate each of them separately. To make the distinction clear, we employ the *LFM* prefix for the LFM related function names and *FLFM* for the FLFM related ones; see appendix.

5.1.2 Getting started

Clone or download *oLaF* at `https://gitlab.lrz.de/IP/olaf` into a location of choice and run the script `olaf/Code/import2ws.m` to set up the Matlab path. Every time Matlab restarts, this script needs to be re-run. Alternatively, add it to `startup.m`.

`olaf/SampleData/` contains several example light field datasets, acquired with various conventional LFM and FLFM setups. Every dataset contains a raw light field image, a white image (in case of LFM) or a calibration image (in case of FLFM) used for detecting the micro-lens centers and a YAML file describing the microscope configuration parameters. Fig. 5.1 displays three such datasets.

5.1.3 Step-by-step reconstruction of conventional LFM data

`olaf/Code/mainLFM.m` serves as a step-by-step demo script of the LFM related functionality in oLaF v3.0.

You can switch between datasets by un-commenting the associated lines at the beginning of the script. Different `depthRange` and `depthStep` are suggested for different datasets in order to keep a low runtime for demonstration purposes. The impact of `depthRange` on the runtime is discussed in Sec. 5.4.1.

5.1.3.1 Loading datasets

```
[LensletImage, WhiteImage, configFile] = LFM_selectLFImages(dataset);
```

is a convenience function for loading the light field image together with the corresponding white image and a configuration file containing the acquisition specific parameters, for a given dataset. Note, the raw light field images are cropped to a region of interest (ROI), as depicted

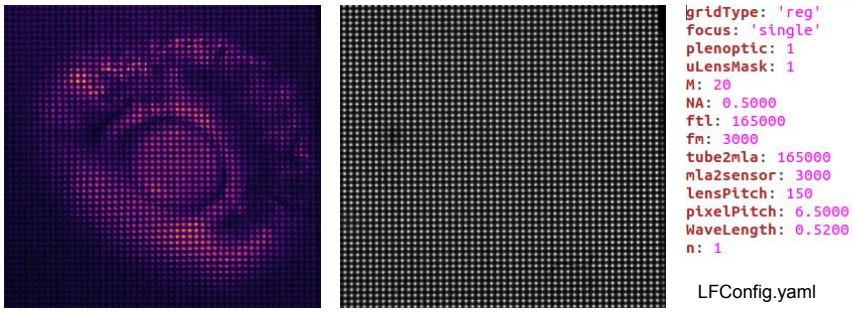

(a) Zebrafish eye: Single focal length, regular grid micro-lens array; original LFM setup.

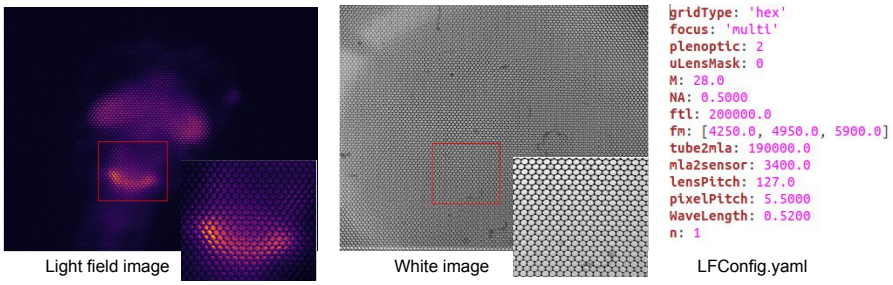

(b) Zebrafish brain: Multi focus, hexagonal grid micro-lens array; defocused LFM setup.

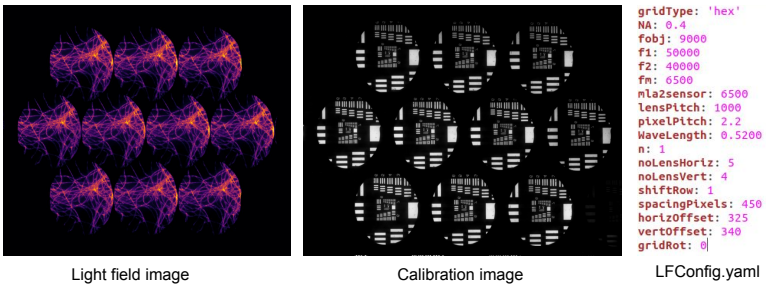

(c) Cotton fibers: Hexagonal grid micro-lens array; FLFM setup.

Figure 5.1: Example light field data sets.

in Fig. 5.1 (b), in order to speed up the computations. For the provided datasets the ROIs are predefined. However, you can choose custom regions using the built-in Matlab interactive function `getrect()`:

```
figure; imagesc(LensletImage);
rect = round(getrect);
```

5.1.3.2 User Inputs.

When reconstructing a light field image, the user decides the resolution related parameters:

```
depthRange % the axial range (in μm) of the reconstructed volume,
% relative to the focal plane of the objective lens,
% e.g., depthRange = [-20,20].
```

```
depthStep % represents the axial resolution (in μm) of the
% reconstructed object.
```

```
newSpacingPx % the desired spacing (in number of pixels) between
% neighboring lenslet centers. This parameter was introduced to
% allow for up-/down-sampling of the raw lenslet image.
newSpacingPx = 'default' % means no up-/down-sampling i.e.,
% newSpacingPx = spacingPx (spacingPx is the real lenslet spacing
% given by the micro-lens pitch and the camera sensor pixel pitch).
% newSpacingPx controls the sensor resolution and the lenslet
% image is interpolated to this user-specified pixel spacing,
% prior to reconstruction.
```

```
superResFactor % controls the lateral resolution of the reconstructed
% object. It is interpreted as a multiple of the lenslet resolution
% (1 voxel/lenslet).
superResFactor = 'default' % means the object is reconstructed at
% sensor resolution, while superResFactor = 1 means
% lenslet resolution.
```

5.1.3.3 Light field microscope (LFM) setup descriptor.

```
Camera = LFM_setCameraParams(configFile, newSpacingPx);
```

builds the `Camera` structure based on the fields in the `configFile`. A configuration file (see Fig. 5.1 (a) and (b)) typically contains the following LFM setup specific parameters:

```
gridType % micro-lens array grid type;
gridType = 'reg' % for regular grid array;
gridType = 'hex' % for hexagonal grid array.
```

```
focus % flag for the micro-lens array type;
focus = 'single' % when all the micro-lens in the array have the same
% focal length;
focus = 'multi' % when the array contains three mixed focal lengths
% in a hexagonal grid; see Fig.5.6.
```

```
fm % the focal length of the micro-lens; when focus = 'multi',
% fm is an array (see Fig.5.1 (b)).
```

```
plenoptic % flag for the LFM configuration;
plenoptic = 1 % for the original LFM design (1.0);
plenoptic = 2 % for the defocused LFM design (2.0, tube2mla ≠ ftl).
```

```
uLensMask % flag for micro-lens shape mask;
uLensMask = 1 % when there is no space between micro-lens
% e.g., regular grid array with square aperture micro-lens;
uLensMask = 0 % when there is space between micro-lens
% e.g., circular aperture.
```

```
M % objective magnification;
NA % objective numerical aperture;
ftl % focal length of the tube lens (in μm);
lensPitch % micro-lens pitch (in μm);
pixelPitch % sensor pixel pitch (in μm).
```

```
tube2MLA % distance between the tube lens and MLA
% tube2MLA = ftl in original LFM design, i.e. when plenoptic = 1
% When tube2MLA is not known from the acquisition (measuring was
% not possible), set tube2MLA = 0 in the YAML configuration file.
% Then the function:
tube2MLA = computeTube2MLA(lensPitch, mla2sensor, deltaOT,...
                objRad, ftl) % computes tube2MLA such that
% the effective image-side NA of the tube lens matches
% the effective NA of the micro-lenses i.e., the micro-images
% optimally fill the sensor without overlapping.
% Here deltaOT is the distance between the objective and the tube
% lens, usually deltaOT = ftl + fobj for commercial microscopes.
```

```
mla2sensor % distance between the MLA and sensor;
% set mla2sensor = 0 in the configuration file if tube2MLA is known
% and mla2sensor has to be retrieved such that the F-number matching
% condition is satisfied.
```

```
wavelength % wavelength of the emission light;
n % refraction index (1 for air).
```

Based on the input parameters and the ones in the configuration file, the function

```
Camera = LFM_setCameraParams(configFile, newSpacingPx)
```

computes extra parameters relevant for the reconstruction; these are described in Sec. 5.2.1.

5.1.3.4 Retrieve lenslet centers and related data structures.

For every image/dataset to be reconstructed, an associated white image needs to be provided in order to detect the lenslet centers; Fig. 5.1 (a) and (b) show example light field (lenslet) and white images.

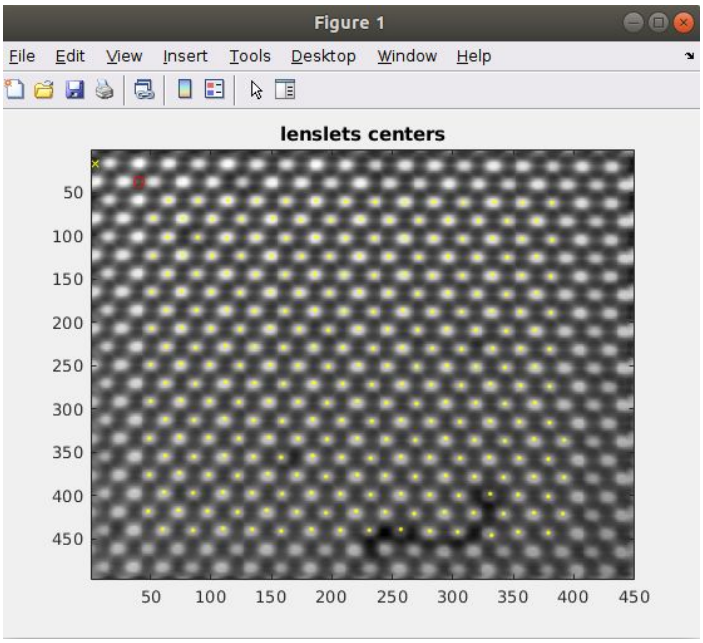

Figure 5.2: Detected micro-image centers in a white image.

The function

```
[LensletCenters, Resolution, LensletGridModel, NewLensletGridModel]...
        = LFM_computeGeometryParameters(...
                Camera, WhiteImage, depthRange, depthStep,...
                superResFactor, DebugBuildGridModel, imgSize)
```

uses such a white image, `WhiteImage`, together with the `Camera` structure and the user inputs to retrieve the lenslet centers and builds several data structures relevant for the 3D reconstruc-

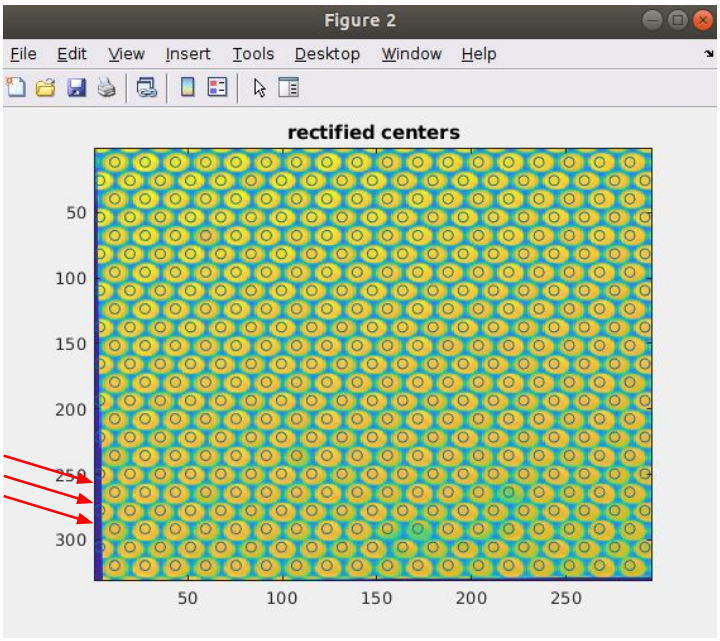

Figure 5.3: Rectified micro-lens centers after the `NewLensletGridModel` matching transformation.

tion process. Details on the implementation of this function and the returned data structures are given in Sec. 5.2.1.

5.1.3.5 Compute the light field point spread function.

The function

```
[H, Ht] = LFM_computeLFMatrixOperators(...
                Camera, Resolution, LensletCenters)
```

uses the data structures introduced in the previous section to pre-compute the forward (`H`) and backward (`Ht`) light transport patterns. `H` describes the discrete light field point spread function (LFPSF), and `Ht` describes the inverse light propagation.

Sec. 5.3.1 describes in detail the functionality implemented by this function.

5.1.3.6 Correct/rectify light field images.

Prior to the reconstruction, the input light field image is transformed to match the `NewLensletGridModel`. For this purpose, we retrieve the 2D affine transformation between the original and new (user defined) grids, `LensletGridModel` and `NewLensletGridModel`:

```
FixAll = LFM_retrieveTransformation(LensletGridModel,...
                                    NewLensletGridModel)
```

and apply this transformation to the light field and white images:

```
[CorrectedLensletImage, CorrectedWhiteImage]...
        = LFM_applyTransformation(LensletImage, WhiteImage, FixAll,...
        LensletCenters, debug)} % When debug = '1', the...
        % transformed white image (with overlaid rectified
        % centers) is displayed for a visual check like in Fig.5.3.
```

While transforming both images, due to the rotation without cropping, the rectified images show some zero borders, as pointed out by the red arrows in Fig. 5.3. In order to even out these parts, for smooth visualization of the subsequent reconstruction result, we apply a pre-processing step:

```
correctedLensletImage(correctedLensletImage <...
                                mean(correctedLensletImage(:)))...
                                = mean(correctedLensletImage(:))
```

however, this is optional, and other strategies may be used.

5.1.3.7 Set forward/backward projection operators.

The forward projection operators are functions which use the forward projection patterns (`H`) to simulate a light field image from a 3D volume (object), and the backward projection operators are meant to do the inverse mapping, i.e. generate the 3D object from a lenslet image by applying the pre-computed back-projection patterns (`Ht`).

Based on the `Camera.focus`, function pointers are set up to be passed to the deconvolution routine.

When `Camera.focus = 'single'`:

```
forwardFUN = @(object) LFM_forwardProject( H, object, ...
        LensletCenters, Resolution, imgSize, Camera.range);
backwardFUN = @(projection) LFM_backwardProject(Ht, projection,...
        LensletCenters, Resolution, texSize, Camera.range).
```

In case `Camera.focus = 'multi'`, we use projection operators which adapt the func-

tionality to multi-focus MLA setups (H, Ht contain multi-focus patterns, as discussed in Sec. 5.3.1):

```
forwardFUN = @(object) LFM_forwardProjectMultiFocus( H, object,...
        LensletCenters, Resolution, imgSize, Camera.range);
backwardFUN = @(projection) LFM_backwardProjectMultiFocus(Ht,...
        projection, LensletCenters, Resolution, texSize, Camera.range).
```

imgSize and texSize are pre-computed light field image and volume container sizes; they are different when we reconstruct at a different resolution than sensor resolution.

5.1.3.8 3D reconstruction.

Once we have all the necessary ingredients we proceed to 3D reconstruct the light field image, correctedLensletImage.

The function

```
reconVolume = deconvEMS(forwardFUN, backwardFUN, LFimage, it,...
        initVolume, filterFlag, lanczos2FFT, onesForward, onesBack)
```

implements the Estimate-Maximize-Smooth deconvolution algorithm we presented in [68]. The arguments are described below:

```
forwardFUN / backwardFUN % the function pointers set previously
LFimage = correctedLensletImage;
initVolume = ones([texSize, length(Resolution.depths)]); % initial
% guess
it % the number of iterations
filterFlag % when filterFlag = 0, deconvEMS implements the
% Richardson-Lucy deconvolution, otherwise, when filterFlag = 1,
% deconvEMS implements the depth-dependent aliasing-free
% deconvolution with smoothing step as described in [68];
```

```
lanczos2FFT = LFM_buildAntiAliasingFilter([texSize,...
        length(Resolution.depths)], widths, lanczosWindowSize);
        % contains the depth-dependent anti-aliasing filter kernels,
        % used in the smoothing step of the EMS algorithm.
        % When filterFlag = 0, lanczos2FFT argument can be [].

        widths = LFM_computeDepthAdaptiveWidth(Camera, Resolution);
        % are the ideal filter radii, computed based on the LFM
        % depth-dependent sampling. There is one computed width
```

```
        % per object depth.
        lanczosWindowSize % is the size of the Lanczos window used
        % to implement the ideal filters. Typically, in our
        % experiments, lanczosWindowSize = 2,3
```

```
onesForward / onesBackward % are used for background correction
% during deconvolution, to cope with the illumination and noise
% effects imbalances in real images:
        onesvol = ones(size(initVolume));
        onesForward = forwardFUN(onesvol);
        onesBack = backwardFUN(onesForward);
% When using the EMS deconvolution (filterFlag = 1),
% the background normalization is not necessary, as the
% smoothing step keeps the process stable over the iterations.
```

For more details on the implementation of the deconvolution, see the corresponding Matlab files. For the theory behind the EMS deconvolution algorithm, check out [68].

5.1.4 Step-by-step reconstruction of Fourier LFM data

`olaf/Code/mainFLFM.m` serves as a step-by-step demo script of the FLFM related functionality in oLaF v3.0 using the example dataset shown in Fig.5.1 (c).

5.1.4.1 User Inputs.

Once the `LensletImage`, `CalibrationImage` and `configFile` are loaded, the user decides the resolution related parameters:

```
depthRange % is the axial range (in μm) of the reconstructed
% volume, relative to the front focal plane of the microscope
% objective lens, e.g., depthRange = [-80,80];
depthStep % represents the axial resolution (in μm) of the
% reconstructed object.
```

```
superResFactor % controls the lateral sampling rate of the
% reconstructed object. When superResFactor == 1 the volume is
% reconstructed at the resolution of the sub-aperture images.
% Conversely, superResFactor > 1, the object is discretized
```

```
% at a sampling rate superResFactor times the sensor sampling rate.
% The LensletImage (as well as the CalibrationImage) is upsampled
% accordingly using the nearest neighbor method.
```

5.1.4.2 Fourier light field microscope (FLFM) setup descriptor.

The function

```
[Camera, LensletGridModel] = FLFM_setCameraParams(configFile,...
                                                  superResFactor)
```

builds the `Camera` and `LensletGridModel` structures based on the fields in the `configFile`. A configuration file (see Fig. 5.1 (c)) typically contains the following FLFM setup specific parameters:

```
gridType % micro-lens array grid type. gridType = 'reg'
% for regular grid array; gridType = 'hex' for hexagonal
% grid array.
NA % numerical aperture of the microscope objective
fobj % focal length of the microscope objective lens
f1 / f2  % focal lengths of the two relay lenses
fm % focal length of the micro-lens
mla2sensor % distance between the MLA plane and camera sensor plane
lensPitch % micro-lens pitch (in μm)
pixelPitch % sensor pixel pitch (in μm)
wavelength % wavelength of the emission light
n % refraction index (1 for air).
```

The `configFile` also contains parameters describing the micro-lens array. These are usually rough estimates (by analyzing the `LensleImage` of the `CalibrationImage`) and they will be refined later, as discussed in section 5.2.2:

```
noLensHoriz / noLensVert % the number of micro-lens in the array
% to match the sensor extent

spacingPixels % the number of pixels between two horizontally
% neighboring lenslets

horizOffset / vertOffset % the coordinates of the center of the
% first (upper left corner) whole elemental image in the LensleImage
%  or the CalibrationImage

shiftRow % whether odd (shiftRow = 1) or even (shiftRow = 2)
% represents the number of rows that are half diameter
```

```
% shifted in case of hexagonal grids

gridRot % the rotation of the grid with respect to the optical axis
```

Based on the input parameters and the ones in the configuration file, the function

```
[Camera, LensletGridModel] = FLFM_setCameraParams(configFile,...
                                        superResFactor)
```

computes extra parameters relevant for the reconstruction; these are described in Sec. 5.2.2.

5.1.4.3 Retrieve lenslet centers and resolution related parameters.

For every image to be reconstructed, an associated calibration image needs to be provided in order to detect the lenslet centers; Fig. 5.1 (c) shows an example light field image and a corresponding calibration image. A calibration image is an image of an object (usually, but not necessarily, a resolution target) placed at the front focal plane of the microscope objective, so that the centers of the micro-lens coincide with the centers of the elemental images.

The function

```
[LensletCenters, Resolution] =...
        FLFM_computeGeometryParameters(CalibrationImage,...
        Camera, LensletGridModel, depthRange, depthStep)
```

uses such a `CalibrationImage`, together with the `Camera` and `LensletGridModel` data structures and the user inputs to retrieve the lenslet centers and compute several resolution related parameters that are relevant for the 3D reconstruction process.

Details on the implementation of this function are given in Sec. 5.2.2.

5.1.4.4 Compute the light field point spread function.

The function

```
[H, Ht] = FLFM_computeLFMatrixOperators(Camera, Resolution)
```

uses the data structures introduced in the previous sections to precompute the forward (`H`) and backward (`Ht`) light transport patterns. `H` describes the discretized 3D light field point spread function (LFPSF), and `Ht` is its transpose.

Sec. 5.3.2 describes the functionality provided by the FLFM_computeLFMatrixOperators function.

5.1.4.5 3D reconstruction.

The forward projection operator is a function which uses the pre-computed LFPSF (H) to simulate a light field image from a 3D volume (object), and the backward projection operator is meant to do the inverse mapping, i.e. generate the 3D object from a lenslet image by applying the pre-computed back-projection model (Ht).

We set up function pointers for the projectors to be passed to the deconvolution routine:

```
forwardFUN = @(volume) FLFM_forwardProject(H, volume);
backwardFUN = @(projection) FLFM_backwardProject(Ht, projection);
```

Once we have all the necessary ingredients we proceed to deconvolved the light field image, LensletImage.

The function

```
recon = deconvRL(forwardFUN, backwardFUN, LensletImage, iter, init)
```

implements the Richardson-Lucy deconvolution algorithm as presented in [133]. The arguments are described below:

```
forwardFUN / backwardFUN % the function pointers set previously;
LensletImage % the raw light field image we want to 3D reconstruct;
iter % the number of iterations;
init % the initial solution guess; usually a uniform white object
% init = ones(volumeSize).
```

Alternatively, the function

```
recon = deconvOSL(forwardFUN, backwardFUN, LensletImage,...
                iter, init, lambda)
```

implements the One-Step-Late algorithm which combines the Richardson-Lucy deconvolution with a total variation (TV) prior on the data to be reconstructed as presented in [129]. The additional argument, lambda represents the regularization parameter.

The axial slices of the 3D reconstructed object have the same size as the light field image (in terms of number of pixel), for the ease of use of the convolution operation (see section 5.4.2). However, the actual field of view of the microscope is smaller (it matches an elemental image

size in terms of number of pixels; see section 5.2.2). We compute the field of view (`fovRangeX` and `fovRangeY`) and crop the `recon` accordingly:

```
reconCropped = recon(fovRangeY, fovRangeX, :)
```

5.2 Microscope geometry

5.2.1 LFM setup

Based on the setup description (from user inputs and configuration file), the function below computes extra parameters relevant for the reconstruction:

```
Camera = LFM_setCameraParams(configFile, newSpacingPx)
```

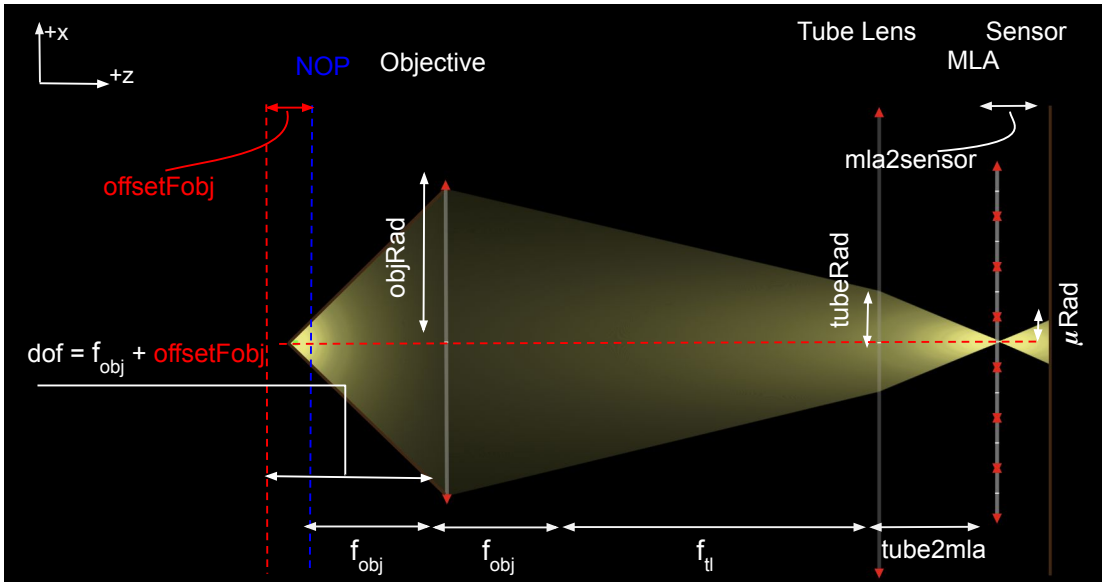

Figure 5.4: LFM setup specific quantities.

```
Camera.range % when gridType = 'reg' we exploit the symmetry
% of the discrete volume relative to the system's optical axis.
% Then we can pre-compute the light field point spread
% function (LFPSF) for a reduced (one quarter) set of source
% point positions. In this case we set Camera.range = 'quarter'.
% When gridType = 'hex', unfortunately, the discretization does
% not allow for such optimization and we set Camera.range = 'full'
% For a detailed explanation see Sec. 5.3.1.
```

```
Camera.fobj % focal length of the objective lens
Camera.fobj = Camera.ftl/Camera.M;

Camera.DeltaOT % objective to tube lens distance
Camera.DeltaOT = Camera.ftl + Camera.fobj; % for 4-f systems

Camera.spacingPx % number of pixels behind a micro-lens
Camera.spacingPx = Camera.lensPitch/Camera.pixelPitch;

Camera.newSpacingPx % as specified by the user
% See paragraph 5.1.3.2.

Camera.newPixelPitch % sensor pixel pitch corresponding to the
% new micro-lens spacing.
Camera.newPixelPitch = Camera.lensPitch / newSpacingPx;

Camera.k % wave number
Camera.k = Camera.n/Camera.WaveLength % 2*π

Camera.dof % an object at a distance Camera.dof in front of
% the objective is focused on the MLA by the tube lens.
% Fig.~5.4 depicts dof together with all the relevant
% LFM quantities.

Camera.offsetFobj % the offset from fobj to dof
Camera.offsetFobj = Camera.dof - Camera.fobj;

Camera.objRad % radius of the objective lens
Camera.objRad = Camera.fobj * Camera.NA

Camera.uRad % radius of the micro-image formed on the sensor
% for an object depth focused on the MLA by the tube
% lens (Camera.dof). μRad is depicted in Fig.5.4.

Camera.tubeRad % effective tube lens radius.
% It represents the radius of the wave-front distribution
% incident on the tube lens, for a source point at dof;
% see Fig.5.4.
```

The function

```
[LensletCenters, Resolution, LensletGridModel, NewLensletGridModel] =
        LFM_computeGeometryParameters(Camera, WhiteImage,...
        depthRange, depthStep, superResFactor,...
        DebugBuildGridModel, imgSize)
```

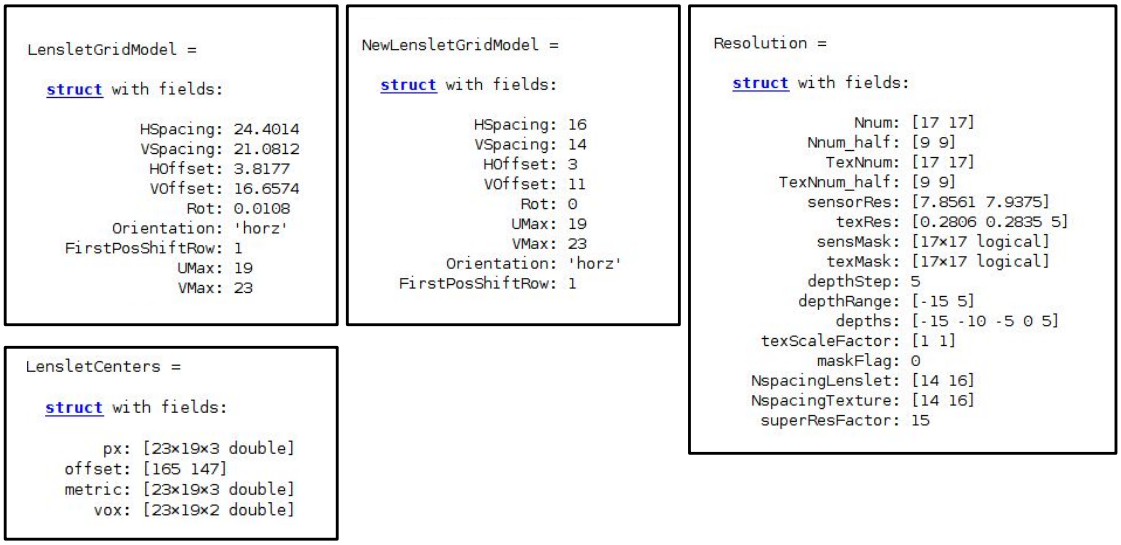

Figure 5.5: Lenslet grid and resolution related parameters.

uses a white image, together with the `Camera` structure and the user inputs to retrieve the lenslet centers and to build several data structures relevant for the reconstruction.

`DebugBuildGridModel` is a binary flag. When it is set `true`, the white image with overlaid micro-image centers is displayed for a visual check as in Fig. 5.2.

`imgSize` is only needed when a white image is not available (`WhiteImage = []`). This is the case in simulations, when a lenslet grid model is built based on the `Camera` specs and the desired sensor image size, `imgSize`. Conversely, when a white image is provided, the `imgSize` argument can be omitted as the sensor image size is just the size of the `WhiteImage`.

Finally, the `LFM_computeGeometryParameters` function returns the following data structures:

```
LensletGridModel %  derived when analyzing the raw white image.
% LensletGridModel contains information like the spacing between
% lenslet centers in pixels (HSpacing and Vspacing fields;
% which are different for hexagonal grids),
% the offset to the center of the first whole lenslet image
% in the white image (HOffset and VOffset),
% the rotation of the grid with respect to the optical axis (Rot),
% and whether odd or even rows are half diameter shifted
% in case of hexagonal grids (FirstPosShiftRow), etc.
% An example LensletGridModel for a regular grid MLA,
% with lensPitch = 127 μm and pixelPitch = 5.5 μm
% is displayed in Fig.5.5.
```

```
NewLensletGridModel % the ideal (Rot = 0) grid model created based
% on the user inputs and the LensletGridModel.
```

```
% Fig.5.5 (middle) shows a NewLensletGridModel for
% an input newSpacingPx = 17.
% The new pixel pitch is now given by lensPitch/newSpacingPx,
% such that HSpacing and VSpacing are now integer values in
% terms of the new pixel size.
```

```
Resolution % contains all the sensor and object space resolution
% related quantities. Similarly to the lenslet grid model,
% we build a TextureGridModel which describes the object space.
% The object space is interpreted as tiled lateral patches
% (areas) that are imaged exactly behind a micro-lens.
% In Sec.5.3.1 and Sec.5.4.1 we
% describe how such a representation of the object space
% makes the imaging process computationally efficient.
% The TextureGridModel depends on the LensletGridModel and the
% superResFactor introduced earlier.
```

The function

```
Resolution = LFM_computeResolution(NewLensletGridModel,...
        TextureGridModel, Camera, depthRange, depthStep)
```

builds the `Resolution` structure as shown in Fig. 5.5. `NspacingLenslet` is the distance in pixels between lenslets centers.

`Resolution` contains fields like:

```
Resolution.Nnum / Resolution.TexNnum % always odd
% to ensure a center pixels exists. They refer to the number of
% pixels/voxels behind/in front of a micro-lens, together with
% sensor/texture (object) resolution in μm,
% or Resolution.texScaleFactor which is computed as texNnum/Nnum.

Resolution.sensMask % a Nnum*Nnum binary mask computed in the function
% LFM_computePatchMask(NspacingLenslet, Camera.gridType, sensorRes,
% Camera.uRad, Nnum), such that the sensor patches behind
% the micro-lens perfectly fill the sensor plane without overlapping;
% this is particularly important for hexagonal grid MLAs, where the
% discretization of the patches is not symmetric with respect to
% the center of a micro-lens (NspacingLenslet vs. Nnum).
% Fig.5.6 (left) shows such a lenslet mask.

Resolution.texMask % analogous for the object space patches
% aligned with the micro-lenses. Ultimately, the struct also
% keeps depth related (axial resolution) input parameters.
```

Finally, the function

```
LensletCenters = LFM_computeLensCenters(NewLensletGridModel,...
        TextureGridModel, Resolution.sensorRes,
        Camera.focus, Camera.gridType)
```

builds the `LensletCenters` data structure illustrated in Fig. 5.5 (bottom):

```
LensletCenters.px % lenslet centers coordinates in pixels
LensletCenters.metric % metric lenslet centers coordinates in µm
LensletCenters.offset % the position of the central micro-lens
LensletCenters.vox % the centers of the object space patches
% LensletCenters.px has a third dimension in case of multi-focus
% MLAs (Fig.5.6 (right)) in order to store the
% lenslet type along side its center x/y coordinates.
```

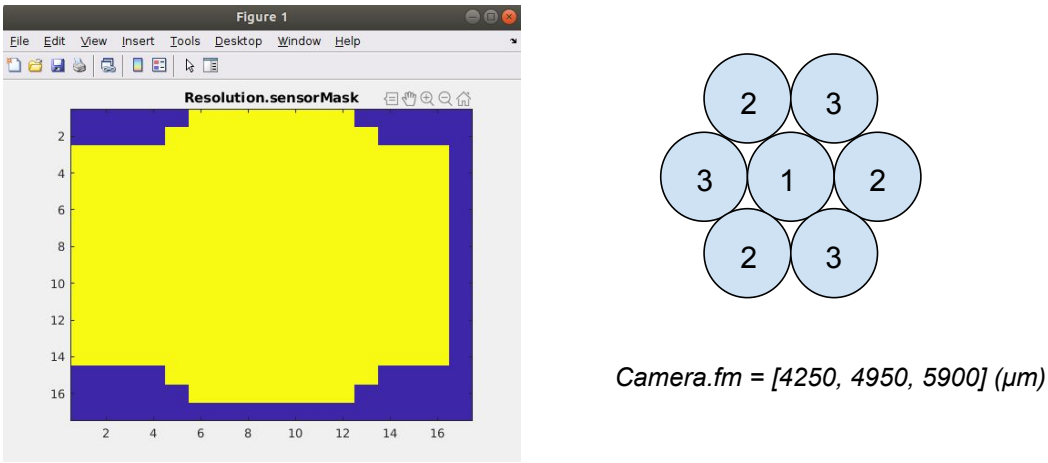

Figure 5.6: Left: Non-overlapping sensor lenslet mask. Right: Multi-focus MLA with three mixed focal length micro-lenses.

5.2.2 FLFM setup

Based on the setup description (from user inputs and configuration file; see paragraphs 5.1.4.1 and 5.1.4.2), the function

```
[Camera, LensletGridModel] = FLFM_setCameraParams(configFile,...
                                superResFactor)
```

computes extra parameters relevant for the reconstruction:

```
Camera.spacingPixels = Camera.spacingPixels * superResFactor;
% We scale the spacing between micro-lenses according
% to the super-sampling factor superResFactor
% See paragraph 5.1.4.1.

Camera.objRad % radius of the microscope objective under
% paraxial approximation.
Camera.objRad = Camera.fobj * Camera.NA;

Camera.k % wave number
Camera.k = Camera.n/Camera.WaveLength = $2*\pi$;

Camera.M % total system magnification factor
Camera.M = (Camera.fm*Camera.f1)/(Camera.f2*Camera.fobj)

Camera.fsRad % the radius of the field stop
Camera.fsRad = Camera.lensPitch/2 * Camera.f2/Camera.fm;
% see Fig.~5.7.

Camera.fovRad % the radius of the object space field of view
Camera.fovRad =  Camera.fsRad * Camera.fobj/Camera.f1;

LensletGridModel.VSpacing % vertical spacing (in pixels)
% between neighboring lenslets.
% In case of LensletGridModel.gridType == 'hex',
% LensletGridModel.VSpacing = round(sqrt(3)/2*LensletGridModel.HSpacing)
% Otherwise (for regular grid arrays)
% LensletGridModel.VSpacing and LensletGridModel.HSpacing are the same.
```

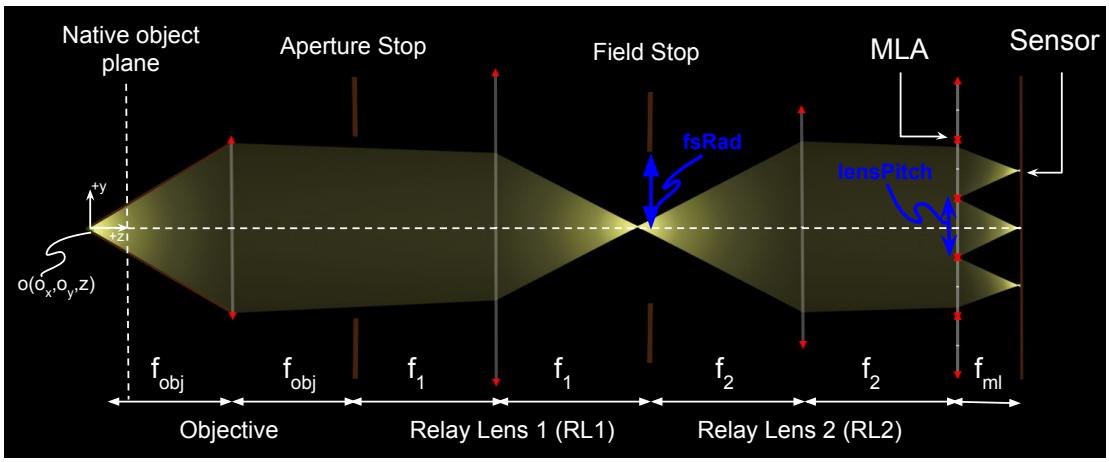

Figure 5.7: FLFM ray diagram and setup specific quantities.

The function

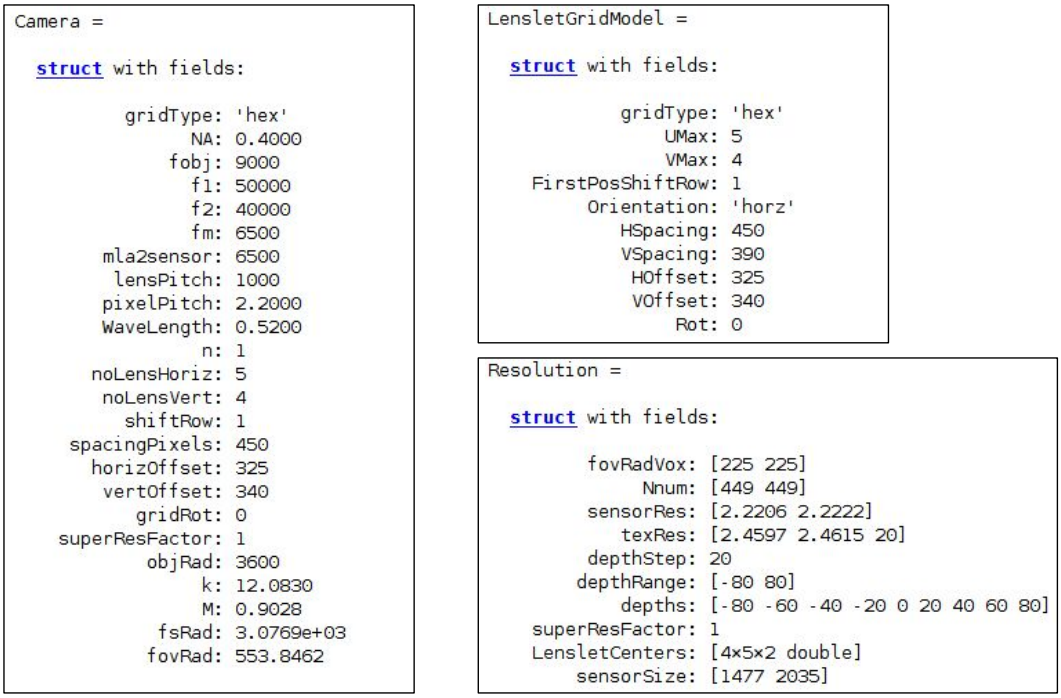

Figure 5.8: Setup, lenslet grid and resolution related parameters.

```
[LensletCenters, Resolution] = FLFM_computeGeometryParameters...
        (CalibrationImage, Camera, LensletGridModel, ...
        depthRange, depthStep)
```

uses a calibration image, together with the `Camera` and `LensletGridModel` data structures and the user inputs to retrieve the lenslet centers and to compute several resolution quantities relevant for the reconstruction. Fig. 5.8 illustrates the content of the `Camera` and `LensletGridModel` data structures for the experimental FLFM configuration used to acquire the cotton fibers image in Fig. 5.1 (c).

The `FLFM_computeGeometryParameters` function returns the following data structures:

```
Resolution % contains all the sensor and object space resolution
% related quantities, as displayed in Fig.5.8.
% computed in the function FLFM_computeResolution(...
        % LensletGridModel, Camera, depthRange, depthStep)
% It contains fields like:
        % Nnum - number of pixels behind each micro-lens,

        % senRes / texRes (object space) resolution in μm,

        % fovRadVox - radius of the object side field of view

        % sensorSize is the size of the input light field image.
```

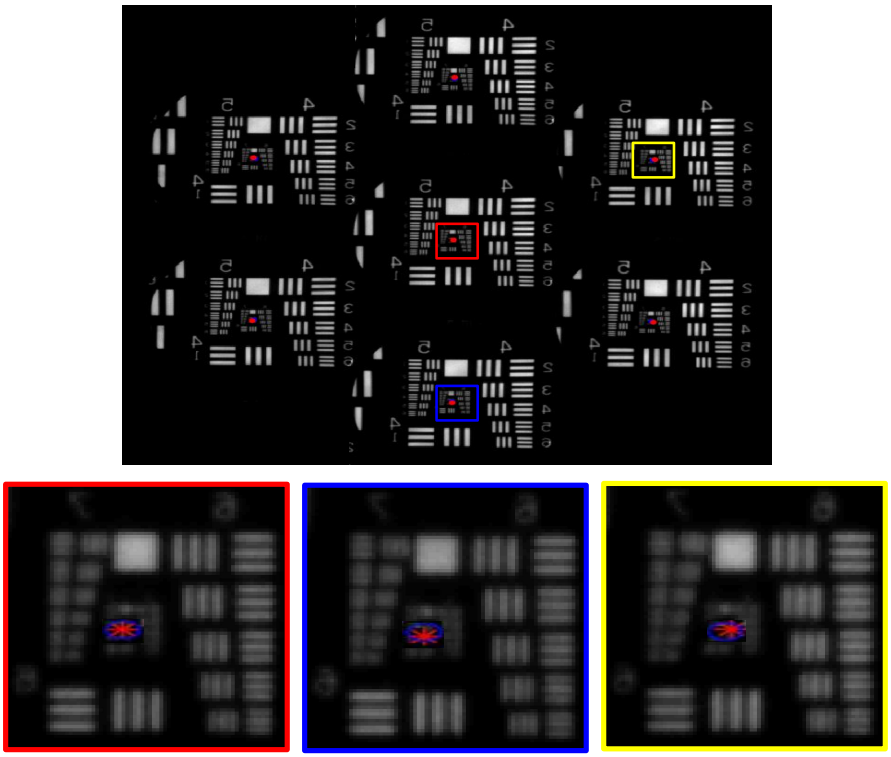

Figure 5.9: FLFM light field image of the USAF-1951 resolution target and elemental image close-ups: uniformly spaced micro-lens centers according to the `LensletGridModel` specifications (red stars) vs. corrected centers via elemental image registration (blue circles).

```
LensletCenters % the lenslet centers coordinates in pixels
% computed by the function FLFM_computeLensCenters(CalibrationImage,
                % Camera, LensletGridModel)
```

In order to detect the exact lenslet centers, in function

```
transformationsStack = ...
        FLFM_retrieveEItransformations(LensletGridModel,
        CalibrationImage)
```

we first extract the elemental images from the `CalibrationImage` using the `LensletGridModel`:

```
LF = FLFM_extractEI(LensletGridModel, CalibrationImage),
```

then pick a reference elemental image (the most central one):

```
fixed = LF(:,:,ceil(size(LF,3)/2), ceil(size(LF,4)/2)),
```

and register all the other elemental images to this reference one, in order to retrieve the translational transformation between them:

```
tform = imregtform(LF(:,:,i,j), fixed, 'translation',...
                           optimizer, metric);
```

The `transformationsStack` contains the transformations corresponding to all the elemental images.

Having computed these translational offsets, we can now find the exact centers of the microlenses by correcting the coordinates of the centers in the uniformly spaced grid estimated from the `LensletGridModel`:

```
centersUniform = LFBuildGrid(LensletGridModel, Camera.gridType)
...
LensletCenters(j,k,1) = centersUniform(j,k,1) -...
                transformationsStack{j,k}.T(3,1);
LensletCenters(j,k,2) = centersUniform(j,k,2) -...
                transformationsStack{j,k}.T(3,2);
```

Fig. 5.9 shows a light field image of the USAF-1951 resolution target and elemental image close-ups overlaid with the uniformly spaced (according to `LensletGridModel`) micro-lens centers (red stars) and the real (corrected) centers (blue circles).

5.3 Light Field Point Spread Function

5.3.1 LFPSF in conventional LFM

When passing through an optical system, an ideal source point generates a diffraction pattern at the observation plane, known as the system's point spread function (PSF). While in a conventional optical microscope, the PSF is invariant with respect to the position of the point source, in the LF microscope, the light field PSF (LFPSF) is translationally variant i.e., the diffraction pattern generated behind the MLA depends on the 3D position of the point source.

Fortunately, the repeating nature of the MLA grid makes the LFPSF to be periodic such that for source points at $s * \frac{lensPitch}{M}$ apart (s is any integer scalar factor), their response on the sensor (LFPSFs) are identical up to a $s * lensPitch$ translation.

When we represent the discrete forward imaging model as:

$$i = H * t, \tag{5.1}$$

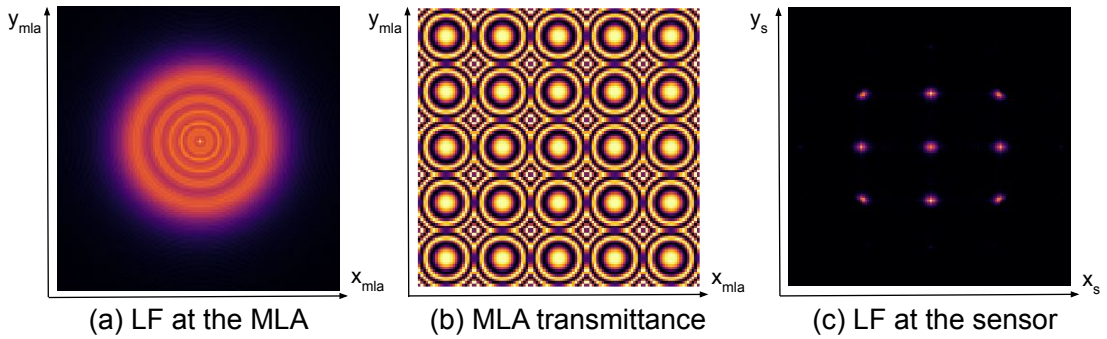

Figure 5.10: Step-by-step LF point spread function computation.

the operator H represents the discrete LFPSF, i the sensor image (LF measurements) and t the discretized imaged 3D object.

Due to the periodicity of the LFPSF, the computational burden of computing the columns of matrix H reduces dramatically as we only compute and store the LFPSF for a limited number (`Resolution.TexNnum*Resolution.TexNnum`) of discrete source points per axial depth; we call these the forward projection patterns. Consequently, H can be efficiently applied (forward projection) as a series of convolutions (each PSF pattern as kernel over corresponding source points) at every object depth. This procedure is described in Sec. 5.4.1.

The function

```
[H, Ht] = LFM_computeLFMatrixOperators(Camera, Resolution,...
                          LensletCenters)
```

uses the data structures introduced in Sec. 5.2.1 to pre-compute the forward (`H`) and backward (`Ht`) projection patterns in several steps:

- The function

  ```
  PSFsize = LFM_computePSFsize(maxDepth, Camera)
  ```

  first computes the maximum blur size in pixels (area of the wave-front distribution) at the MLA plane in order to know the needed size of the `H, Ht` matrix containers.

  `maxDepth` is that depth among `Resolution.depthRange` which is further away from the front focal point of the microscope objective, such that it generates the largest blur in extent. Once we know the maximum size of the LFPSF for the chosen axial range, using the `Resolution.sensorRes` we define the sensor plane coordinates (in μm), `Resolution.xspace, Resolution.yspace` as well as local lenslet coordinates (relative to a lenslet center), `Resolution.xMLspace, Resolution.yMLspace`.

- The function

```
psfWaveStack = LFM_calcPSFAllDepths(Camera, Resolution)
```

computes the wave-front distribution at the MLA plane generated by point source on the optical axis at every depth in `Resolution.depths`. This intermediary PSF at the MLA plane is shift invariant and so it is enough to compute the response for a single source point, for simplicity, a point on the optical axis. In order to optimize the implementation and computation time, we exploit the nature of the wave-based PSF:

- Due to the circular symmetry of the PSF, we only compute one quarter of the 2D distribution and then replicate it for the full range.
- The PSF for source points at equal distance from the focus point of the objective are complex conjugates. In practice, in general, we are interested in reconstructing axial ranges symmetrically around the native object plane, e.g. $[-50, 50]\mu m$; we then only effectively compute the responses at the MLA for half of the range and use their complex conjugates for the rest.

The simulated PSF at the MLA plane for a point at depth $\Delta z = -20$ is shown in Fig. 5.10 (a). For these simulations, we emulated a LFM setup as described in the `LFConfig.yaml` of Fig. 5.1 (a).

- Once we have the `psfWaveStack` at the MLA plane, the function

```
[H, Ht] = LFM_computePatternsSingleWaves (psfWaveStack, Camera, ...
                Resolution, tolLFpsf)
```

computes the forward and back-projection patterns for LFM setups with single focus MLA.

Similarly, the function

```
[H, Ht] = LFM_computePatternsMultiWaves(psfWaveStack, Camera,...
                Resolution, tolLFpsf)
```

adapts the functionality for multi-focus (`Camera.focus = 'multi'`) MLA setups as depicted in Fig. 5.6 (right). Over the remaining of this section we will point out to the multi-focus specific functionality when relevant.

The forward/backward light patterns computation is implemented in several steps:

- The function

```
ulensPattern = LFM_ulensTransmittance(Camera, Resolution)
```

computes the 2D transmittance function for one micro-lens and

```
MLARRAY = LFM_mlaTransmittance (Camera, Resolution,...
                ulensPattern)
```

replicates the `ulensPattern` one `lensPitch` apart for the size of the MLA. The simulated 2D MLA transmittance function is depicted in Fig. 5.10 (b).

– The function

```
H = LFM_computeForwardPatternsWaves(psfWaveStack,...
                MLARRAY, Camera, Resolution)
```

computes the forward projection for every point inside a patch aligned with the central (w.r.t the optical axis) micro-lens. The size of this patch is chosen such that its image on the sensor is formed exactly behind one micro-lens. It is then sufficient to compute the LFPSFs for these points and then apply them in a shifted matter for any object size in front of the microscope.

In case of regular grid MLAs, it is sufficient to compute the LFPSF for only one quarter of the object space patch

```
Resolution.TexNnum_half * Resolution.TexNnum_half *
                length(Resolution.depths)
```

due to symmetry, and then use shift rotated versions of these for the rest of the discrete points in the patch. Unfortunately, such optimization is not possible in case of hexagonal grid MLAs, as the object space cannot be split into symmetrically (with respect to the center point of a patch) discretized patches; this is due to the integer rounding of the half `lenspitch` displacement of the micro-lens every other row in the hex MLA. This discrimination gives rise to the `Camera.range` flag introduced in Sec. 5.2.1:

```
Camera.range = 'quarter' % for regular grid MLA setups;
Camera.range = 'full' % for hexagonal grid MLA setups.
```

Coming back to computing the forward patterns, for each discrete point in the object space range (full or quarter patch) described above, we laterally shift the previously compute 2D PSF (at the MLA plane) corresponding to the axial position of the point (from `psfWaveStack`) to the xy position of the current point, using the function

```
newImg = imShift2(Img, ShiftX, SHiftY)
```

Then the shifted PSF (`psfSHIFT`) is passed through the MLA by applying the MLA transmittance:

```
psfMLA = psfSHIFT.*MLARRAY;
```

The response is then propagated to the sensor using the function:

```
LFpsfAtSensor = prop2Sensor(psfMLA, sensorRes,...
                Camera.mla2sensor, Camera.WaveLength, 0);
```

which implements the Rayleigh-Sommerfeld diffraction.

Finally, the 2D response patterns are shifted back and the results are stored in sparse format:

```
H(aa_tex, bb_tex, c) = sparse(abs(double(LFpsf).^2));
```

Here, `aa_tex, bb_tex` represent the local lateral object patch coordinates and `c` indexes the axial coordinate, `Resolution.depths(c)`:

```
aa_tex = 1..Resolution.TexNnum,

bb_tex = 1..Resolution.TexNnum,

c = 1..length(Resolution.depths).
```

In case of the multi-focus LFM setup, we compute three (as many as the number of different micro-lens focal length available in the MLA) different sets of forward patterns. In order to do so, we simulate three different 2D MLA transmittance functions, each with one of the three micro-lens in the center (w.r.t the optical axis of the system), by shifting around the available focal lengths, e.g.:

```
CameraShift.fm = circshift(Camera.fm, -1);
ulensPattern = LFM_ulensTransmittance(CameraShift,...
               Resolution);
MLARRAY = LFM_mlaTransmittance(CameraShift,...
               Resolution, ulensPattern);
```

Fig. 5.10 (c) shows a simulated forward pattern for source a point on the optical axis (`(aa_tex, bb_tex) = (Resolution.TexNnum_half, Resolution.TexNnum_half)` at $-20\mu m$.

– The function

```
H = ignoreSmallVals(H, tolLFpsf)
```

is a convenience function which first clamps the values of `H` smaller than `tolLFpsf` in order to speed up the computations (see convolution in Sec. 5.4.1). Then the individual 2D LFPSFs, `H(aa,bb,c)` are normalized to `[0,1]` range.

– The function

```
Ht = LFM_computeBackwardPatterns(H, Resolution,...
                range, lensOrder)
```

computes the backward light transport patterns, for every discrete point on the sensor plane, behind a micro-lens. Analogous to the forward pass, it is sufficient to compute the patterns for only a limited set (behind the central micro-lens) of points (`Resolution.Nnum * Resolution.Nnum`) as the entire sensor plane contains only shifted version of these.

The `lensOrder` argument is left empty (`[]`) for single-focus MLA setups, and it is only used in case of multi-focus setups when we compute three different sets of back-projection patterns, one for each micro-lens type:

```
lensOrder = [1,2,3];
Ht1 = LFM_computeBackwardPatterns(H, Resolution,...
                Camera.range, lensOrder);
Ht2 = LFM_computeBackwardPatterns(H, Resolution,...
                Camera.range, circshift(lensOrder, -1));
Ht3 = LFM_computeBackwardPatterns(H, Resolution,...
                Camera.range, circshift(lensOrder, -2));
```

The backward light propagation represents the inverse process of the forward projection, and it is thus a mapping from the 2D sensor space to the 3D object space; every backward pattern is stored in a 3D container:

```
Ht = cell(coordsRange(1), coordsRange(2), nDepths);
% coordsRange = Resolution.Nnum when Camera.range = 'full'
% coordsRange = Resolution.Nnum_half when
                % Camera.range = 'quarter'
```

In order to compute the backward projection patterns, we iterate through every pixel behind the central micro-lens and compute its 3D object space response (which part -and to what extent- of the 3D object space affects the current pixel).

The function

```
tempback = LFM_backwardProjectSinglePoint(H, Resolution,...
        imgSize, texSize, currentPixel,...
        lensletCenters, range, lensOrder);
```

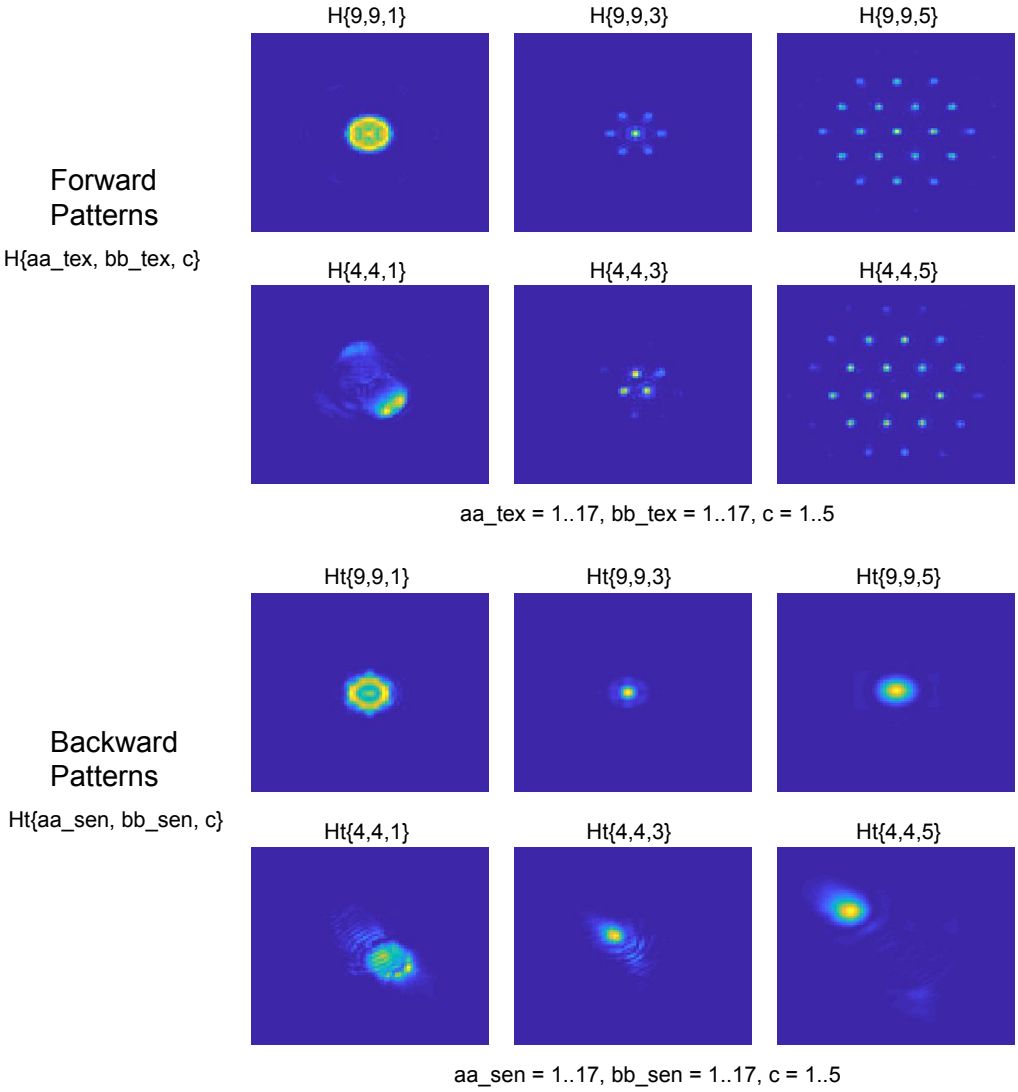

Figure 5.11: Example forward and backward light transport patterns for a hexagonal grid MLA system.

returns the back-projection response for one activated pixel, `currentPixel`. The idea to obtain the back-projection pattern for an active pixel is to forward project the whole (an area as wide as it can be captured) 3D space in front of the microscope and acknowledge which object space points were seen by the active pixel and to what extent (intensity of the LFPSF); then this is the object space response to our active sensor pixel (the back-projection pattern).

In practice, in order to forward project the 3D object space, we convolve the object with the LFPSF, `H`. However, since the LFPSF is different for different source point positions, the object space needs to be split into discrete sets of points which give the same (only translated) sensor response and apply each `H(aa_tex, bb_tex, c)` to the corresponding points and store the sensor response back into the volume at the same locations. This process is equivalent to convolving each rotated forward pattern kernel with the sensor image with a single active pixel and grabbing the

result of this convolution only at the relevant (which generate the forward pattern in discussion) coordinates in the volume:

```
H_rot = imrotate(H(aa_tex,bb_tex,cc), 180);
tempSlice = sconv2singlePointFlip(imgSize,...
        currentPixel, H_rot, flipX, flipY, 'same');
% Instead of a 2D convolution between H_rot and the sensor
% image, we have implemented a computationally efficient
% single point convolution, as the sensor image has only
% one active pixel.

% flipX, flipY are flags used when Camera.range = 'quarter',
% when we only compute forward  projection patterns
% for one quarter of the patch in front of the central
% micro-lens, and thus for the rest of the points
% the LFPSFs are flipped versions of the available ones.

sliceCurrentDepth(indicesTex) = sliceCurrentDepth(indicesTex)
                        + tempSlice(indicesSen);
% indicesTex and indicesSen are the relevant
% (associated with H(aa_tex,bb_tex,cc))
% volume and sensor coordinates.

% indicesTex and indicesSen are different
% when we reconstruct at a different lateral resolution
% than the sensor resolution.
% For a comprehensive understanding,
% see the backwardProjectSinglePoint.m file.
```

We repeat this for all the object depths, as one sensor pixel back-projects to the entire axial range.

Finally, we shift the patterns back (needed for convolution, see Sec. 5.4.1) and store them:

```
Ht(aa_sensor,bb_sensor,:) = tempbackShift;
% aa_sensor = 1..coordsRange(1),
% bb_sensor = 1..coordsRange(2).
```

Fig. 5.11 shows example forward and backward light transport patterns for a defocused LFM setup with hexagonal grid MLA and a desired reconstruction with axial resolution `Resolution.depths = [-15, -10, -5, 0, 5]` μm, and `Resolution.TexNnum = Resolution.Nnum = 17`. We show forward patterns for source points on the optical axis (Fig. 5.11 (top row)), as well as off-axis ones (Fig. 5.11 (second row)), for the `-15, -5, 5` μm depth planes. The displayed backward patterns correspond to the central pixel behind a micro-lens (Fig. 5.11 (third row)), as well as an offset pixel (Fig. 5.11 (bottom row)).

The derivation of the wave-based LFPSF implemented in this framework is described in detail in [68].

5.3.2 LFPSF in Fourier LFM

When passing through an optical system, an ideal source point generates a diffraction pattern at the observation plane, known as the system's point spread function (PSF). Similarly to a conventional wide field microscope, the light field PSF (LFPSF) of the Fourier LFM is translationally invariant for a fixed axial position, due to the strategic placement of the MLA at the back aperture stop of the objective. Conveniently, this allows us to describe the imaging process in FLFM as a 2D convolution (at each axial slice) of the object with the LFPSF. This process is described in Sec. 5.4.2.

When we represent the discrete forward imaging model as:

$$i = H * t, \tag{5.2}$$

H represents the discrete LFPSF (a stack of the 2D PSFs for each object space axial position in the object), i the sensor image (LF measurements) and t the discretized imaged object. $*$ is then the slice-by-slice 2D convolution operator.

The function

```
[H, Ht] = FLFM_computeLFMatrixOperators(Camera, Resolution)
```

uses the data structures introduced in Sec. 5.2.2 to pre-compute the LFPSF (`H`) and its transpose (`Ht`) in several steps:

```
psfStack = FLFM_calcPSFAllDepths(Camera, Resolution)
% computes the wave-front distribution incident on the micro-lens
% array (MLA) plane generated by a point source
% on the optical axis at every depth in Resolution.depths.

[U1, LU1] = FLFM_lensProp(U0, LU0,...
                Camera.WaveLength, Camera.fobj)
% implements the Fourier property of a lens (under paraxial context)
% to generate the field at the back focal plane;
% see AS plane in Fig.5.7
% of the objective as a scaled Fourier transform of the field
% at the front focal plane.

% The field at the MLA plane is then just a scaled version
% of the field at the AS plane, by the relay magnification factor,
% Mrelay = Camera.f2/Camera.f1.
```

```
% For implementation details of these functions,
% see the corresponding Matlab functions.
```

Once we have the psfStack at the MLA plane,

```
[H, Ht] = FLFM_computeLFPSF(psfStack, Camera,...
                            Resolution, tolLFpsf)
```

computes the forward and backward light propagation models of the FLFM setup in several steps:

```
% computes the 2D transmittance function for one micro-lens
ulensPattern = FLFM_ulensTransmittance(Camera, Resolution);

% replicates the ulensPattern
% one lensPitch apart for the size of the MLA.
MLARRAY = FLFM_mlaTransmittance (Resolution, ulensPattern);

% each of the 2D PSFs in the psfSTACK is passed through the
% MLA by applying the MLA transmittance
psfREF = psfSTACK(:,:,c);
psfMLA = psfSHIFT.*MLARRAY;

% Rayleigh-Sommerfeld diffraction transfer function
% propagates the response to the sensor
LFpsfSensor = prop2Sensor(psfMLA, sensorRes, Camera.mla2sensor,...
                Camera.WaveLength, 0);

% store the 2D response patterns in the H container
H(i,j,c) = sparse(abs(double(LFpsfSensor).^2))

% clamp the values of H smaller than tolLFpsf
% in order to speed up the computations;
% see convolution in Sec.5.4.2
H = ignoreSmallVals(H, tolLFpsf)

% H(1,1,c) are also normalized to the [0, 1] range.

% Ht stores the backward light transport patterns,
% which are the rotated LFPSF kernels
Ht(i,j,c) = imrotate(H(i,j,c), 180)

% makes sure the transpose LFPSF adds up to 1
% for each source axial position.
% This step ensures that when applying the inverse mapping (H_t * i),
% the energy in the reconstruction is kept through the
```

```
% Richardson-Lucy iterative deconvolution scheme.
Ht = normalizeHt(Ht)
```

The derivation of the wave-based LFPSF implemented in this framework is described in detail in [133].

5.4 Forward/Backward projection

5.4.1 Projection operators in conventional LFM

The function

```
Projection = LFM_forwardProject(H, realSpace, LensletCenters, ...
        Resolution, imgSize, Camera.range);
```

implements the light field forward projection operator. It applies the pre-computed (see Sec. 5.3.1) forward patterns, `H` to a given 3D volume, `realSpace` and returns a light field image, `Projection` of size `imgSize`.

In order to apply the patterns in `H` to the object, `realSpace`, we pre-store the object voxels with coordinates `(aa_tex,bb_tex)` relative to the '`Resolution.TexNnum*Resolution.TexNnum`' object space repetition patches (imaged behind exactly one micro-lens extent), into `indicesTex(aa_tex,bb_tex)`. The corresponding sensor image coordinates are pre-stored into `indicesImg(aa_tex,bb_tex)`.

Once we sort out which object coordinates generate which pattern, for every reconstruction depth, `cc = 1..length(Resolution.depths)`, we grab, at a time, only those parts of the object corresponding to current `indicesTex(aa_tex,bb_tex)` and apply the associated `H(aa_tex,bb_tex,cc)`:

```
% grab object slice (current depth) to be forward projected
realspaceCurrentDepth = realSpace(:,:,cc);

% from the current slice, keep only indicesTex(aa_tex,bb_tex)
tempspace(indicesImg(aa_tex,bb_tex)) =...
        realspaceCurrentDepth(indicesTex(aa_tex,bb_tex));

% convolve tempspace with the corresponding pattern
Hs = H(aa_tex,bb_tex, cc);
conv2(tempspace, Hs, 'same');

% finally, the intermediate projection are accumulated
Projection = Projection + projectedPattern;
```

The non-zero values in `H(aa_tex,bb_tex, cc)` (effective sparse kernel size) directly affect the computation time. The further away a source point is from the native object plane (NOP, depicted in blue in Fig. 5.4) of the LFM, the larger the LFPSF size on the sensor. This means object depths further away from the NOP require are computationally more expensive to forward- / backward-project.

The above procedure is executed in parallel on workers using Matlab's `parallel pool` functionality, for all `aa_tex = 1..Resolution.TexNnum, bb_tex = 1..Resolution.TexNnum`.

The function

```
BackProjection = LFM_backwardProject(Ht, projection,...
                 lensCenters, Resolution, texSize, range);
```

implements the light field backward projection operator. It applies the pre-computed (see Sec. 5.3.1) backward patterns, `Ht` to a given light field image, `projection` and returns 3D volume, `BackProjection` of size `texSize`.

In order to tapply he patterns in `Ht` to the light field image, `projection`, the `LFM_backwardProject` function implements selective sparse convolutions in an analogous manner to the `LFM_forwardProject` function described above.

`imgSize` and `texSize` are pre-computed container sizes for the returned light field image in case of the `forwardProjectACC` function and 3D object in case of the `backwardProjectACC` function, respectively. The `imgSize` and `texSize` sizes are different when we reconstruct an object at a lateral resolution different from the sensor resolution. Then `texSize` is retrieved as (see `main.m` script):

```
imgSize = size(correctedLensletImage);
imgSize = imgSize + (1-mod(imgSize,2)); % ensure odd size
texSize = ceil(imgSize.*Resolution.texScaleFactor);
texSize = texSize + (1-mod(texSize,2)); % ensure odd size
```

Both `LFM_forwardProject` and `LFM_backwardProject` functions apply to single focus MLA setups (`Camera.focus = 'single'`). In case of multi-focus setups (`Camera.focus = 'multi'`), functions `LFM_forwardProjectMultiFocus` and `LFM_backwardProjectMultiFocus` expand and adapt the functionality above in a straightforward manner. For details on the implementation of the projection operators, see the corresponding Matlab files.

5.4.2 Projection operators in FLFM

The function

```
Projection = FLFM_forwardProject(H, realSpace);
```

implements the light field forward projection operator. It applies the pre-computed (see Sec. 5.3.2) forward light model, `H` to a given 3D volume, `realSpace` and returns a light field image, `Projection`.

In order to project the object, `realSpace` using the LFPSF in `H`, we perform 2D slice-by-slice convolutions at every depth and cumulate the responses:

```
Projection = Projection + conv2(realSpace(:,:,k),...
                         full(H(i,j,k)),'same');
```

The function

```
BackProjection = FLFM_backwardProject(Ht, projection)
```

implements the light field backward projection operator. It applies the pre-computed (see Sec. 5.3.2) backward patterns, `Ht` to a given light field image, `projection` and returns a 3D volume, `BackProjection`.

In order to apply the patterns in `Ht` to the light field image, `projection`, the `LFM_backwardProject` function implements slice-by-slice convolutions in an analogous manner to the `FLFM_forwardProject` function described above:

```
BackProjection(:,:,k) = BackProjection(:,:,k) + conv2(projection,...
                         full(Ht(i,j,k)),'same');
```

For details on the implementation of the projection operators, see the corresponding Matlab files.

Part V

How it all started

Chapter 6

NeubTracker

This Chapter is dedicated to *NeuBtracker* - the project that marks my debut in computational imaging research. Taking part in the development of this framework definitely influenced my subsequent research work; both in terms of methods and vision.

The work presented here was published as part of the article:

- P. Symvoulidis, A. Lauri, A. Stefanoiu, M. Cappetta, S. Schneider, H. Jia, A. Stelzl, M. Koch, C. Cruz Perez, A. Myklatun, S. Renninger, A. Chmyrov, T. Lasser, W., V. Ntziachristos, and G. G. Westmeyer. "NeuBtracker - Imaging neurobehavioral dynamics in freely behaving fish." *Nature Methods*, 14, pp. 1079-1082, 2017. DOI: 10.1038/nmeth.4459.

NeuBtracker is the product of endless work and successful collaboration between several research entities [1].

[1] Institute of Biological and Medical Imaging, Helmholtz Zentrum München, Munich, Germany;
Institute of Developmental Genetics, Helmholtz Zentrum Müunchen, Munich, Germany;
Department of Nuclear Medicine, Technical University of Munich, Munich, Germany;
Computer Aided Medical Procedures, Technical University of Munich, Munich, Germany;
Institute of Neuroscience, Technical University of Munich, Munich, Germany;
Champalimaud Centre for the Unknown, Lisbon, Portugal;
Chair for Biological Imaging, Technical University of Munich, Munich, Germany.

6.1 Motivation

An important goal in neuroscientific research is to record spatiotemporal patterns of brain activity in free, naturally-behaving vertebrate animals in order to reveal neuronal correlates of unperturbed perception and unrestrained behavior. However, technical challenges usually necessitate a combination of physical restraint, pharmacological sedation, and paralysis of the animal to enable neuroimaging. Whereas sophisticated head-mounted optical imaging devices have been developed for rodents to achieve real-time neuroimaging of selected cell populations [134], their field of view (FOV) is usually much smaller than what could be achieved in transparent vertebrate reporter fish.

Several advances in genetically encoded fluorescent sensors [135] and fast optical imaging instrumentation have established the zebrafish (Danio rerio) as a powerful genetic vertebrate model organism for imaging-based neuroscience [136]. Virtual reality approaches in restrained zebrafish larvae [137, 138], fluorescent imaging of unrestrained fish within a stationary FOV [139], or bioluminescent point measurements in free larvae [140] have been reported. There is also considerable interest in quantifying the versatile behavioral repertoire of zebrafish [141, 142] in the context of high-throughput pharmacological screens [143].

NeuBtracker [144] is an open-source modular platform for neuro-behavioral imaging and manipulation that enables simultaneous and non-invasive monitoring of brain activity and behavioral parameters in unrestrained, freely swimming zebrafish larvae.

6.2 The optical tracking system

The NeuBtracker platform is able to track the head and/or body of freely swimming zebrafish larvae to obtain fluorescence images with up to 15 fold magnification. Fig. 6.1 gives an overview of the main features and capabilities of the tracking microscope. NeuBtracker has two imaging channels: one is static to observe the behavior of the fish and locate its position, the other one tracks the freely swimming larva to provide magnified fluorescent images. Tracking of the fish is controlled by a custom-written acquisition software that receives the 1× image from an IR-sensitive camera as input, locates the fish's head, and moves galvanometric mirrors to the position that keeps the FOV of the fluorescent camera on the fish.

For fluorescence excitation a LED centered at 460 nm was used to provide homogeneous illumination across the whole arena rather than guiding the excitation light through the tracking mirrors, which might result in confounding visual or thermal stimuli during imaging. Magnification is obtained either by using lenses with a fixed focal length ("MicroFixed" configuration) or a zoom lens ("MacroZoom" configuration), which can achieve a resolution of up to 150 line pairs per mm (lp/mm) for FOVs ranging from the whole body of a larva to zoom-ins on only the larval brain. Furthermore, an electrically tunable lens (ETL) inserted in the optical path enables fast refocusing with submicrometer steps up to a focal length of 10 mm.

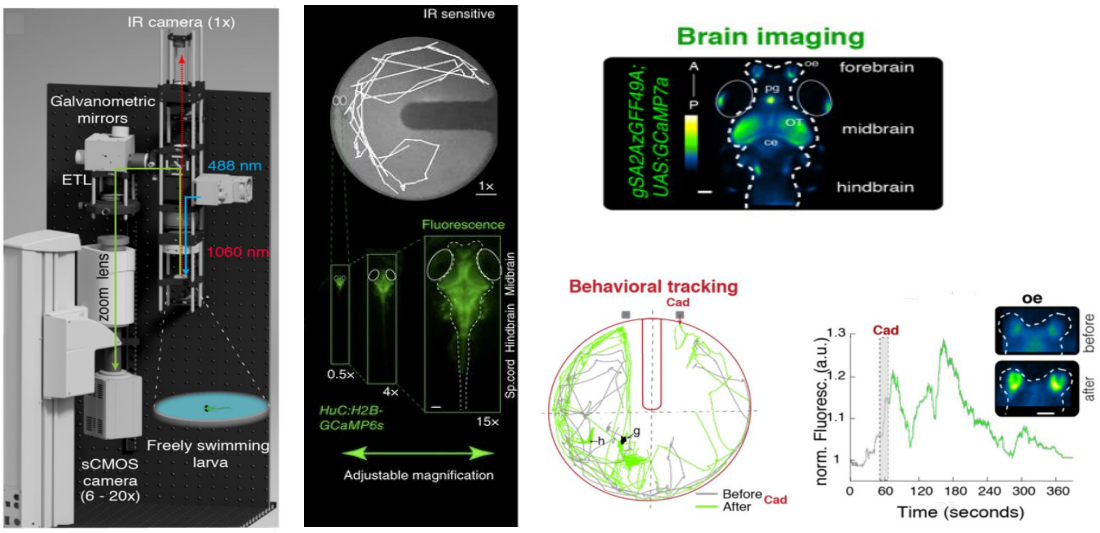

Figure 6.1: *Left*: Rendering of the system showing the infrared (IR) channel (red arrow) for transillumination imaging as well as the fluorescence detection path (blue/green) that can be scanned across the arena with adjustable magnification and focusing via an electrically tunable lens (ETL). *Middle:* Example of a swimming trajectory as well as fluorescent images obtained at different magnifications either capturing the whole arena 0.5×, covering the entire body 4× or just the brain 15× of a fish larva. *Right:* Neurobehavioral imaging and tracking data from a swimming zebrafish larva during an experiment where cadaverine odour was injected in the water.

6.3 Image processing

6.3.1 Tracking

The online tracking procedures detects the center of mass of the fish from the IR channel. Once the coordinates are determined, they are transformed (based on a fixed transformation matrix built during a calibration step) into a pair of voltage values. If the center of mass exceeds a predefined distance from the center of FOV, these voltage command signals are sent via an IO card to the galvanometric mirrors that move the FOV of the fluorescent channel. Manual overrides of the automated tracking are possible by either defining the desired coordinates of the FOV via a mouse click or by moving the FOV with a joystic. The GUI illustrated in Fig. 6.2 intermediates the acquision control.

6.3.2 Autofocus

The electrically focus-tunable lens (ETL) can be manually controlled from the acquisition GUI of system for optimizing the focus for each experimental run. It can also be tuned automatically via an autofocus routine to enable, e.g., refocusing for long-term recordings or screens. The routine operates by computing a focus measure of each acquired frame. If this measure is lower than a threshold, additional focus measures are obtained from images acquired by varying the

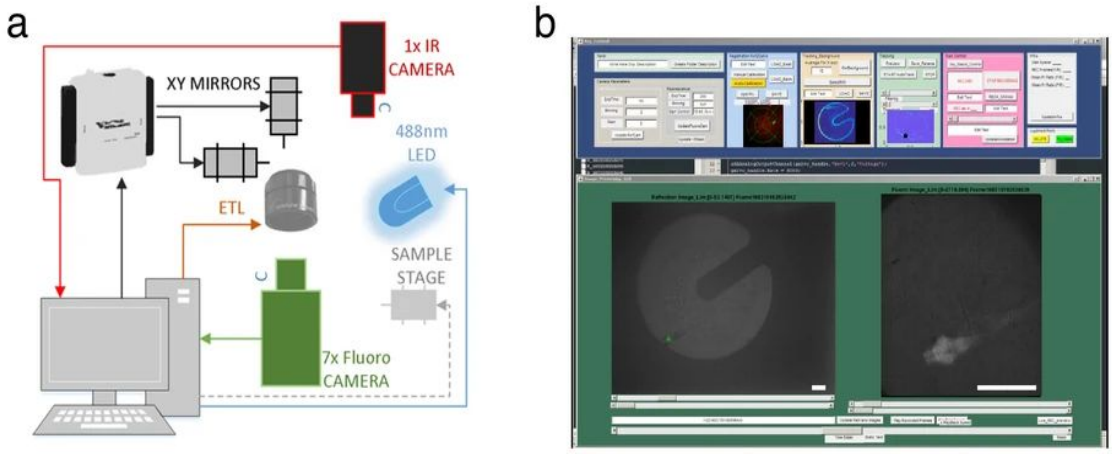

Figure 6.2: *(a)* Simplified schematic showing the main connections to and from the console running the control software. *(b)* Screenshot acquired during one of the acquisitions, showing the GUI of the control software displaying both of the imaging channels (left: 1x behavioral tracking, right: magnified real-time view of the fluorescent imaging).

focal length of the ETL in both directions. A 2nd-degree polynomial is fitted to the obtained focus measures vs. the focal lengths that were acquired. If the residuals of the fit are small, the ETL is set to the focal length that resulted in the largest focus measure. If the residuals are large, the maximum of the fitted curve is used to set the ETL to the corresponding focal length. The autofocus rutine is illustrated in Fig. 6.3.

6.3.3 Data post-processing

Each single output data set of NeuBtracker is composed of two collections of images: one acquired by the fluorescence channel and one obtained from the 1× channel. A postprocessing algorithm coregisters the fluorescence acquired images to enable analysis of the spatio-temporal patterns of calcium fluxes. The processing pipeline is illustrated in Fig. 6.4.

An automated quality inspection of the fluorescence images is performed in two stages. In the first stage, a fast feature detection algorithm (SURF) is run on each single frame. The number of features detected is the first parameter considered in order to confirm the presence of the brain in the FOV in each frame. Any frame with less than five features detected is censored from subsequent analyses. In the second stage, the individual frames are grouped into batches. In each batch, an image with a high number of features is selected as a key frame, which is a good indicator for the presence of the brain in the FOV. All other frames in the batch are matched to the key frame using a similarity transform. Frames that yield no rigid match to the key frame are censored, as well as frames that have a similarity transform with nonunit scaling. The transformed frames in the batches are used as initialization for the subsequent registration routine.

To initialize the fine image registration process, the key frame in each batch and the estimated

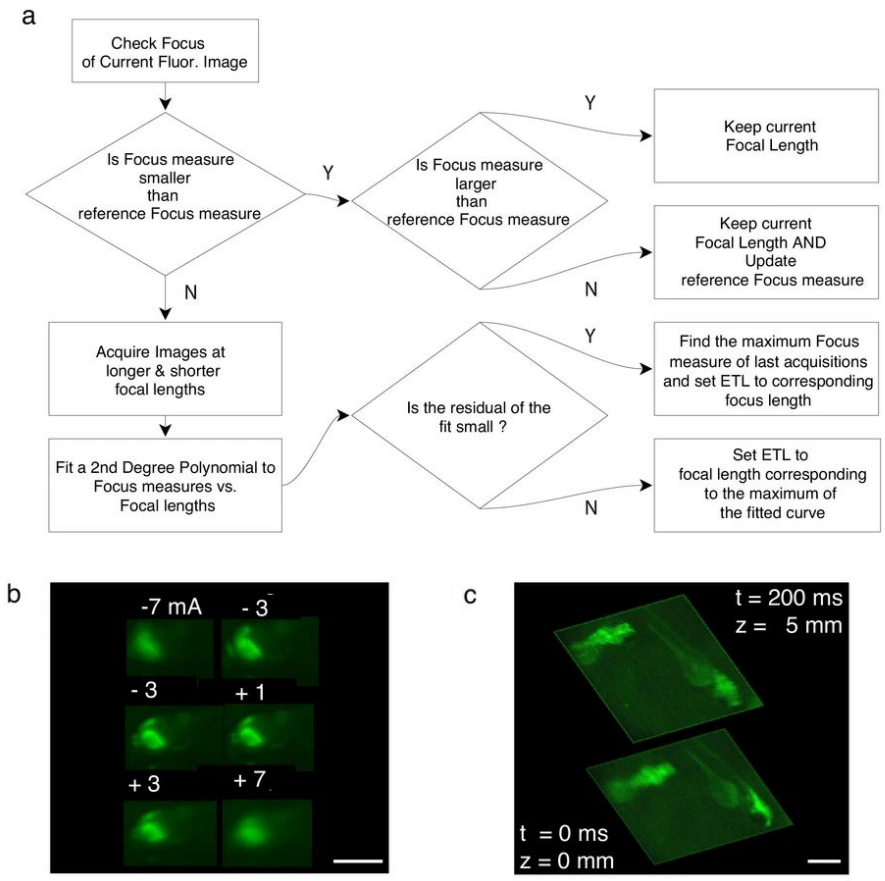

Figure 6.3: *(a)* The autofocus routine runs during the acquisition in order to keep the fish in focus as it swims at different depths. *(b)* Fine-focusing of the ETL (m? control currents correspond to submicron steps in the focal length) on a larval brain. *(c)* The fish swimming in different depths in a 10 mm deep arena were brought in focus. The bottom frame focuses on the right fish located close to the surface (fish is tilted). The top frame was acquired 200 ms later and focused on the left fish swimming at a greater depth.

transform computed from the feature matching are used. The frames in each batch are then cropped around the estimated position of the fish brain to reduce the file size. The registration then proceeds in three steps. First, for each batch the frames are registered to the key frame using an intensity-based registration algorithm maximizing the mutual information similarity measure, applying a rigid transformation model. In a second step, a global template image is selected from the key frames. All frames of the image series are then rigidly registered to the global template by applying the same registration algorithm again, propagating the previous transformations. As a final step for fine tuning the registration result, all frames are again registered with respect to the global template. This is performed by optimizing the crosscorrelation of the images in the Fourier domain and applying a transformation model using only translations.

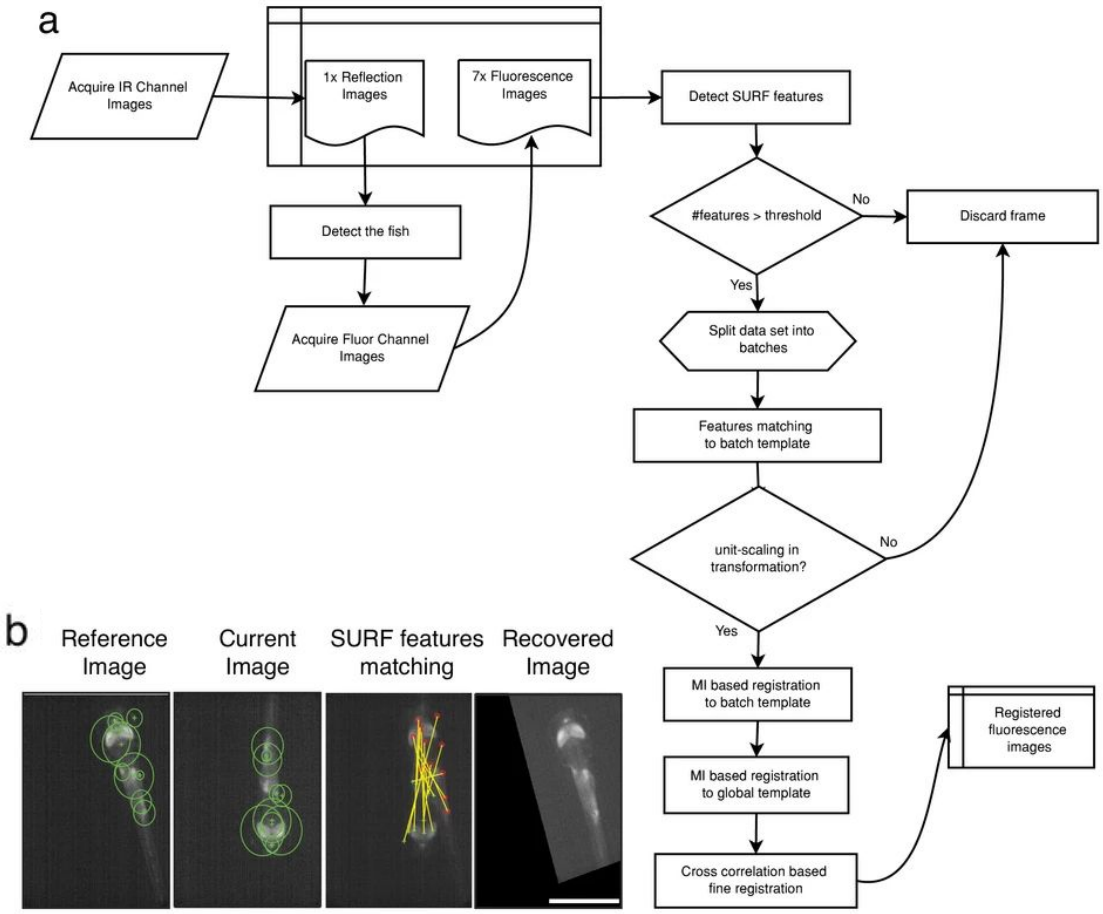

Figure 6.4: *(a)* Flowchart of the data acquisition and processing pipeline with *(b)* examples from the feature matching of the SURF registration.

6.4 Results

This section selectively presents several experiments showcasing the potential of the tracking microscope. We used NeuBtracker with a FOVs of 15×15 mm and a working distance between objective and sample of ≈ 10 cm. To enable long-term recordings and controlled application of substances (e.g. odors), we designed custom-made circular arenas of 9 mm in diameter that contain two symmetric holes $\leq 10\mu$m, connected to two $\approx 25\mu$L compartments into which substances can be directly pipetted via external injection ports.

Single zebrafish larvae were left free to explore a circular arena (9 mm) on NeuBtracker (containing 100μL of fish water). After a few seconds of acclimation, an automated tracker control routine was initiated that switched the 488 nm LED illumination OFF and ON (5 seconds OFF and 20 seconds ON as showen in Fig. 6.5 for several cycles to test for responses of the pineal complex known to contain photoreceptors. The dynamics of neuronal activation in response to the OFF-ON were studied within each subject. For validation experiments, a custom-built single-plane illumination (SPIM) setup was used, which combines both a fast galvo-scanner light sheet [145] and an ETL [146] for the z-scanning of the optical path. The larvae were em-

bedded in 1% low melting agarose in a custom-made chamber and illuminated by a light sheet generated by a 488 nm laser. One plane was imaged at 10 Hz. Activation of the pineal complex was confirmed by immunodetection of phosphorylated ERK [147] on a different group of larvae of the same age and strain using the same dark-light cycles protocol as was used for the NeuBtracker.

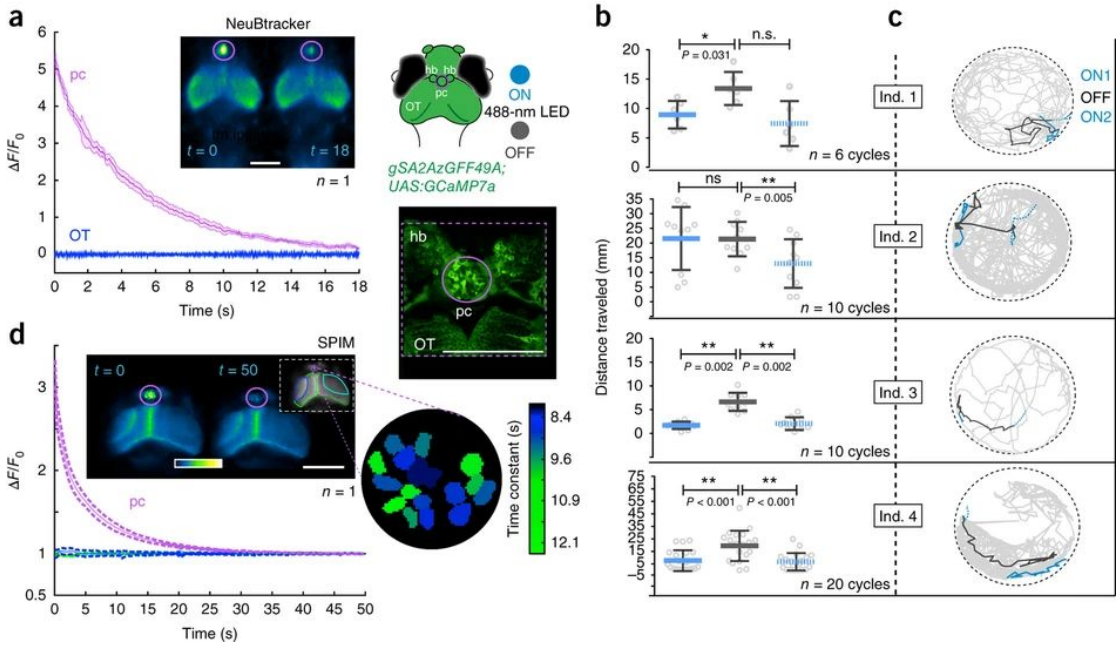

Figure 6.5: *(a)* Fluorescence signal changes obtained with NeuBtracker from the PC and optic tectum (OT) in a larva expressing the calcium indicator GCaMP7a. The signal was averaged over ten dark-light cycles. Right, schematic drawing and two-photon microscopy image of the anterior larval zebrafish brain showing pc, habenulae (hb) and OT. The symbols indicate the color coding of the stimulation paradigm consisting of alternating periods of illumination with the LED ON (blue) or OFF (gray). *(b)* Plot of the median and the interquartile range of the locomotor activity (distance traveled) across different cycles (50 s light ON, 10 sec OFF and 50 sec ON again) for four individuals. *(c)* Plot of swimming trajectories color coded for the illumination condition for four animals. *(d)* Fluorescent signal time courses in PC (purple ROI) detected by SPIM in the same transgenic larvae immobilized in 1% low melting agarose.

To analyze stimulus-induced neurobehavioral responses, we applied the odorant cadaverine [148] into one of two reservoirs of a custom-built arena such that it could diffuse on one side of a central divider. We simultaneously tracked the swimming trajectory and the neuronal activity of larvae exhibiting prominent expression of GCaMP7a in the optic tectum and anterior brain regions [139] and observed repeated activations of the fish's olfactory epithelium after multiple visits to the cadaverine port. The experiemnts are described in Fig. 6.6.

6.5 Conclusion

It is a long-standing objective in neuroscience to measure distributed neuronal activity in freely behaving animals. In this light, "NeuBtracker" implements a tracking microscope for simulta-

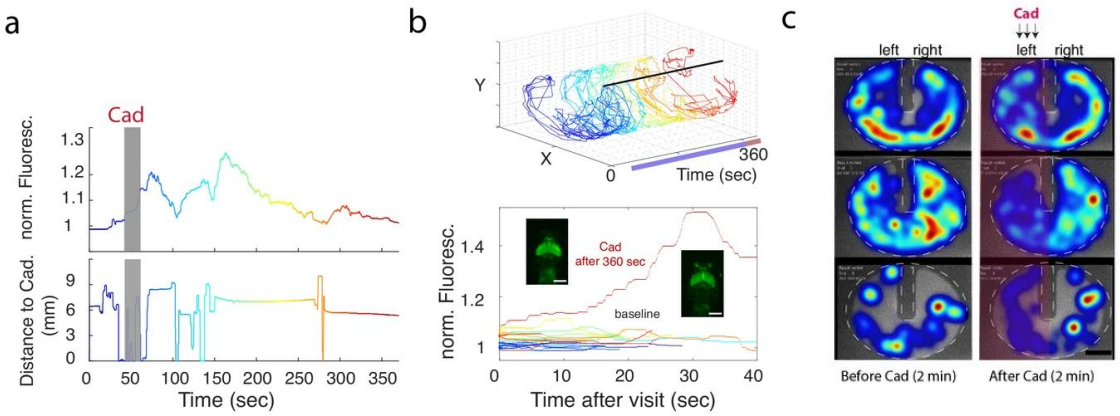

Figure 6.6: *(a)* Fluorescent signal changes recorded in the olfactory epithelium in the experiment shown in Fig. 6.1 plotted here continuously over the entire duration of the experiment together with the distance of the fish to the cadaverine port at each point in time. *(b)* Control experiment in which water was injected instead of cadaverine. After the end of the 360 second baseline observation period, cadaverine was injected.*(c)* Representative heat maps of the behavioral traces for 3 different individuals during 2 minutes before (left) and after (right) delivery of cadaverine to the left compartment.

neous imaging of neuronal activity and behavior of freely swimming fluorescent reporter fish. The system enables the possibility of screening neurostimulants with respect to their neuronal and behavioral effects, while determining spontaneous and stimulus-induced spatio-temporal neuronal activation patterns during unrestrained behavior.

Part VI

Final Thoughts

Chapter 7

Conclusion

The sampling patterns of the conventional light field microscope are highly depth-dependent, which implies non-uniform recoverable lateral resolution across depth. Moreover, reconstructions using state-of-the-art approaches suffer from strong artifacts at axial ranges, where the LFM samples the light field at a coarse rate. In this thesis we study the sampling patterns of the LFM and analyze how they introduce aliasing, in order to understand the cause of the artifacts. We introduce a flexible light field point spread function model to cope with arbitrary LFM designs (with varying MLA to sensor distance) and propose a novel aliasing-aware deconvolution for artifact-free 3D reconstruction. We evaluate the depth-dependent trade-offs in terms of recoverable lateral resolution when comparing various LFM configurations.

Fourier light field microscopy, also referred to as Fourier integral microscopy (FiMic) in the literature, was recently proposed as an alternative to conventional LFM. FiMic is designed to overcome the non-uniform lateral resolution limitation specific to LFM. In this thesis, we analyze the image formation process in FLFM to understand how the modified microscope samples the light field, and, based on this analysis, we discuss the conditions and extent to which the computational super-resolution is possible in FLFM. We propose a deconvolution scheme combining the well-known Expectation-Maximization algorithm with total variation regularization.

The proposed reconstruction algorithms are evaluated on real experimental data and demonstrate superior image quality results over the state-of-the-art methods.

The methods we developed in this thesis are related to computational super-resolution techniques used in computer vision and computational photography, where sub-pixel shifts (or sub-lenslet shifts in conventional LFM) between multiple aliased views of the same scene are combined to recover an image with higher resolution. Thus, computational super-resolution should not be confused with optical super-resolution which aims at breaking the diffraction limit of imaging systems, as discussed in Chapter 1.

Appendix A

List of publications

- P. Symvoulidis, A. Lauri, **A. Stefanoiu**, M. Cappetta, S. Schneider, H. Jia, A. Stelzl, M. Koch, C. Cruz Perez, A. Myklatun, S. Renninger, A. Chmyrov, T. Lasser, W., V. Ntziachristos, and G. G. Westmeyer. "NeuBtracker - Imaging neurobehavioral dynamics in freely behaving fish." *Nature Methods*, 14, pp. 1079-1082, 2017. DOI: 10.1038/nmeth.4459.

- **A. Stefanoiu**, J. Page, P. Symvoulidis, G. G. Westmeyer, and T. Lasser. "Artifact-free deconvolution in light field microscopy." *Optics Express*, 27, pp. 31644-31666, 2019. DOI: 10.1364/OE.27.031644.

- **A. Stefanoiu**, G. Scrofani, G. Saavedra, M. Martínez-Corral, and T. Lasser. "What about computational super-resolution in fluorescence Fourier light field microscopy?" *Optics Express*, 28, p. 16554, 2020. DOI: 10.1364/OE.391189.

- **A. Stefanoiu**, G. Scrofani, G. Saavedra, M. Martínez-Corral, and T. Lasser. "Deconvolution in Fourier integral microscopy." *Proc. SPIE 11396, Computational Imaging V*, p. 18, 2020. DOI: 10.1117/12.2558516.

Bibliography

[1] Michael W. Davidson. “Pioneers in Optics: Zacharias Janssen and Johannes Kepler”. *Microscopy Today* 17, pp. 44–47, 2009. DOI: 10.1017/s1551929509991052. (Cit. on p. 3).

[2] Eric Clark. “Pioneers in Optics: Galileo Galilei”. *Microscopy Today* 26, pp. 48–49, 2018. DOI: 10.1017/s1551929518000470. (Cit. on p. 3).

[3] Robert Hooke. *Micrographia: or some physiological descriptions of minute bodies made by magnifying glasses, with observations and inquiries thereupon*. London : The Royal Society, 1665. Pp. 1–323. DOI: 10.5962/bhl.title.904. (Cit. on p. 3).

[4] Michael W. Davidson. “Pioneers in Optics: Robert Hooke”. *Microscopy Today* 21, pp. 48–50, 2013. DOI: 10.1017/s1551929513000564. (Cit. on p. 3).

[5] Ian Lawson. “Crafting the microworld: how Robert Hooke constructed knowledge about small things”. *Notes and Records: the Royal Society Journal of the History of Science* 70, pp. 23–44, 2016. DOI: 10.1098/RSNR.2015.0057. (Cit. on p. 3).

[6] Adam J.M. Wollman, Richard Nudd, Erik G Hedlund, and Mark C Leake. *From animaculum to single molecules: 300 years of the light microscope*. 2015. DOI: 10.1098/rsob.150019 (cit. on pp. 3–5, 7).

[7] Antony Van Leeuwenhoek and Samuel Hoole. *The Select Works of Antony Van Leeuwenhoek: Containing his microscopical discoveries in many of the works of nature.* Gale ECCO. Vol. 1. 1800. (Cit. on p. 4).

[8] F. Zernike. “Phase contrast, a new method for the microscopic observation of transparent objects”. *Physica* 9, pp. 686–698, 1942. DOI: 10.1016/S0031-8914(42)80035-X. (Cit. on p. 4).

[9] F. Zernike. “How I discovered phase contrast”. *Science* 121, pp. 345–349, 1955. DOI: 10.1126/SCIENCE.121.3141.345. (Cit. on p. 4).

[10] Joseph von Gerlach. *Mikroskopische Studien aus dem Gebiete der menschlichen Morphologie*. 1858. (Cit. on p. 4).

[11] Camillo Golgi. “Sulla struttura della sostanza grigia del cervello.” *Gaz. Med. Intalianna Lomb.* 6, pp. 244–246, 1873. (Cit. on p. 4).

[12] C Gram. “Ueber die isolirte Färbung der Schizomyceten in Schnitt-und Trockenpräparaten (The differential staining of Schizomycetes in tissues sections and in dried preparations)”. *Fortschritte der Medicin* 2, pp. 185–189, 1884. (Cit. on p. 4).

[13] George Gabriel Stokes. “On the change of refrangibility of light”. *Philosophical Transactions of the Royal Society of London* 142, pp. 463–562, 1852. DOI: 10.1098/RSTL.1852.0022. (Cit. on p. 4).

[14] Adolf Baeyer. “Ueber eine neue Klasse von Farbstoffen”. *Berichte der deutschen chemischen Gesellschaft* 4, pp. 555–558, 1871. DOI: 10.1002/cber.18710040209. (Cit. on p. 5).

[15] Osamu Shimomura, Frank H. Johnson, and Yo Saiga. “Extraction, Purification and Properties of Aequorin, a Bioluminescent Protein from the Luminous Hydromedusan, Aequorea”. *Journal of Cellular and Comparative Physiology* 59, pp. 223–239, 1962. DOI: 10.1002/JCP.1030590302. (Cit. on p. 5).

[16] Martin Chalfie, Yuan Tu, Ghia Euskirchen, William W. Ward, and Douglas C. Prasher. “Green fluorescent protein as a marker for gene expression”. *Science* 263, pp. 802–805, 1994. DOI: 10.1126/science.8303295. (Cit. on p. 5).

[17] J. S. Ploem. “The use of a vertical illuminator with interchangeable dichroic mirrors for fluorescence microscopy with incidental light.” *Zeitschrift fur wissenschaftliche Mikroskopie und mikroskopische Technik* 68, pp. 129–142, 1967. (Cit. on p. 5).

[18] J S Ploem and F Walter. “Multi-wavelength epi-illumination in fluorescence microscopy”. *Edition CDR* 5, pp. 1–16, 2001. (Cit. on p. 5).

[19] Marvin Minsky. “Microscopy Apparatus”. *US Patent 3013467* 3013467, p. 5, 1957. (Cit. on p. 5).

[20] Shinya Inoué. “Foundations of confocal scanned imaging in light microscopy”. In: *Handbook of Biological Confocal Microscopy: Third Edition*. Springer, Boston, MA, 2006. Pp. 1–19. DOI: 10.1007/978-0-387-45524-2_1. (Cit. on pp. 5, 6).

[21] A. Canette and R. Briandet. “Microscopy: Confocal Laser Scanning Microscopy”. In: *Encyclopedia of Food Microbiology: Second Edition*. Elsevier Inc., 2014. Pp. 676–683. DOI: 10.1016/B978-0-12-384730-0.00214-7. (Cit. on p. 5).

[22] Maria Göppert-Mayer. “Über Elementarakte mit zwei Quantensprüngen”. *Annalen der Physik* 401, pp. 273–294, 1931. (Cit. on p. 5).

[23] N. Nishimura. “Experimental Methods for Measuring Blood Flow in Brain Capillaries”. *Primer on Cerebrovascular Diseases: Second Edition*, pp. 339–343, 2017. DOI: 10.1016/B978-0-12-803058-5.00071-0. (Cit. on p. 5).

[24] A. H. Voie, D. H. Burns, and F. A. Spelman. “Orthogonal-plane fluorescence optical sectioning: Three-dimensional imaging of macroscopic biological specimens”. *Journal of Microscopy* 170, pp. 229–236, 1993. DOI: 10.1111/J.1365-2818.1993.TB03346.X. (Cit. on p. 5).

[25] Tanner C. Fadero, Therese M. Gerbich, Kishan Rana, Aussie Suzuki, Matthew DiSalvo, Kristina N. Schaefer, Jennifer K. Heppert, Thomas C. Boothby, Bob Goldstein, Mark Peifer, Nancy L. Allbritton, Amy S. Gladfelter, Amy S. Maddox, and Paul S. Maddox. “LITE microscopy: Tilted light-sheet excitation of model organisms offers high resolution and low photobleaching”. *The Journal of Cell Biology* 217, p. 1869, 2018. DOI: 10.1083/JCB.201710087. (Cit. on p. 5).

[26] E. Abbe. “Beiträge zur Theorie des Mikroskops und der mikroskopischen Wahrnehmung”. *Archiv für Mikroskopische Anatomie 1873 9:1* 9, pp. 413–468, 1873. DOI: 10.1007/BF02956173. (Cit. on p. 5).

[27] Jan Keller, Andreas Schönle, and Stefan W. Hell. “Efficient fluorescence inhibition patterns for RESOLFT microscopy”. *Optics Express* 15, p. 3361, 2007. DOI: 10.1364/oe.15.003361. (Cit. on p. 6).

[28] Stefan W. Hell and Jan Wichmann. “Breaking the diffraction resolution limit by stimulated emission: stimulated-emission-depletion fluorescence microscopy”. *Optics Letters* 19, p. 780, 1994. DOI: 10.1364/ol.19.000780. (Cit. on p. 6).

[29] Thomas A. Klar and Stefan W. Hell. “Subdiffraction resolution in far-field fluorescence microscopy”. *Optics Letters* 24, p. 954, 1999. DOI: 10.1364/ol.24.000954. (Cit. on p. 6).

[30] Eric Betzig, George H. Patterson, Rachid Sougrat, O. Wolf Lindwasser, Scott Olenych, Juan S. Bonifacino, Michael W. Davidson, Jennifer Lippincott-Schwartz, and Harald F. Hess. “Imaging intracellular fluorescent proteins at nanometer resolution”. *Science* 313, pp. 1642–1645, 2006. DOI: 10.1126/science.1127344. (Cit. on p. 6).

[31] Ryoko Ando, Hiroshi Hama, Miki Yamamoto-Hino, Hideaki Mizuno, and Atsushi Miyawaki. “An optical marker based on the UV-induced green-to-red photoconversion of a fluorescent protein”. *Proceedings of the National Academy of Sciences of the United States of America* 99, pp. 12651–12656, 2002. DOI: 10.1073/pnas.202320599. (Cit. on p. 6).

[32] Samuel T. Hess, Thanu P.K. Girirajan, and Michael D. Mason. “Ultra-high resolution imaging by fluorescence photoactivation localization microscopy”. *Biophysical Journal* 91, pp. 4258–4272, 2006. DOI: 10.1529/biophysj.106.091116. (Cit. on p. 6).

[33] Michael J. Rust, Mark Bates, and Xiaowei Zhuang. “Sub-diffraction-limit imaging by stochastic optical reconstruction microscopy (STORM)”. *Nature Methods* 3, pp. 793–795, 2006. DOI: 10.1038/nmeth929. (Cit. on p. 6).

[34] Brent Bailey, Daniel L. Farkas, D. Lansing Taylor, and Frederick Lanni. “Enhancement of axial resolution in fluorescence microscopy by standing-wave excitation”. *Nature* 366, pp. 44–48, 1993. DOI: 10.1038/366044a0. (Cit. on p. 6).

[35] M. G.L. Gustafsson. “Surpassing the lateral resolution limit by a factor of two using structured illumination microscopy”. *Journal of Microscopy* 198, pp. 82–87, 2000. DOI: 10.1046/j.1365-2818.2000.00710.x. (Cit. on p. 6).

[36] Manuel F. Juette, Travis J. Gould, Mark D. Lessard, Michael J. Mlodzianoski, Bhupendra S. Nagpure, Brian T. Bennett, Samuel T. Hess, and Joerg Bewersdorf. “Three-dimensional sub-100 nm resolution fluorescence microscopy of thick samples”. *Nature Methods* 5, pp. 527–529, 2008. DOI: 10.1038/nmeth.1211. (Cit. on p. 6).

[37] Gleb Shtengel, James A. Galbraith, Catherine G. Galbraith, Jennifer Lippincott-Schwartz, Jennifer M. Gillette, Suliana Manley, Rachid Sougrat, Clare M. Waterman, Pakorn Kanchanawong, Michael W. Davidson, Richard D. Fetter, and Harald F. Hess. “Interferometric fluorescent super-resolution microscopy resolves 3D cellular ultrastructure”. *Proceedings of the National Academy of Sciences of the United States of America* 106, pp. 3125–3130, 2009. DOI: 10.1073/pnas.0813131106. (Cit. on p. 6).

[38] Peter W. Winter and Hari Shroff. *Faster fluorescence microscopy: Advances in high speed biological imaging*. 2014. DOI: 10.1016/j.cbpa.2014.04.008 (cit. on p. 6).

[39] Bassam Hajj, Mohamed El Beheiry, and Maxime Dahan. “PSF engineering in multifocus microscopy for increased depth volumetric imaging”. *Biomedical Optics Express* 7, p. 726, 2016. DOI: 10.1364/boe.7.000726. (Cit. on p. 7).

[40] Sharon V. King, Ana Doblas, Nurmohammed Patwary, Genaro Saavedra, Manuel Martínez-Corral, and Chrysanthe Preza. “Implementation of PSF engineering in high-resolution 3D microscopy imaging with a LCoS (reflective) SLM”. In: *Three-Dimensional and Multidimensional Microscopy: Image Acquisition and Processing XXI*. Vol. 8949. SPIE, 2014. P. 894913. DOI: 10.1117/12.2040723. (Cit. on p. 7).

[41] Wenxiao Wang, Fan Ye, Hao Shen, Nicholas A. Moringo, Chayan Dutta, Jacob T. Robinson, and Christy F. Landes. “Generalized method to design phase masks for 3D super-resolution microscopy”. *Optics Express* 27, p. 3799, 2019. DOI: 10.1364/oe.27.003799. (Cit. on p. 7).

[42] Majid Badieirostami, Matthew D. Lew, Michael A. Thompson, and W. E. Moerner. “Three-dimensional localization precision of the double-helix point spread function versus astigmatism and biplane”. *Applied Physics Letters* 97, 2010. DOI: 10.1063/1.3499652. (Cit. on p. 7).

[43] Gergely Katona, Gergely Szalay, Pál Maák, Attila Kaszás, Máté Veress, Dániel Hillier, Balázs Chiovini, E Sylvester Vizi, Botond Roska, and Balázs Rózsa. “Fast two-photon in vivo imaging with three-dimensional random-access scanning in large tissue volumes”. *Nature Methods* 9, pp. 201–208, 2012. DOI: 10.1038/nmeth.1851. (Cit. on p. 7).

[44] Robert Prevedel, Young Gyu Yoon, Maximilian Hoffmann, Nikita Pak, Gordon Wetzstein, Saul Kato, Tina Schrödel, Ramesh Raskar, Manuel Zimmer, Edward S Boyden, and Alipasha Vaziri. “Simultaneous whole-animal 3D imaging of neuronal activity using light-field microscopy”. *Nature Methods* 11, pp. 727–730, 2014. DOI: 10.1038/nmeth.2964. arXiv: 1401.5333. (Cit. on pp. 7, 29, 30, 32, 37, 40, 71).

[45] Nils Wagner, Nils Norlin, Jakob Gierten, Gustavo de Medeiros, Bálint Balázs, Joachim Wittbrodt, Lars Hufnagel, and Robert Prevedel. “Instantaneous isotropic volumetric imaging of fast biological processes”. *Nature Methods* 16, pp. 497–500, 2019. DOI: 10.1038/s41592-019-0393-z. (Cit. on pp. 7, 8, 30, 40, 49, 52).

[46] Young-Gyu Yoon, Zeguan Wang, Nikita Pak, Demian Park, Peilun Dai, Jeong Seuk Kang, Ho-Jun Suk, Panagiotis Symvoulidis, Burcu Guner-Ataman, Kai Wang, and Edward S. Boyden. “Sparse decomposition light-field microscopy for high speed imaging of neuronal activity”. *Optica* 7, p. 1457, 2020. DOI: 10.1364/optica.392805. (Cit. on p. 7).

[47] Josue Page Vizcaino, Federico Saltarin, Yury Belyaev, Ruth Lyck, Tobias Lasser, and Paolo Favaro. “Learning to Reconstruct Confocal Microscopy Stacks from Single Light Field Images”. *IEEE Transactions on Computational Imaging* 7, pp. 775–788, 2021. DOI: 10.1109/TCI.2021.3097611. arXiv: 2003.11004. (Cit. on p. 7).

[48] Josue Page, Federico Saltarin, Yury Belyaev, Ruth Lyck, and Paolo Favaro. “Learning to Reconstruct Confocal Microscopy Stacks from Single Light Field Images”. 2020. arXiv: 2003.11004. (Cit. on p. 7).

[49] Lin Cong, Zeguan Wang, Yuming Chai, Wei Hang, Chunfeng Shang, Wenbin Yang, Lu Bai, Jiulin Du, Kai Wang, and Quan Wen. “Rapid whole brain imaging of neural activity in freely behaving larval zebrafish (Danio rerio)”. *eLife* 6, 2017. DOI: 10.7554/eLife.28158. (Cit. on pp. 7, 61).

[50] Haoyu Li, Changliang Guo, Deborah Kim-Holzapfel, Weiyi Li, Yelena Altshuller, Bryce Schroeder, Wenhao Liu, Yizhi Meng, Jarrod B French, Ken-Ichi Takamaru, Michael A Frohman, and Shu Jia. “Fast, volumetric live-cell imaging using high-resolution light-field microscopy”. *Biomedical Optics Express* 10, pp. 29–49, 2019. DOI: 10.1364/BOE.10.000029. (Cit. on pp. 7, 37).

[51] Edward H Adelson and John Y A Wang. *Single Lens Stereo with a Plenoptic Camera*. Tech. rep. 2. 1992, pp. 99 –106. DOI: 10.1109/34.121783 (cit. on p. 7).

[52] G. Lippmann. "Épreuves Réversibles Donnant La Sensation Du Relief". *Journal de Physique Théorique et Appliquée* 7, pp. 821–825, 1908. DOI: 10.1051/jphystap:019080070082100. (Cit. on p. 7).

[53] Ren Ng, Marc Levoy, Mathieu Brédif, Gene Duval, Mark Horowitz, and Pat Hanrahan. *Light Field Photography with a Hand-Held Plenoptic Camera – Stanford Tech Report CTSR 2005-02*. Tech. rep. 2005, pp. 1–11. DOI: 10.1.1.163.488. arXiv: 0070242542 (cit. on pp. 7, 29, 30).

[54] Andrew Lumsdaine and Todor Georgiev. "The focused plenoptic camera". In: *2009 IEEE International Conference on Computational Photography, ICCP 09*. IEEE, 2009. Pp. 1–8. DOI: 10.1109/ICCPHOT.2009.5559008. (Cit. on pp. 7, 29, 35, 52).

[55] Todor Georgiev and Andrew Lumsdaine. "The multifocus plenoptic camera". *Proceedings of SPIE* 8299, pp. 829908–829911, 2012. DOI: doi:10.1117/12.908667. (Cit. on pp. 7, 49, 52).

[56] Christian Perwass and Lennart Wietzke. "Single lens 3D-camera with extended depth-of-field". In: 2012. P. 829108. DOI: 10.1117/12.909882. (Cit. on pp. 7, 42, 52).

[57] Tom E Bishop and Paolo Favaro. "The light field camera: Extended depth of field, aliasing, and superresolution". *IEEE Transactions on Pattern Analysis and Machine Intelligence* 34, pp. 972–986, 2012. DOI: 10.1109/TPAMI.2011.168. (Cit. on pp. 7, 8, 30–32, 40, 52, 57).

[58] Marc Levoy, Ren Ng, Andrew Adams, Matthew Footer, and Mark Horowitz. "Light field microscopy". *ACM Transactions on Graphics* 25, pp. 924–934, 2006. DOI: 10.1145/1141911.1141976. arXiv: 1508.03590. (Cit. on pp. 7, 29, 34, 35, 39, 40, 42, 52).

[59] A Llavador, J Sola-Pikabea, G Saavedra, B Javidi, and M Martínez-Corral. "Resolution improvements in integral microscopy with Fourier plane recording". *Optics Express* 24, pp. 20792–20798, 2016. DOI: 10.1364/oe.24.020792. (Cit. on pp. 7, 53, 63).

[60] A Llavador, J Garcia-Sucerquia, E. Sanchez-Ortiga, G Saavedra, and M. Martinez-Corral. "View images with unprecedented resolution in integral microscopy". *OSA Continuum* 1, pp. 40–47, 2018. DOI: 10.1364/osac.1.000040. (Cit. on pp. 7, 64).

[61] Manuel Martinez-Corral and Bahram Javidi. "Fundamentals of 3D imaging and displays: a tutorial on integral imaging, light-field, and plenoptic systems". *Advances in Optics and Photonics* 10, pp. 512–566, 2018. DOI: 10.1364/aop.10.000512. (Cit. on p. 7).

[62] Ren Ng. "Fourier slice photography". In: *ACM SIGGRAPH 2005 Papers on - SIGGRAPH '05*. 2005. Pp. 735–744. DOI: 10.1145/1186822.1073256. (Cit. on pp. 7, 32, 52).

[63] Donald G Dansereau, Oscar Pizarro, and Stefan B Williams. "Linear Volumetric Focus for Light Field Cameras". *ACM Transactions on Graphics* 34, pp. 1–20, 2015. DOI: 10.1145/2665074. (Cit. on p. 7).

[64] Tom E Bishop, Sara Zanetti, and Paolo Favaro. "Light field superresolution". In: *2009 IEEE International Conference on Computational Photography (ICCP)*. 2009. Pp. 1–9. DOI: 10.1109/ICCPHOT.2009.5559010. (Cit. on pp. 7, 8).

[65] Michael W Tao, Sunil Hadap, Jitendra Malik, and Ravi Ramamoorthi. “Depth from combining defocus and correspondence using light-field cameras”. In: *Proceedings of the IEEE International Conference on Computer Vision*. 2013. Pp. 673–680. DOI: 10.1109/ICCV.2013.89. (Cit. on p. 7).

[66] Michael W. Tao, Jong Chyi Su, Ting Chun Wang, Jitendra Malik, and Ravi Ramamoorthi. “Depth Estimation and Specular Removal for Glossy Surfaces Using Point and Line Consistency with Light-Field Cameras”. *IEEE Transactions on Pattern Analysis and Machine Intelligence* 38, pp. 1155–1169, 2016. DOI: 10.1109/TPAMI.2015.2477811. (Cit. on p. 7).

[67] Michael Broxton, Logan Grosenick, Samuel Yang, Noy Cohen, Aaron Andalman, Karl Deisseroth, and Marc Levoy. “Wave optics theory and 3-D deconvolution for the light field microscope”. *Optics Express* 21, pp. 25418–25439, 2013. DOI: 10.1364/OE.21.025418. (Cit. on pp. 7, 8, 29, 32–35, 37–40, 43, 45–47, 51, 52, 57, 60, 66).

[68] Anca Stefanoiu, Josue Page, Panagiotis Symvoulidis, Gil G Westmeyer, and Tobias Lasser. “Artifact-free deconvolution in light field microscopy”. *Optics Express* 27, pp. 31644–31666, 2019. DOI: 10.1364/OE.27.031644. (Cit. on pp. 7, 8, 57, 60, 61, 79, 80, 100).

[69] Zhi Lu, Jiamin Wu, Hui Qiao, You Zhou, Tao Yan, Zijing Zhou, Xu Zhang, Jingtao Fan, and Qionghai Dai. “Phase-space deconvolution for light field microscopy”. *Optics Express* 27, p. 18131, 2019. DOI: 10.1364/oe.27.018131. (Cit. on p. 7).

[70] M Levoy, Z Zhang, and I McDowall. “Recording and controlling the 4D light field in a microscope using microlens arrays”. *Journal of Microscopy* 235, pp. 144–162, 2009. DOI: 10.1111/j.1365-2818.2009.03195.x. (Cit. on p. 7).

[71] G Scrofani, J Sola-Pikabea, A Llavador, E Sanchez-Ortiga, J C Barreiro, G Saavedra, J Garcia-Sucerquia, and M Martinez-Corral. “FIMic: design for ultimate 3D-integral microscopy of in-vivo biological samples”. *Biomedical Optics Express* 9, pp. 335–346, 2018. DOI: 10.1364/BOE.9.000335. (Cit. on pp. 7, 53, 56, 63, 64).

[72] Noy Cohen, Samuel Yang, Aaron Andalman, Michael Broxton, Logan Grosenick, Karl Deisseroth, Mark Horowitz, and Marc Levoy. “Enhancing the performance of the light field microscope using wavefront coding”. *Optics Express* 22, pp. 24817–24839, 2014. DOI: 10.1364/OE.22.024817. (Cit. on pp. 8, 52).

[73] Chien-Hung Lu, Stefan Muenzel, and Jason Fleischer. “High-Resolution Light-Field Microscopy”. In: *Imaging and Applied Optics*. 2013. CTh3B.2. DOI: 10.1364/COSI.2013.CTh3B.2. (Cit. on pp. 8, 52).

[74] Sina Farsiu, Dirk Robinson, Michael Elad, and Peyman Milanfar. *Advances and challenges in super-resolution*. 2004. DOI: 10.1002/ima.20007 (cit. on pp. 8, 57).

[75] Sung Cheol Park, Min Kyu Park, and Moon Gi Kang. “Super-resolution image reconstruction: a technical overview”. *IEEE Signal Processing Magazine* 20, pp. 21–36, 2003. DOI: 10.1109/msp.2003.1203207. arXiv: 1504.06654. (Cit. on p. 8).

[76] Mattia Rossi and Pascal Frossard. “Geometry-Consistent Light Field Super-Resolution via Graph-Based Regularization”. *IEEE Trans. Image Processing* 27, pp. 4207–4218, 2018. DOI: 10.1109/TIP.2018.2828983. arXiv: 1701.02141. (Cit. on p. 8).

[77] Sven Wanner and Bastian Goldluecke. “Variational light field analysis for disparity estimation and super-resolution”. *IEEE Transactions on Pattern Analysis and Machine Intelligence* 36, pp. 606–619, 2014. DOI: 10.1109/TPAMI.2013.147. (Cit. on pp. 8, 57).

[78] Chia-Kai Liang and Ravi Ramamoorthi. “A Light Transport Framework for Lenslet Light Field Cameras”. *ACM Trans. Graph.* 34, 2015. DOI: 10.1145/2665075. arXiv: 1608.01250. (Cit. on pp. 8, 57).

[79] Sapna A Shroff and Kathrin Berkner. “Image formation analysis and high resolution image reconstruction for plenoptic imaging systems”. *Applied Optics* 52, pp. D22–D31, 2013. DOI: 10.1364/AO.52.000D22. (Cit. on pp. 8, 57).

[80] Arnold Sommerfeld. *Optics (Lectures on theoretical physics, Volume IV)*. Academic Press, 1954. P. 383. (Cit. on p. 11).

[81] Min Gu. *Advanced Optical Imaging Theory*. Vol. 75. Springer, Berlin, Heidelberg, 1999. DOI: 10.1007/978-3-540-48471-4. (Cit. on pp. 11, 12, 14, 16–18, 34, 37, 40, 59–61).

[82] Joseph W Goodman. *Introduction to Fourier Optics in Electrical and Computer Engineering*. Vol. 8. 5. McGraw-Hill Series, 1996. P. 491. arXiv: 0070242542. (Cit. on p. 11).

[83] Christiaan Huygens. *Traité de la lumière, où sont expliquées les causes de ce qui luy arrive dans la réflexion, et dans la réfraction, et particulièrement dans l'étrange réfraction du cristal d'Islande: Avec un discours de la cause de la pesanteur*. Pierre van der Aa, 1690. P. 180. DOI: 10.5479/sil.294285.39088000545160. (Cit. on p. 12).

[84] A Fresnel. *Mémoire sur la Diffraction de la Lumière*. De l'Imprimerie de Feugueray, rue du Cloitre Saint-Benoit, no. 4, 1818. (Cit. on p. 12).

[85] J Hadamard. *Sur les problems aux derivees patielles et leur signification physique*. Vol. 13. 1902. Pp. 49–52. (Cit. on p. 21).

[86] Heinz W. Engl, Martin. Hanke, and Andreas. Neubauer. *Regularization of Inverse Problems*. Kluwer Academic Publishers, 1996. P. 321. DOI: 10.1007/978-94-009-1740-8. (Cit. on p. 21).

[87] Barbara Kaltenbacher, Andreas Neubauer, and Otmar Scherzer. *Iterative Regularization Methods for Nonlinear Ill-Posed Problems*. De Gruyter, 2008. DOI: 10.1515/9783110208276. (Cit. on p. 21).

[88] Otmar Scherzer, Markus Grasmair, Harald Grossauer, Markus Haltmeier, and Frank Lenzen. “Variational regularization methods for the solution of inverse problems”. In: *Applied Mathematical Sciences (Switzerland)*. Vol. 167. Springer, New York, NY, 2009. Pp. 53–113. DOI: 10.1007/978-0-387-69277-7_3. (Cit. on p. 21).

[89] A. N. Tikhonov. “Solution of incorrectly formulated problems and the regularization method.” *Soviet Math. Dokl.* 4, pp. 1035–1038, 1963. (Cit. on p. 22).

[90] Leonid I Rudin, Stanley Osher, and Emad Fatemi. “Nonlinear total variation based noise removal algorithms”. *Physica D: Nonlinear Phenomena* 60, pp. 259–268, 1992. DOI: 10.1016/0167-2789(92)90242-F. (Cit. on pp. 22, 62).

[91] Amir Beck and Marc Teboulle. “Fast gradient-based algorithms for constrained total variation image denoising and deblurring problems”. *IEEE Transactions on Image Processing* 18, pp. 2419–2434, 2009. DOI: 10.1109/TIP.2009.2028250. (Cit. on p. 22).

[92] David Spiegelhalter and Kenneth Rice. “Bayesian statistics”. *Scholarpedia* 4, p. 5230, 2009. DOI: 10.4249/scholarpedia.5230. (Cit. on p. 23).

[93] Tan Bui-Thanh. *A Gentle Tutorial on Statistical Inversion using the Bayesian Paradigm*. Tech. rep. 2012, p. 49 (cit. on p. 23).

[94] Peter M. Lee. “Bayesian Statistics: An Introduction, 4th Edition”. *Journal of Chemical Information and Modeling*, p. 486, 2012. (Cit. on p. 23).

[95] D. Calvetti and E. Somersalo. “Inverse problems: From regularization to Bayesian inference”. *Wiley Interdisciplinary Reviews: Computational Statistics* 10, 2018. DOI: 10.1002/WICS.1427. (Cit. on p. 23).

[96] Simon Arridge, Peter Maass, Ozan Öktem, and Carola-Bibiane Schönlieb. “Solving inverse problems using data-driven models”. *Acta Numerica* 28, pp. 1–174, 2019. DOI: 10.1017/S0962492919000059. (Cit. on pp. 23, 24).

[97] A P Dempster, N M Laird, and D B Rubin. “Maximum Likelihood from Incomplete Data Via the EM Algorithm”. *Journal of the Royal Statistical Society: Series B (Methodological)* 39, pp. 1–22, 1977. DOI: 10.1111/j.2517-6161.1977.tb01600.x. (Cit. on p. 25).

[98] Ashok Veeraraghavan, Ramesh Raskar, Amit Agrawal, Ankit Mohan, and Jack Tumblin. *Dappled Photography: Mask Enhanced Cameras for Heterodyned Light Fields and Coded Aperture Refocusing*. New York, New York, USA, 2007. DOI: 10.1145/1275808.1276463 (cit. on p. 8).

[99] Peng Fei, Zhaoqiang Wang, Hao Zhang, Yicong Yang, Yi Li, and Shangbang Gao. “Deep learning light field microscopy for rapid four-dimensional imaging of behaving animals”. *bioRxiv*, p. 432807, 2018. DOI: 10.1101/432807. (Cit. on pp. 30, 40).

[100] Marc Levoy and Pat Hanrahan. “Light Field Rendering”. In: *Proc. ACM Siggraph*. 1996. Pp. 31–42. (Cit. on p. 30).

[101] Jin-Xiang Chai, Shing-Chow Chan, Heung-Yeung Shum, and Xin Tong. “Plenoptic sampling”. In: *Proc. ACM Siggraph*. 2000. Pp. 307–318. DOI: 10.1145/344779.344932. (Cit. on p. 30).

[102] J Stewart, J Yu, Sj Gortler, and L McMillan. “A new reconstruction filter for undersampled light fields”. *Proceedings of the 14th Eurographics Workshop Rendering*, pp. 150–156, 2003. (Cit. on p. 30).

[103] Zhaolin Xiao, Qing Wang, Guoqing Zhou, and Jingyi Yu. “Aliasing detection and reduction in plenoptic imaging”. In: *Proceedings of the IEEE Computer Society Conference on Computer Vision and Pattern Recognition*. 2014. Pp. 3326–3333. DOI: 10.1109/CVPR.2014.425. (Cit. on p. 30).

[104] Todor Georgiev and Andrew Lumsdaine. “Depth of Field in Plenoptic Cameras”. *Eurographics 2009*, pp. 5–8, 2009. DOI: 10.2312/egs.20091035. (Cit. on p. 30).

[105] Li-Yi Wei, Chia-Kai Liang, Graham Myhre, Colvin Pitts, and Kurt Akeley. “Improving light field camera sample design with irregularity and aberration”. *ACM Transactions on Graphics* 34, 152:1–152:11, 2015. DOI: 10.1145/2766885. (Cit. on pp. 30, 52).

[106] George Wolberg. “Sampling, Reconstruction, and Antialiasing”. In: *Digital Image Warping*. CRC Press, 2004. Pp. 1–32. DOI: 10.1002/jsfa.6623. (Cit. on pp. 31, 34, 59).

[107] David G Voelz and Michael C Roggemann. *Digital simulation of scalar optical diffraction: revisiting chirp function sampling criteria and consequences.* Tech. rep. 32. 2009, pp. 6132–42. DOI: 10.1364/AO.48.006132 (cit. on p. 38).

[108] David G. Voelz. *Computational Fourier Optics: A MATLAB® Tutorial*. SPIE, 2011. P. 250. DOI: 10.1117/3.858456. arXiv: arXiv:1011.1669v3. (Cit. on pp. 38, 56, 60).

[109] William Hadley Richardson. “Bayesian-Based Iterative Method of Image Restoration”. *Journal of the Optical Society of America* 62, pp. 55–59, 1972. DOI: 10.1364/JOSA.62.000055. arXiv: 9807278 [hep-ph]. (Cit. on pp. 41, 61).

[110] B W Silverman, M C Jones, J D Wilson, and D W Nychka. “A Smoothed Em Approach to Indirect Estimation Problems, with Particular Reference to Stereology and Emission Tomography”. *Journal of the Royal Statistical Society: Series B (Methodological)* 52, pp. 271–303, 1990. DOI: 10.1111/j.2517-6161.1990.tb01788.x. (Cit. on p. 42).

[111] Todor Georgiev, Ke Colin Zheng, Brian Curless, David Salesin, Shree Nayar, and Chintan Intwala. “Spatio-angular resolution tradeoffs in integral photography”. *Eurographics Symposium on Rendering (EGSR)*, pp. 263–272, 2006. DOI: 10.2312/EGWR/EGSR06/263-272. (Cit. on p. 42).

[112] Anat Levin, Samuel W Hasinoff, Paul Green, Frédo Durand, and William T Freeman. “4D frequency analysis of computational cameras for depth of field extension”. In: *ACM SIGGRAPH 2009 papers on - SIGGRAPH '09*. 2009. P. 1. DOI: 10.1145/1576246.1531403. (Cit. on pp. 49, 52).

[113] Paolo Favaro. “A split-sensor light field camera for extended depth of field and superresolution”. In: ed. by Peter Schelkens, Touradj Ebrahimi, Gabriel Cristóbal, Frédéric Truchetet, and Pasi Saarikko. 2012. P. 843602. DOI: 10.1117/12.924927. (Cit. on pp. 49, 52).

[114] Moon Gi Kang and Subhasis Chaudhuri. *Super-resolution image reconstruction*. 2003. DOI: 10.1109/MSP.2003.1203206 (cit. on p. 57).

[115] S. Susan Young and Ronald G. Driggers. “Superresolution image reconstruction from a sequence of aliased imagery”. *Applied Optics* 45, pp. 5073–5085, 2006. DOI: 10.1364/AO.45.005073. (Cit. on p. 57).

[116] Jing Tian and Kai Kuang Ma. *A survey on super-resolution imaging*. 2011. DOI: 10.1007/s11760-010-0204-6 (cit. on p. 57).

[117] Jonathan Simpkins and Robert Stevenson. “An Introduction to Super-Resolution Imaging”. In: *Mathematical Optics*. CRC Press, 2012. Pp. 555–580. DOI: 10.1201/b14298-23. (Cit. on p. 57).

[118] Wai San Chan, Edmund Y. Lam, Michael K Ng, and Giuseppe Y Mak. “Super-resolution reconstruction in a computational compound-eye imaging system”. In: *Multidimensional Systems and Signal Processing*. Vol. 18. 2-3. 2007. Pp. 83–101. DOI: 10.1007/s11045-007-0022-3. (Cit. on p. 57).

[119] Ken D. Sauer and Jan P. Allebach. “Iterative Reconstruction of Band Limited Images from Nonuniformly Spaced Samples”. *IEEE Transactions on Circuits and Systems* 34, pp. 1497–1506, 1987. DOI: 10.1109/TCS.1987.1086088. (Cit. on p. 59).

[120] Karlheinz Grochenig. “Reconstruction Algorithms in Irregular Sampling”. *Mathematics of Computation* 59, pp. 181–194, 1992. DOI: 10.2307/2152989. (Cit. on p. 59).

[121] K. Gröchenig and T. Strohmer. “Numerical and Theoretical Aspects of Nonuniform Sampling of Band-Limited Images”. In: *Marvasti F. (eds) Nonuniform Sampling. Information Technology: Transmission, Processing, and Storage*. Springer, Boston, MA, 2001. Pp. 283–324. DOI: 10.1007/978-1-4615-1229-5_6. (Cit. on p. 59).

[122] Simon Baker and Takeo Kanade. “Limits on super-resolution and how to break them”. *IEEE Transactions on Pattern Analysis and Machine Intelligence* 24, pp. 1167–1183, 2002. DOI: 10.1109/TPAMI.2002.1033210. (Cit. on p. 59).

[123] Manuel Martínez-Corral and Genaro Saavedra. “The Resolution Challenge in 3D Optical Microscopy”. *Progress in Optics* 53, pp. 1–67, 2009. DOI: 10.1016/S0079-6638(08)00201-1. (Cit. on p. 59).

[124] Changliang Guo, Wenhao Liu, Xuanwen Hua, Haoyu Li, and Shu Jia. "Fourier light-field microscopy". *Optics Express* 27, pp. 25573–25594, 2019. DOI: 10.1364/oe.27.025573. (Cit. on pp. 60, 63).

[125] L. B. Lucy. "An iterative technique for the rectification of observed distributions". *The Astronomical Journal* 79, p. 745, 1974. DOI: 10.1086/111605. (Cit. on p. 61).

[126] Peter J Green. "On Use of the Em Algorithm for Penalized Likelihood Estimation". *Journal of the Royal Statistical Society: Series B (Methodological)* 52, pp. 443–452, 1990. DOI: 10.1111/j.2517-6161.1990.tb01798.x. (Cit. on p. 62).

[127] Pascal Getreuer. "Rudin-Osher-Fatemi Total Variation Denoising using Split Bregman". *Image Processing On Line* 2, pp. 74–95, 2012. DOI: 10.5201/ipol.2012.g-tvd. (Cit. on p. 62).

[128] Antonin Chambolle. "An Algorithm for Total Variation Minimization and Applications". In: *Journal of Mathematical Imaging and Vision*. Vol. 20. 1-2. 2004. Pp. 89–97. DOI: 10.1023/B:JMIV.0000011321.19549.88. (Cit. on p. 62).

[129] Anca Stefanoiu, Gabriele Scrofani, Genaro Saavedra, Manuel Martínez-Corral, and Tobias Lasser. "Deconvolution in Fourier integral microscopy". In: *Computational Imaging V*. Vol. 11396. SPIE, 2020. P. 18. DOI: 10.1117/12.2558516. (Cit. on pp. 62, 83).

[130] Seung-Hyun Hong, Ju-Seog Jang, and Bahram Javidi. "Three-dimensional volumetric object reconstruction using computational integral imaging". *Optics Express* 12, pp. 483–491, 2004. DOI: 10.1364/opex.12.000483. (Cit. on pp. 63, 64).

[131] Joseph Rosen, Nisan Siegel, and Gary Brooker. "Theoretical and experimental demonstration of resolution beyond the Rayleigh limit by FINCH fluorescence microscopic imaging". *Optics Express* 19, p. 26249, 2011. DOI: 10.1364/oe.19.026249. (Cit. on p. 66).

[132] Donald G Dansereau, Oscar Pizarro, and Stefan B Williams. "Decoding, Calibration and Rectification for Lenselet-Based Plenoptic Cameras". In: *2013 IEEE Conference on Computer Vision and Pattern Recognition*. IEEE, 2013. Pp. 1027–1034. DOI: 10.1109/CVPR.2013.137. (Cit. on p. 71).

[133] Anca Stefanoiu, Gabriele Scrofani, Genaro Saavedra, Manuel Martínez-Corral, and Tobias Lasser. "What about computational super-resolution in fluorescence Fourier light field microscopy?" *Optics Express* 28, p. 16554, 2020. DOI: 10.1364/OE.391189. (Cit. on pp. 83, 102).

[134] Christina K. Kim, Samuel J. Yang, Nandini Pichamoorthy, Noah P. Young, Isaac Kauvar, Joshua H. Jennings, Talia N. Lerner, Andre Berndt, Soo Yeun Lee, Charu Ramakrishnan, Thomas J. Davidson, Masatoshi Inoue, Haruhiko Bito, and Karl Deisseroth. "Simultaneous fast measurement of circuit dynamics at multiple sites across the mammalian brain". *Nature Methods* 13, pp. 325–328, 2016. DOI: 10.1038/nmeth.3770. (Cit. on p. 108).

[135] Loren L. Looger and Oliver Griesbeck. *Genetically encoded neural activity indicators*. 2012. DOI: 10.1016/j.conb.2011.10.024 (cit. on p. 108).

[136] Misha B. Ahrens and Florian Engert. *Large-scale imaging in small brains*. 2015. DOI: 10.1016/j.conb.2015.01.007 (cit. on p. 108).

[137] Ruben Portugues, Claudia E. Feierstein, Florian Engert, and Michael B. Orger. "Whole-brain activity maps reveal stereotyped, distributed networks for visuomotor behavior". *Neuron* 81, pp. 1328–1343, 2014. DOI: 10.1016/j.neuron.2014.01.019. (Cit. on p. 108).

[138] Nikita Vladimirov, Yu Mu, Takashi Kawashima, Davis V. Bennett, Chao Tsung Yang, Loren L. Looger, Philipp J. Keller, Jeremy Freeman, and Misha B. Ahrens. *Light-sheet functional imaging in fictively behaving zebrafish*. 2014. DOI: 10.1038/nmeth.3040 (cit. on p. 108).

[139] Akira Muto, Masamichi Ohkura, Gembu Abe, Junichi Nakai, and Koichi Kawakami. "Real-time visualization of neuronal activity during perception". *Current Biology* 23, pp. 307–311, 2013. DOI: 10.1016/j.cub.2012.12.040. (Cit. on pp. 108, 113).

[140] Eva A. Naumann, Adam R. Kampff, David A. Prober, Alexander F. Schier, and Florian Engert. "Monitoring neural activity with bioluminescence during natural behavior". *Nature Neuroscience* 13, pp. 513–520, 2010. DOI: 10.1038/nn.2518. (Cit. on p. 108).

[141] Allan V. Kalueff, Michael Gebhardt, Adam Michael Stewart, Jonathan M. Cachat, Mallorie Brimmer, Jonathan S. Chawla, Cassandra Craddock, Evan J. Kyzar, Andrew Roth, Samuel Landsman, Siddharth Gaikwad, Kyle Robinson, Erik Baatrup, Keith Tierney, Angela Shamchuk, William Norton, Noam Miller, Teresa Nicolson, Oliver Braubach, Charles P. Gilman, Julian Pittman, Denis B. Rosemberg, Robert Gerlai, David Echevarria, Elisabeth Lamb, Stephan C.F. Neuhauss, Wei Weng, Laure Bally-Cuif, and Henning Schneider. *Towards a comprehensive catalog of zebrafish behavior 1.0 and beyond*. 2013. DOI: 10.1089/zeb.2012.0861 (cit. on p. 108).

[142] Michael B. Orger and Gonzalo G. De Polavieja. "Zebrafish Behavior: Opportunities and Challenges". *Annual Review of Neuroscience* 40, pp. 125–147, 2017. DOI: 10.1146/annurev-neuro-071714-033857. (Cit. on p. 108).

[143] Giancarlo Bruni, Andrew J. Rennekamp, Andrea Velenich, Matthew McCarroll, Leo Gendelev, Ethan Fertsch, Jack Taylor, Parth Lakhani, Dennis Lensen, Tama Evron, Paul J. Lorello, Xi Ping Huang, Sabine Kolczewski, Galen Carey, Barbara J. Caldarone, Eric Prinssen, Bryan L. Roth, Michael J. Keiser, Randall T. Peterson, and David Kokel. "Zebrafish behavioral profiling identifies multitarget antipsychotic-like compounds". *Nature Chemical Biology* 12, pp. 559–566, 2016. DOI: 10.1038/nchembio.2097. (Cit. on p. 108).

[144] Panagiotis Symvoulidis, Antonella Lauri, Anca Stefanoiu, Michele Cappetta, Steffen Schneider, Hongbo Jia, Anja Stelzl, Maximilian Koch, Carlos Cruz Perez, Ahne Myklatun, Sabine Renninger, Andriy Chmyrov, Tobias Lasser, Wolfgang Wurst, Vasilis Ntziachristos, and Gil G. Westmeyer. "NeuBtracker - Imaging neurobehavioral dynamics in freely behaving fish". *Nature Methods* 14, pp. 1079–1082, 2017. DOI: 10.1038/nmeth.4459. (Cit. on p. 108).

[145] Philipp J. Keller, Annette D. Schmidt, Joachim Wittbrodt, and Ernst H.K. Stelzer. "Reconstruction of zebrafish early embryonic development by scanned light sheet microscopy". *Science* 322, pp. 1065–1069, 2008. DOI: 10.1126/science.1162493. (Cit. on p. 112).

[146] Florian O. Fahrbach, Fabian F. Voigt, Benjamin Schmid, Fritjof Helmchen, and Jan Huisken. "Rapid 3D light-sheet microscopy with a tunable lens". *Optics Express* 21, p. 21010, 2013. DOI: 10.1364/oe.21.021010. (Cit. on p. 112).

[147] Owen Randlett, Caroline L. Wee, Eva A. Naumann, Onyeka Nnaemeka, David Schoppik, James E. Fitzgerald, Ruben Portugues, Alix M.B. Lacoste, Clemens Riegler, Florian Engert, and Alexander F. Schier. "Whole-brain activity mapping onto a zebrafish brain atlas". *Nature Methods* 12, pp. 1039–1046, 2015. DOI: 10.1038/nmeth.3581. (Cit. on p. 113).

[148] Ashiq Hussain, Luis R. Saraiva, David M. Ferrero, Gaurav Ahuja, Venkatesh S. Krishna, Stephen D. Liberles, and Sigrun I. Korsching. “High-affinity olfactory receptor for the death-associated odor cadaverine”. *Proceedings of the National Academy of Sciences of the United States of America* 110, pp. 19579–19584, 2013. DOI: 10.1073/pnas.1318596110. (Cit. on p. 113).